การเพิ่มการตอบสนองต่อการรับรู้แก๊สไฮโดรเจนซัลไฟด์ของฟิล์มบางแคลเซียมคอปเปอร์ไททาเนตโดยการเติมสารประกอบซิลเวอร์

นายอุกฤษ นาฎแก้ว

วิทยานิพนธ์นี้เป็นส่วนหนึ่งของการศึกษาตามหลักสูตรปริญญาวิทยาศาสตรมหาบัณฑิต
สาขาวิชาฟิสิกส์ ภาควิชาฟิสิกส์
คณะวิทยาศาสตร์ จุฬาลงกรณ์มหาวิทยาลัย
ปีการศึกษา 2560

ENHANCING H_2S SENSING RESPONSE OF CALCIUM COPPER TITANATE THIN FILMS BY ADDING Ag COMPOUNDS

Mr. Aukrit Natkaeo

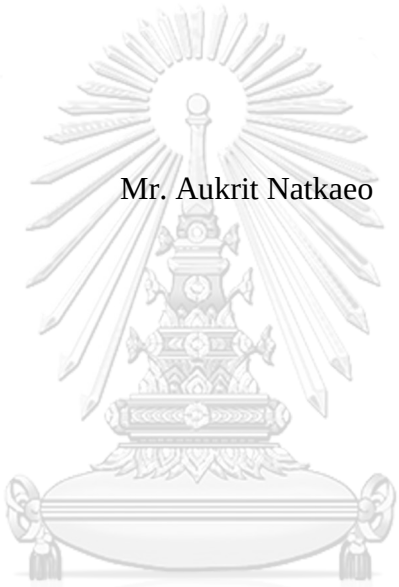

A Thesis Submitted in Partial Fulfillment of the Requirements
for the Degree of Master of Science Program in Physics
Department of Physics
Faculty of Science
Chulalongkorn University
Academic Year 2017

Thesis Title	ENHANCING H_2S SENSING RESPONSE OF CALCIUM COPPER TITANATE THIN FILMS BY ADDING Ag COMPOUNDS
By	Mr. Aukrit Natkaeo
Field of Study	Physics
Thesis Advisor	Associate Professor Satreerat Hodak, Ph.D.
Thesis Co-Advisor	Anurat Wisitsoraat, Ph.D.

Accepted by the Faculty of Science, Chulalongkorn University in Partial Fulfillment of the Requirements for the Master's Degree

.....Dean of the Faculty of Science
(Associate Professor Polkit Sangvanich, Ph.D.)

THESIS COMMITTEE

.....Chairman
(Assistant Professor Rattachat Mongkolnavin, Ph.D.)

.....Thesis Advisor
(Associate Professor Satreerat Hodak, Ph.D.)

.....Thesis Co-Advisor
(Anurat Wisitsoraat, Ph.D.)

.....Examiner
(Assistant Professor Boonchoat Paosawatyanyong, Ph.D.)

.....External Examiner
(Nattasamon Petchsang, Ph.D.)

อุกฤษ นาฏแก้ว : การเพิ่มการตอบสนองต่อการรับรู้แก๊สไฮโดรเจนซัลไฟด์ของฟิล์มบางแคลเซียมคอปเปอร์ไททาเนตโดยการเติมสารประกอบซิลเวอร์ (ENHANCING H_2S SENSING RESPONSE OF CALCIUM COPPER TITANATE THIN FILMS BY ADDING Ag COMPOUNDS) อ.ที่ปรึกษาวิทยานิพนธ์หลัก: รศ. ดร. สตรีรัตน์ โฮดัค, อ.ที่ปรึกษาวิทยานิพนธ์ร่วม: ดร. อนุรัตน์ วิศิษฏ์สรอรรถ, 135 หน้า.

ฟิล์มบางแคลเซียมคอปเปอร์ไททาเนต ($CaCuTi_4O_{12}$: CCTO) ที่เจือเงินที่ความเข้มข้นต่างกันถูกเตรียมด้วยวิธีโซลเจล (sol-gel) ฟิล์มบางความหนาสี่ชั้นถูกปลูกลงบนฐานรองอลูมินาขั้วไฟฟ้าโครเมียมและทองถูกเตรียมด้วยวิธีสปัตเตอร์ริ่งบนผิวชิ้นงานเพื่อสร้างอุปกรณ์รับรู้แก๊ส ฟิล์มบางได้นำมาวิเคราะห์โดยใช้เทคนิคต่างๆ เช่น เทคนิคการเลี้ยวเบนของรังสีเอกซ์ (XRD) สำรวจด้วยกล้องขยายกำลังสูงชนิดส่องผ่านสนามไฟฟ้าจุลทรรศน์อิเล็กตรอนแบบส่องกราด (FESEM) เทคนิคการกระจายพลังงานของรังสีเอกซ์ (EDX) รามานสเปกโตรสโกปี (Raman spectroscopy) และวิธีสเปกโตรสโกปีของอนุภาคอิเล็กตรอนที่ถูกปลดปล่อยด้วยรังสีเอกซ์ (XPS) พบว่าฟิล์มบาง CCTO มีโครงสร้างผลึกเป็นแบบซูโดเพอรอฟสไกต์ที่มีปริมาณไททาเนียมไดออกไซด์เจือปนในโครงสร้างปริมาณน้อย สำหรับงานวิจัยนี้ฟิล์มบาง CCTO ที่ถูกเจือด้วยเงินถูกทดสอบด้วยแก๊สที่หลากหลายเช่น แก๊สไฮโดรเจนซัลไฟด์ (H_2S) แก๊สแอมโมเนีย (NH_3) แก๊สไนโตรเจนไดออกไซด์ (NO_2) และแก๊สเอทานอล เพื่อค้นหาการทำงานสูงสุดต่อการตอบสนองต่อแก๊ส สำหรับผลการศึกษาสมบัติการตอบรับแก๊สไฮโดรเจนซัลไฟด์ในช่วงความเข้มข้น 0.2-10 พีพีเอ็มของฟิล์มบาง CCTO ถูกดำเนินการในช่วงอุณหภูมิระหว่าง 150-350 องศาเซลเซียส เมื่อทำการเปรียบเทียบการทำงานสูงสุดต่อการตอบสนองต่อแก๊สไฮโดรเจนซัลไฟด์พบว่าฟิล์มบาง CCTO ที่เจือด้วยเงินตอบสนองได้ดีกว่าฟิล์มบางที่ไม่ได้เจือเงิน การทำงานสูงสุดต่อการตอบสนองต่อแก๊สไฮโดรเจนซัลไฟด์ถูกศึกษาในฟิล์มบาง CCTO ที่เจือด้วยเงิน 0.9 เปอร์เซ็นต์โดยน้ำหนักที่อุณหภูมิ 250 องศาเซลเซียสซึ่งได้ผลดีกว่าฟิล์มบาง CCTO ที่ไม่เจือด้วยเงินประมาณ 10 เท่า ฟิล์มบางที่เจือด้วยเงินมีเวลาตอบสนองและเวลาคืนสภาพที่น้อยกว่าฟิล์มที่ไม่ถูกเจือด้วยเงิน อีกทั้งยังพบว่าเงินเป็นตัวเร่งปฏิกิริยาออกซิเดชันในฟิล์มอีกด้วย ดังนั้น ฟิล์มบาง CCTO ที่เจือด้วยเงินปริมาณน้อยจึงเป็นตัวเลือกที่เยี่ยมยอดในการนำมาสร้างเป็นอุปกรณ์รับรู้แก๊สไฮโดรเจนซัลไฟด์

ภาควิชา ฟิสิกส์	ลายมือชื่อนิสิต .....
สาขาวิชา ฟิสิกส์	ลายมือชื่อ อ.ที่ปรึกษาหลัก .....
ปีการศึกษา 2560	ลายมือชื่อ อ.ที่ปรึกษาร่วม .....

5772223523 : MAJOR PHYSICS
KEYWORDS: CCTO THIN FILM, HYDROGEN SULFIDE SENSOR, GAS SENSING PROPERTIES, SILVER DOPING

AUKRIT NATKAEO: ENHANCING H_2S SENSING RESPONSE OF CALCIUM COPPER TITANATE THIN FILMS BY ADDING Ag COMPOUNDS. ADVISOR: ASSOC. PROF. SATREERAT HODAK, Ph.D., CO-ADVISOR: ANURAT WISITSORAAT, Ph.D., 135 pp.

Ag-doped $CaCu_3Ti_4O_{12}$ (CCTO) thin films with different doping concentrations were prepared by a sol-gel technique. Films were grown by depositing four layers of CCTO on alumina substrates followed by sputtering Au/Cr interdigitated electrodes to fabricate gas sensors. The films were characterized by X-ray diffraction (XRD), field emission scanning electron microscopy (FESEM), energy dispersive X-ray spectroscopy (EDX) Raman spectroscopy and X-ray photoemission spectroscopy (XPS). The films have predominantly the perovskite CCTO crystal phase with very small amount of TiO_2 secondary phases. In this thesis, both undoped CCTO and Ag-doped CCTO thin films were tested for selective sensing to H_2S gas relative to NH_3, H_2, NO_2 and ethanol vapor. For characterizing gas sensing properties of the films, gas concentrations in the range of 0.2-10 ppm were used with operating temperatures ranging from 150 to 350 °C. When compared to undoped CCTO sensor, the Ag-doped CCTO sensors presented much higher response. The best sensor response towards H_2S was found in 0.9 wt% Ag-doped CCTO film and at the optimum operating temperature of 250 °C. The highest response of the sensor based on the 0.9 wt% Ag-doped CCTO film to 10 ppm of H_2S is approximately 99 which is ten times than that of a sensor based on undoped CCTO film. The doped film sensor also showed stability and relatively short response and recovery times. It is found that Ag plays a role promoting the adsorption as well as the catalytic oxidation of H_2S. Therefore, Ag-doped CCTO films with small doping concentration constitute an excellent candidate for developing H_2S sensors operating at low-temperatures.

Department:	Physics	Student's Signature	.....
Field of Study:	Physics	Advisor's Signature	.....
Academic Year:	2017	Co-Advisor's Signature	.....

ACKNOWLEDGEMENTS

First and foremost, I would like to express my deep gratitude to my great advisor, Associate Professor Dr. Satreerat K. Hodak, for her guidance, patience, understanding, encouragement, and friendly discussion during this work.

Special thank goes to Dr. Anurat Wisitsoraat and Mr. Disayut Phokharatkul for helping in electrode sputtering, dicing the samples and gas-sensing measurement. I greatly appreciate them for giving several useful comments and suggestions to improve my thesis.

I would like to really thank Assistant Professor Dr. Jose Hodak for helping me with gas sensing mechanism and paper improvement for good impact factor publication.

I express my sincere thanks to Assistant Professor Dr. Rattachat Mongkolnavin, Assistant Professor Dr. Boonchoat Paosawatyanyong and Dr. Nattasamon Petchsang for attending as a chairman and committee of this thesis.

I would like to specially thank to Dr. Adisorn Tuantranont and National Electronics and Computer technology (NECTEC) for gas-sensing facilities.

I would also take this opportunity to thanks the Department of Physics, Faculty of science, Chulalongkorn university financial support in doing this thesis as well as paying for expenses to attend the conference.

I would like to thank the Development and Promotion of Science and Technology Talents Project (DPST) and the 90th Anniversary of Chulalongkorn University Fund to support budgets for this work.

Finally, I would like to express my deepest gratitude to my family for their endless support, understanding, encouragement and support throughout my entire study.

CONTENTS

Page

Page

List of Tables

Table Page

List of Figures

Figure Page

CHAPTER I
INTRODUCTION

1.1 Thesis motivation and literature review

Nowadays, air pollution becomes a significant threat to human life due to increasing vehicle and industrial emissions. Various environmentally harmful gases including greenhouse gas and toxic gases such as hydrogen sulfide (H_2S), hydrogen (H_2), methane (NH_3), nitrogen dioxide (NO_2), and ethanol vapor can be occurred in the air. These gases can be effected on human health and the environment. Table 1.1 shows the source of listed air pollutant gases, their the toxicity and the threshold limit values (TLV). TLV is defined as the maximum concentration of a chemical allowable for repeated exposure without producing adverse health effects. In addition, long-term exposure to air pollution can cause cancer and damage to the immune, neurological, reproductive, and respiratory systems. In extreme cases, it can even cause death. Therefore, gas sensors are investigated to supervise air quality in order to ensure the maximum safety for the human life.

Table 1.1: Health effects of air pollutant gases.

Gas	Source of production	Toxicity to human and environment	TLV	Ref
H_2S	Mines, petroleum fields and natural gas production	Headache (2 ppm), eye irritation (10-20 ppm), lung irritation (100 ppm), pulmonary edema (300 ppm), death within 5 min (800 ppm)	10 ppm	[1, 2]
H_2	Natural gas, oil, coal and water	The risk of unconsciousness or death (High concentrations), dangerous gas for transport and storage (explosion ~15,000 ppm)	No data	[3, 4]
NH_3	Agriculture, industry, refrigerant and chemistry	Respiratory irritation, eye irritation and pulmonary edema (more than 1,000 ppm)	35 ppm	[5]
NO_2	The smoke from power plants, manufacturing factories, furnaces and fuel burning devices	Lung and respiratory diseases	3 ppm	[6, 7]
Ethanol vapor	Fermentation of sugars by yeasts or by petrochemical processes.	Irritation	1,000 ppm	[8]

In recent years, gas sensors for the detection of gaseous molecules have attracted much attention. The goal of gas sensor research is to create the detection with a group range of gases or specific type of gases. Detection the quantity of gases is important for security and gas control. It would be expected to be useful for many applications such as food processing, environmental remediation, agriculture, medical diagnostics and defense [9]. The semiconducting metal oxide gas sensors such as ZnO, SnO_2, TiO_2 and WO_3 are found to be a potential candidate because of simple fabrication, their ease of use, low cost and robustness [10]. Their gas sensors can be utilized to detect combustible, reducing, or oxidizing gases. In addition, the gas sensing performance enhanced remarkably when the metal oxide materials were doped with metal catalysts. Table 1.2 summarizes the recent work in the metal oxide materials in different forms such as nanoparticles, nanofibers, nanorods, mesoporous, thin to thick films, and ceramics with the noble dopants for the gas sensing study.

Table 1.2: Literature papers focusing on the sensing properties of metal oxide gas sensors towards target gases.

Target gas	**Materials**	**Methods**	**Operating Temperature (°C)**	**Concentration (ppm)**	**Sensor response (no unit)**	**Ref.**
H_2S	2 wt% Ag doped α-Fe_2O_3 (nanoparitcles)	Chemical Coprecipitation	160	100	~50	[11]
	0.5 mol% Ag-loaded WO_3 (mesoporous)	Using three dimensional cubic KIT-6	75	10	~5	[12]
	4 molar% Ag-doped ɤ-Fe_2O_3/SiO_2 (thin films)	Sol-gel	150	10	~1	[13]
	0.38 wt% Ag-Doped In_2O_3 (nanoparticles)	Standard screen-printing technique	100	10	40,010	[14]
	Ag/TiO_2 (nanofibers)	Electrospinning technique	350	10	240	[15]

Target gas	Materials	Methods	Operating Temperature (°C)	Concentration (ppm)	Sensor response (no unit)	Ref.
H_2S	Ag-Catalyzed SnO_2 (thin films)	Glancing angle deposition	300	5	66.67	[16]
	0.44 wt% Ag doped ZnO (nanowires)	Screen-printing technique	300	100	151	[17]
	0.1 wt% V-doped SnO_2 (nanoparticles)	Flame spray pyrolysis	350	5	550	[18]
	0.5 wt% Mo-doped SnO_2 (nanoparticles)	Flame spray pyrolysis	250	10	75	[19]
	0.50 wt% Ru-WO_3 (nanorods)	Hydrothermal and impregnation	350	5	115	[20]
	0.5 wt% Rh doped SnO_2 (nanoparticles)	Flame spray pyrolysis	300	10	30	[21]
	1 wt% Pd loaded WO_3 (nanoparticles)	Precipitation and impregnation methods	150	10	6	[22]
H_2	Ag-decorated SnO (nanoparticles)	The carbothermal reduction method	300	100	~4	[23]
	Pd-decorated SnO (nanoparticles)	The carbothermal reduction method	300	100	~13	[23]
	CuO-modified tin titanate : $Sn_{0.8}Ti_{0.2}O_2$ (thick film)	Screen printing technique	400	1,000	263.42	[24]
	WO_3 (nanoparticles)	Soft-template method	200	50	1.16	[25]
	Pd-decorated WO_3 (nanoparticles)	Soft-template method	200	50	115.28	[25]
	Ag-decorated WO_3 (nanoparticles)	Soft-template method	200	50	2.31	[25]
	Au-decorated WO_3 (nanoparticles)	Soft-template method	200	50	9.34	[25]
	ZnO (nanofibers)	Electrospinning technique	350	10	109.1	[26]
	SnO_2 (nanofibers)	Electrospinning technique	350	10	5.9	[26]

Target gas	Materials	Methods	Operating Temperature (°C)	Concentration (ppm)	Sensor response (no unit)	Ref.
NH_3	2 wt% Ag doped α-Fe_2O_3 (nanoparitcles)	Chemical Coprecipitation	160	1,000	~2	[11]
	0.5 mol% Ag-loaded WO_3 (mesoporous)	Using three dimensional cubic KIT-6	75	10	~2	[12]
	4 molar% Ag-doped ɤ-Fe_2O_3/SiO_2 (thin films)	Sol-gel	150	10	~6	[13]
	0.38 wt% Nano Ag-Doped In_2O_3 (nanoparticles)	Standard screen-printing technique	100	100	0.3	[14]
	0.44 wt% Ag doped ZnO (nanowires)	Screen-printing technique	300	100	3.6	[17]
	0.5 wt% Mo-doped SnO_2 (nanoparticles)	Flame spray pyrolysis	250	2,000	2	[19]
	0.50 wt% Ru-WO_3 (nanorods)	Hydrothermal and impregnation	350	100	2	[20]
	1 wt% Pd loaded WO_3 (nanoparticles)	Precipitation	150	1,500	5	[22]
NO_2	4 molar% Ag-doped ɤ-Fe_2O_3/SiO_2 (thin films)	Sol-gel	150	10	~1	[13]
	0.1 wt% V-doped SnO_2 (nanoparticles)	Flame spray pyrolysis	350	5	30	[18]
	0.5 wt% Mo-doped SnO_2 (nanoparticles)	Flame spray pyrolysis	250	10	7	[19]
	0.50 wt% Ru-WO_3 (nanorods)	Hydrothermal and impregnation	350	5	2	[20]
	0.5 wt% Rh doped SnO_2 (nanoparticles)	Flame spray pyrolysis	300	5	10	[21]
	1 wt% Pd loaded WO_3 (nanoparticles)	Precipitation and impregnation methods	150	5	2	[22]
	Cu, Zn two-element doped SnO_2 octahedral (nanoparticle)	One-step hydrothermal method	110	50	160	[27]

Target gas	Materials	Methods	Operating Temperature (°C)	Concentration (ppm)	Sensor response (no unit)	Ref.
Ethanol vapor	Cu, Zn two-element doped SnO_2 octahedral (nanoparticles)	One-step hydrothermal method	110	50	210	[27]
	V_2O_5 hierarchical structure networks (nanoparticles)	Direct seed-induced hydrothermal growth	250	100	4	[28]
	ZnO (nanorods)	Simple low-temperature hydrothermal process	320	200	35	[29]
	$Ag@TiO_2$ (nanoparticles)	Chemical reduction and the reverse micelle sol-gel method	25	5	4.35	[30]

H_2S is a colorless and toxic gas which has a very distinct odor even at very low concentrations. H_2S is quite ubiquitous in nature and very important in a variety of areas. Detection and quantification of H_2S is important in occupational safety and health. Because the olfactory response ceases to recognize the presence of H_2S after a short exposure regulations for the maximum permitted air concentration are on the order of 10 ppm for and eight hour exposure [31]. Monitoring the H_2S content is of industrial relevance, spanning the food, oil and construction industries. The food industry relies on detection of unpleasant smells that deteriorate the organoleptic character of food, and it may even be used to monitor its decomposition [32]. In the oil industry, sulfur is a well-known poison for the catalytic production of light hydrocarbon [33]. The degradation of concrete structures is determined by the concentration of H_2S which at levels as low as 2-10 ppm leads to corrosion rates on the 1-5 mm per year in sewers causing nearly half of the sewer maintenance costs [34, 35]. In recent years H_2S in exhaled air is emerging as a useful biomarker in diagnosis and treatments for asthma

and other diseases [36, 37]. In all these applications H_2S gas needs to be detected in sub-10 ppm concentrations, which often contain higher concentrations of other gaseous components. For example sewers contain among other gases CO, CO_2, ammonia and methane [34], while exhales air may contain ammonia or NO [37]. It becomes clear that highly selective detection of H_2S on scales lower than a few ppm is critical for human health, industry and environmental care.

As seen from Table 1.2, various materials, which are synthesized in the different forms are used as active layers in such gas-sensing devices [10]. Based on the discovery in our laboratory not a long ago, calcium copper titanate ($CaCu_3Ti_4O_{12}$: CCTO) contains copper ions in its structure which is capable of interaction with sulfide. Therefore, it may be expected that changes in the band occupancy of CCTO can occur by adsorption of sulfide, leading to the basal electrical response of CCTO to H_2S gas. $CaCu_3Ti_4O_{12}$ (CCTO) has been explored as an alternative candidate to conventional metal oxides for gas-sensing application. CCTO is relatively few investigated as gas-sensing materials [38, 39]. For example, single-phase CCTO thin films were prepared with the polymeric precursor method on alumina substrates. The gas sensing response indicated that CCTO film has high sensor response and selectivity to oxidizing gases and that CCTO films have n-type conductivity [38]. In the other research work, CCTO thin films were prepared by sol-gel method, tested as gas sensors for oxygen, showed n-type conductivity, good sensor response and relatively short response times [40]. In the report of Pongpaiboonkul et, al., the resistance of CCTO thin films sensors rapidly decreased after exposing H_2S which confirmed a typical n-type semiconducting behavior towards a reducing gas. In particular, 9 wt% (~3 at%) Fe-doped CCTO films constitutes an excellent candidate for developing H_2S sensors operating at low-

temperatures of 250 °C, which was more than one order of magnitude higher than that of the undoped CCTO sensor [41].

Furthermore, in the report of Wang et al., CCTO/Ag (composites) were prepared by sintering throughly mixed single phase CCTO powder and different amount of Ag substances from Ag_2O powder. Single phase CCTO powder was synthesized by the solid-state reaction method [42]. The samples were found to consist of Ag deficient insulating surface layers and Ag rich more conductive inner part [42]. With increasing Ag weight fraction, the surface layer becomes thinner and dielectric measurement reveal that apart from the distinct dielectric features for pure CCTO another dielectric relaxation appears near room temperature [42]. It showed that several Ag substances can be added into the CCTO precursors. Silver is arguably one of the best candidates for doping a material towards sensing sulfur containing compounds by means of its very strong interaction with sulfur. This strategy has been successfully applied to other gas sensing materials. Research done by Korotcenkov et al. showed that the surface modification using Ag nanocluster deposition on the SnO_2 surface is effective for optimizing sensor parameters in improving the sensor response of SnO_2 to CO and H_2 operating in atmospheres containing oxidizing gases [43]. Another research work focused on an optical sensor for hydrogen sulfide (H_2S) gas at room temperature based on the chemical reaction of silver nanoparticles (Ag NPs) with H_2S [44]. Thus, in this thesis I will synthesis Ag-doped CCTO films by sol-gel method. My expectation is to fabricate Ag-doped CCTO film gas sensors by obtaining low response rate and still remaining high selectivity towards H_2S. Therefore, it is interesting to investigate the effect of Ag-doping CCTO thin films towards various gases and finally to compare with that of Fe-doped CCTO thin films.

1.2 The aims of the thesis

1. To synthesize Ag-doped $CaCu_3Ti_4O_{12}$ (CCTO) thin films on silicon and alumina substrates by a sol-gel technique using different Ag compounds.

2. To characterize the crystal structure and the surface morphology of Ag-doped on CCTO films by X-ray diffractometry and field emission scanning electron microscopy, respectively.

3. To identify oxidation state of the atoms in the Ag-doped CCTO thin films by X-ray photoelectron spectroscopy.

4. To identify the vibration modes of molecules in the Ag-doped CCTO thin films by Raman spectroscopy.

5. To fabricate Ag-doped CCTO thin film devices for application based on their gas sensing properties and compare the gas sensing result with undoped and Fe-doped CCTO devices.

1.3 Scope of the thesis

In this thesis, the experiment concerning Ag-doped CCTO thin films were prepared by the sol-gel method on alumina substrates along with determination of the gas sensing performances of these films. The different Ag substances such as silver acetate ($AgCH_3CO_2$, MERCK) and silver perchlorate ($AgClO_4$) were added into the precursor solution and also the concentration of Ag was varied. Undoped CCTO and Ag-doped CCTO thin films were sputtered with metal electrode as coplanar patterns for detection the quantity of gases. The effect of Ag doping on gas-sensing properties of CCTO films is characterized towards various gases in order for selectivity and sensor

response such as H_2S, NH_3, H_2, NO_2 and ethanol vapor. The main focus on the gas sensing part will be the enhancement H_2S-sensing performances with Ag-doping in CCTO thin films. Furthermore, a set of films was cast on silicon substrates for material characterization. The CCTO films were structurally characterized by X-ray diffraction (XRD) and Field emission scanning electron microscope (FESEM). Energy dispersive X-ray spectroscopy (EDX), X-ray photoelectron spectroscopy (XPS) and Raman spectroscopy were used to support the evidence of chemical compositions of resulting CCTO thin films.

CHAPTER II
THEORETICAL BACKGROUND

2.1 Calcium Copper Titanate: $CaCu_3Ti_4O_{12}$ (CCTO); undoped and Ag-doped CCTO

The titanate compound $CaCu_3Ti_4O_{12}$ (CCTO) belongs to family of the type, $ACu_3Ti_4O_{12}$ (where A = Ca, Ba, Sr) [45]. $CaCu_3Ti_4O_{12}$ (CCTO) was first synthesized in 1967 by Alfred Deschanvres and his coworkers [45]. The pseudo perovskite structure of $CaCu_3Ti_4O_{12}$ material with cubic structure is caused by octahedral tilting distortion [46]. The dielectric properties of CCTO were discovered by Subramanian and his coworkers in 2000 [47]. They have attracted considerable interest for inventing microelectronic devices because of its giant dielectric constant of about 10^4-10^5 in the temperature range of 100-600 K [48]. Nowadays, there is continuous demand for miniaturization of electronic devices, and interest to develop capacitor materials with high dielectric constant and low loss tangents for applications in microelectronic devices [45, 49]. Therefore, CCTO are widely used for electronic industries, mainly as capacitors, memory devices, power systems and the automotive industry [45]. Furthermore, the electronic conductivity of $CaCu_3Ti_4O_{12}$ (CCTO) materials varies with the composition of the gas atmosphere surrounding them [38]. It has been explored as an alternative candidate to conventional metal oxides for gas-sensing application [39].

2.1.1 Crystal structures

$CaCu_3Ti_4O_{12}$ material has a complex perovskite structure with the space group of Im3 and the lattice parameter of 7.391 Å [45]. It is well known for their ability to produce high dielectric constants which has led to many important applications. The crystal structure of CCTO is centered cubic with four $ATiO_3$ perovskite-type formula units per primitive cell where A is either Ca or Cu. The crystal structure of CCTO is shown in Fig. 2.1.

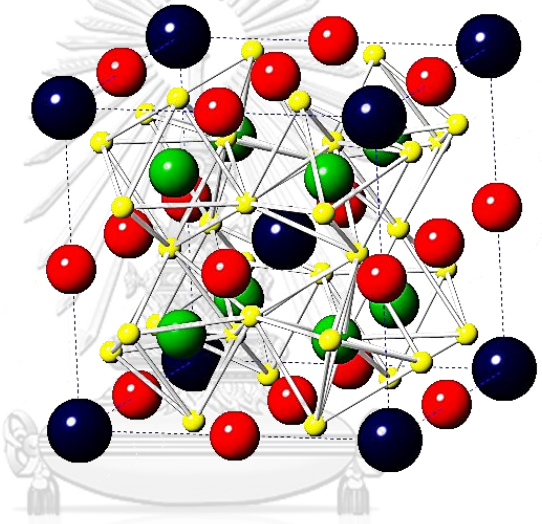

Figure 2.1: Structure of $CaCu_3Ti_4O_{12}$ (CCTO), showing tilted oxygen octahedra. Yellow, dark blue, red, and green atoms are O, Ca, Cu, and Ti, respectively.

As is evident from Fig. 1, the Im3 structure of CCTO can be obtained from an ideal simple-cubic $CaTiO_3$ perovskite by substituting 3/4 of the Ca ions by Cu in a bcc pattern and rotating each TiO_6 octahedron by a fixed angle about one of the four axes [45, 50]. In CCTO, the Ca^{2+} is dodecahedrally coordinated by oxygen ions, while the Cu^{2+} is in square-planar coordination (oxygen as the nearest neighbor) and the Ti^{4+} coordinates six oxygen ions in a slightly distorted octahedron. A tilting of the TiO_6 octahedra is tilted approximately 20° to achieve this coordination environment. The

structure of CCTO was further refined and found to remain centrosymmetric bcc over a wide range of temperatures [45].

2.1.2 Dielectric properties of CCTO

In recent years, the giant dielectric materials have been exhibiting an important significant role in microelectronic devices such as capacitors and memory devices. This is because such devices often require materials with high dielectric constants and low loss tangents. These properties depend upon the particle size, surface morphology and processing conditions (such as the oxygen partial pressure, sintering temperature, and cooling rate), an intrinsic mechanism for the giant dielectric constant seems to be excluded. The high dielectric properties of CCTO are different from classic ferroelectric or relaxors, which show a high dielectric constant near its Curie temperature (associated with change in crystal structure).

In general, the behavior of the high dielectric constant based on the giant dielectric materials can be explained by an internal barrier-layer capacitor model (IBLC model) and Debye-like relaxation behavior. The origin of the high dielectric constant in CCTO has two effects (intrinsic effects and extrinsic effects) on dielectric properties [45].

2.1.2.1 Intrinsic effect

Recently, the perovskite-like body centered cubic material $CaCu_3Ti_4O_{12}$ (CCTO) was reported to have a high dielectric constant of 10^4-10^5 at a wide range of temperatures from 100 to 600 K. However, the dielectric constant decreased in the factor of 100 at temperatures below 100 K along with a broad peak in the loss tangent. Debye model was used to explain the dipolar relaxation process where the dielectric constant is expressed by the Equation (2.1).

$$\tilde{\varepsilon} = \varepsilon_{\infty} + \frac{P_0\tau(1+i\omega\tau)}{1+i(\omega\tau)^2} \quad (2.1)$$

where $P_0\tau = \varepsilon_0 - \varepsilon_{\infty}, P_0$ is the dipole moment, ε_0 and $\varepsilon_{\infty}$are the dielectric constant at low frequency and the dielectric constant at high frequency, respectively. And τ is the relaxation time. The intrinsic properties means that the large dielectric response would be present in a perfectly stoichiometric, defect-free, single-domain crystal of CCTO. In CCTO, the dielectric constant and polarizability are enhanced by tension in Ti-O bonds because a tilting of the TiO_6 octahedra was accommodated by Cu^{2+} square planar coordination [51].

2.1.2.2 Extrinsic effect

For the extrinsic effect, internal barrier layer capacitance (IBLC) has been employed to explain the observed giant dielectric response. Internal microstructure of the giant dielectric materials was established to explain the large capacitance behavior [52]. The effects caused by conductive grain and insulating barrier-layer (grain boundary). Figure 2.2 shows the typical IBLC structure for CCTO materials [53].

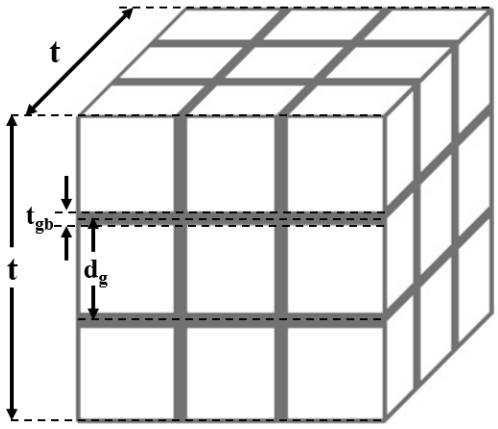

Figure 2.2: Internal barrier layer capacitor (IBLC) structure for CCTO: grains are represented schematically by cubes (solid lines).

From Fig. 2.2, the typical IBLC structure for CCTO materials, it can be calculated the total capacitance from each capacitance (C_i) in CCTO. We can be assumed that $d_g \gg t_{gb}$,

$$C_i = \frac{\varepsilon_{gb}\varepsilon_0 d_g^2}{t_{gb}} \quad (2.2)$$

According to the Equation (2.2), d_g is grain size

t_{gb} is boundary layer thickness

ε_{gb} is dielectric constant of insulating barrier-layer (grain boundary)

$$C = \frac{\varepsilon_{gb}\varepsilon_0 d_g}{t t_{gb}} \quad (2.3)$$

And the capacitance per the unit area (C) can be calculated in the Equation (2.3). From $C = \frac{\varepsilon_r \varepsilon_0}{t}$, t is the total vertical thickness of IBLC structure and the colossal dielectric constant (ε_r) of heterogeneous electro-ceramic material can be revealed as the Equation below.

$$\varepsilon_r = \frac{\varepsilon_{gb} d_g}{t_{gb}} \quad (2.4)$$

It can be easily understood that the bigger grain size (d_g) with thinner grain boundaries (smaller t_{gb}) in the samples affect higher dielectric constant (ε_r) as extrinsic effect. Each grain boundary or grain type contribution is described by one RC circuit as shown in Fig. 2.3 that the relationship refers to the Maxwell-Wagner type polarization with a relaxation behavior [53].

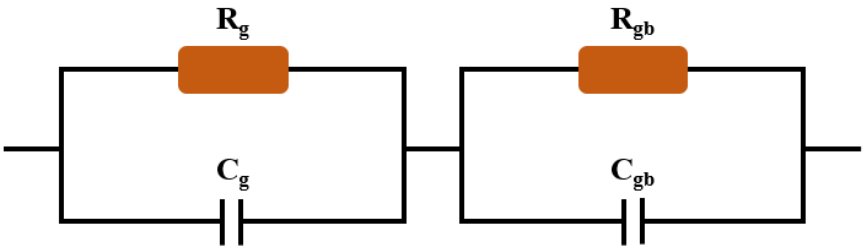

Figure 2.3: Schematic the RC circuit consisting of a resistor and capacitor in the grain (R_g, C_g) and the grain boundary (R_{gb}, C_{gb}).

CCTO grains exhibit as n-type semiconducting behaviors with boundary phases of p-type carriers consisted of CuO. Research done by Jung-Hyuk Koh et al. showed that the resulting Ag-doped $CaCu_3Ti_4O_{12}$ powders were analyzed in terms of the dielectric properties and sintering temperature. Impedance spectroscopy indicates that grain and grain boundary resistances of the 2 mol% Ag-doped CCTO ceramics has been decreased compared with the undoped CCTO ceramics [54].

2.1.3 Gas sensing properties of CCTO

Gas sensing mechanisms of CCTO sensors towards different concentrations of test gases in purify air. From previous research, Felix et al. have reported that CCTO thin films are a typical n-type semiconducting behavior which can be explained as following [38, 41]. The most accepted mechanism is associated to the transfer of free charge carriers between the semiconductor surface and the absorbed molecules. The mechanism of the n-type semiconductors with oxygen as the analyte gas called the ionosorption model. Recently, a theoretical study has proposed that oxygen vacancy defects can react with crystal defects and that can affect the electronic structure of CCTO, depending on the oxygen regime during the synthesis conditions [38]. It can be

leaded to a different conductivity type and identified the oxygen-related intrinsic effects while film processing as the main mechanism responsible for ruling the type of gas sensing response and conductivity in CCTO thin films.

In the previous work done by the previous Ph.D. student in our laboratory, Fe-doped CCTO showed fascinating gas sensing properties towards H_2S against NH_3, CO, C_2H_2, CH_4, ethanol and NO_2 including the ability to detect low concentration of H_2S [41]. CCTO contains copper ions in its structure which is capable of interaction with sulfide. Therefore, it may be expected that changes in the conduction band occupy of CCTO can occur by adsorption of sulfide species leading to the change in its electrical properties. Even pure CCTO thin films could selective and sensitive to H_2S gas but the sensor response is quite moderate (~ 10). These studies have shown that the sensor response of 9 wt% Fe-doped CCTO films towards H_2S increased 10 times (~ 126) relative to pure CCTO [41]. The details of H_2S gas sensing data and the mechanism will be explained in Section 2.3.4.

2.2 Sol-gel process

Sol-gel process is a wet-chemical process for producing solid materials from small molecules. This method is used for the fabrication of metal oxide materials e.g. ceramics, thin films at low temperature. Sol-gel process consists in the chemical transformation of a liquid (the sol) into a gel state and with subsequent post-treatment and transition into metal oxide material. The main benefits of sol-gel processing are the high purity and uniform nanostructure achievable at low temperatures. It based on control of hydrolysis, water condensation and alcohol condensation reactions as seen in the Equations (2.5)-(2.7),

Hydrolysis:

$$M - O - R + H_2O \rightarrow M - OH + R - OH \quad (2.5)$$

Water condensation:

$$M - OH + HO - M \rightarrow M - O - M - H_2O \quad (2.6)$$

Alcohol condensation:

$$M - OH - R + HO - M \rightarrow M - O - M + R - OH \quad (2.7)$$

where M is a metal, -OR is an alkoxide groups and -OH is hydroxyl group. During the hydrolysis reaction, the alkoxide groups (-OR) are replaced with the hydroxyl group (OH) through the addition of water. Subsequent condensation reaction involving M-OH group produces M-O-M bonds with product of water (water condensation) or alcohol (alcohol condensation) [55]. From these Equations, it can be leaded to the formation of a sol.

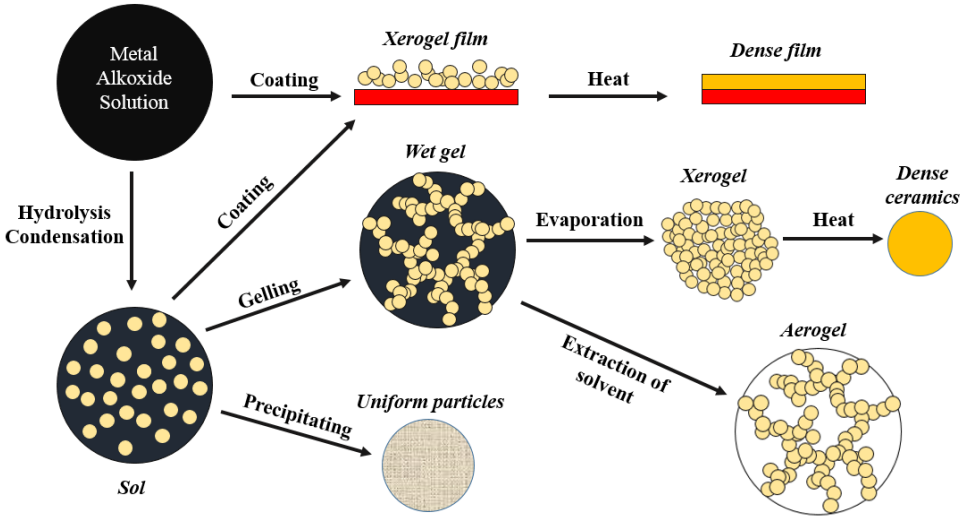

Figure 2.4: Schematic illustration of the different stages and routes of the sol-gel technique.

Figure 2.4 shows that the sol can be applied with the different stages and routes of the sol-gel process. Thin films, normally less than 1 μm in thickness, could be

formed by dipping or coating without cracking [56]. In this thesis, I focus on spin coating technique for thin films preparation. The sol is produced by spin coating and deposited on substrates for various applications that be used. After that, the drying and sol-gel densification are used to the films formation. These processes will be explained in the next sections.

2.2.1 Spin coating

Spin coating is used for making a thin coating on relatively flat substrates. There are three phases (spin-up, spin-off and evaporation) of spin coating process. These phases of spin coating process are shown in Fig. 2.5.

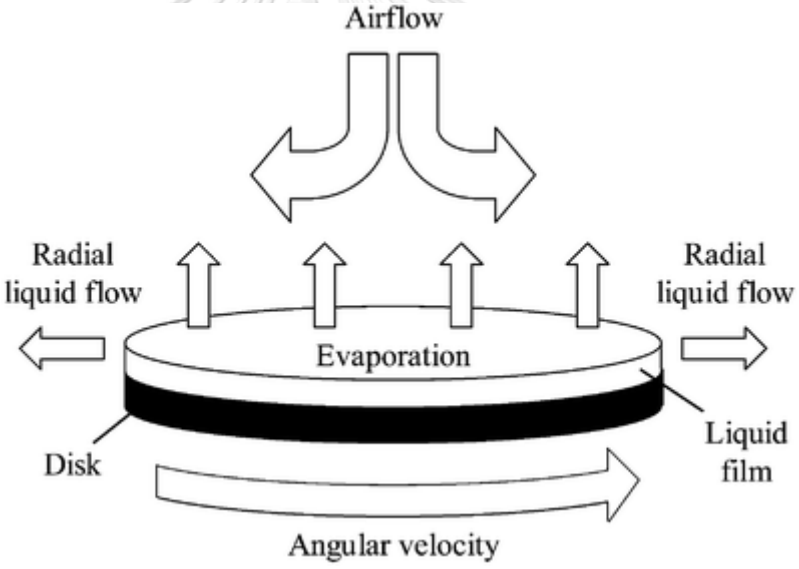

Figure 2.5: Schematic illustration of the major spin coating process [57].

For the spin-up phase, the substrate is accelerated to the final rotation speed in 0.5-2 seconds and the final rotation speeds in the range of 500-10,000 rpm (usual 2,000-5,000 rpm). Spin-up removes most of the solution which has been initially deposited on the substrate. In the spin-off phase, high-speed spinning casts solution off from the edge of the substrate. Centrifugal rotation forces are balanced by viscous dissipation effect of the solution. Then, spin speed that actually slow down because the coating

thickness is reduced. Edge effects are often seen because the fluid flows uniformly outward, but must form droplets at the edge to be flung off. Thus, there may be a small bead of coating thickness difference around the rim of the final wafer. It depends on the surface tension, rotation rate, viscosity, etc. At the last phase, the evaporation of any vaporing solvent species will become the important process occurring in the spin coating process. Evaporation starts to remove only the solvent. The viscosity of the film increases when the solvent may be removed to a certain extent in the spin-off stage [58].

In addition, the interaction between substrate and solution layer are strongly compared than interaction between solution surface layer and air. The film thickness can be simplified to the form $h \propto \omega^{-2/3}$ where h is film thickness and ω is spinning speed [58, 59]. Furthermore, it depends on viscosity and solution concentration. After spinning is stopped many applications require that heat treatment or "Drying" of the coating be performed.

2.2.2 Drying

The gel has a high ratio of water and three dimensional inter-connected pores inside the structure. Before the pore is closed during the densification process, drying is needed to remove the liquid trapped in the interconnected pores. The stages of drying in details can be discussed in the factors affecting stress development of various strategies for avoiding warping and cracking. The first stage of drying is called the constant rate period (CRP). The gel is still flexible and shrinks as liquid evaporates. The second stage, critical point, the gel becomes stiff and resists further shrinkage, the liquid begins to recede (contact angle, θ) into the pores (radius, a), the tension (P) in

the liquid is defined to

$$P = \frac{2\gamma \cos\theta}{a} \tag{2.8}$$

As the gel shrinks, the tension in the pores increases and the vapor pressure of the liquid in the pores decreases according to

$$p_v = p_0 \exp\left(\frac{PV_m}{R_g T}\right) \tag{2.9}$$

where V_m is the molar volume of the liquid and P is the tensile stress in the liquid

The third stage is called the *first falling-rate period* (FRP1). The rate of evaporation decreases and the temperature of the surface rises above the wet-bulb temperature. A thin liquid film remains on the pore walls and flows to the surface. At the same time, some liquid evaporates within the unsaturated pores and the vapor is transported by diffusion [60].

At the last stage, drying is said to enter the *second falling rate period* (FRP2), where evaporation occurs inside the body as shown in Fig. 2.6. The temperature of the surface approaches the ambient temperature and the rate of evaporation becomes less sensitive to external conditions (temperature, humidity, draft, etc.). Since evaporation occurs inside the body (at the pendular-funicular boundary), the surface rises above the wet-bulb temperature. The vapor pressure increases with the temperature, so the concentration gradient may cause some diffusion toward the interior. The ambient vapor pressure is low at near the outer surface [60].

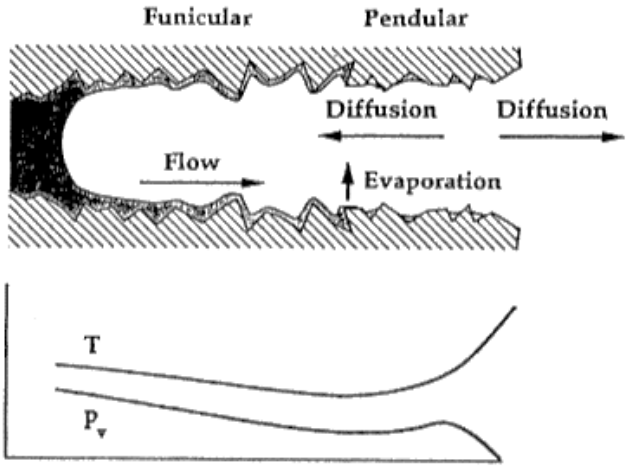

Figure 2.6: Schematic illustration of transport during the second falling rate period [60].

2.2.3 Sol-gel densification

The final process of the sol-gel technique is densification. The densification process will be done by heating the sol-gel thin film with high temperature in order to make a smoother and compact surface. After the sol-gel materials were annealed at high temperature, the pores were eliminated and the density of its became equivalent. In the previous study, the most obvious physical change that occur when a gel is heated above room temperature for a multicomponent borosilicate gel during heating at 0.5 °C/min [61]. Densification stages are shown in Fig. 2.7. The densification curve in the Fig. 2.7 is composed of three distinct portions. In stage I, the weight loss occurs with small shrinkage below the temperature of 200 °C. In stage II, both shrinkage and weight loss are substantial at the temperature in the range of 150-700 °C. When the pores are completely in the closed form that interconnected pore charnels are closed off isolating porosity above 500 °C, the rate of densification is reduced as shown in the final stage within no more weight loss. The densification temperature that be used depending on

the surface areas in the structure, the dimension of the pores and the degree of connection of the pores.

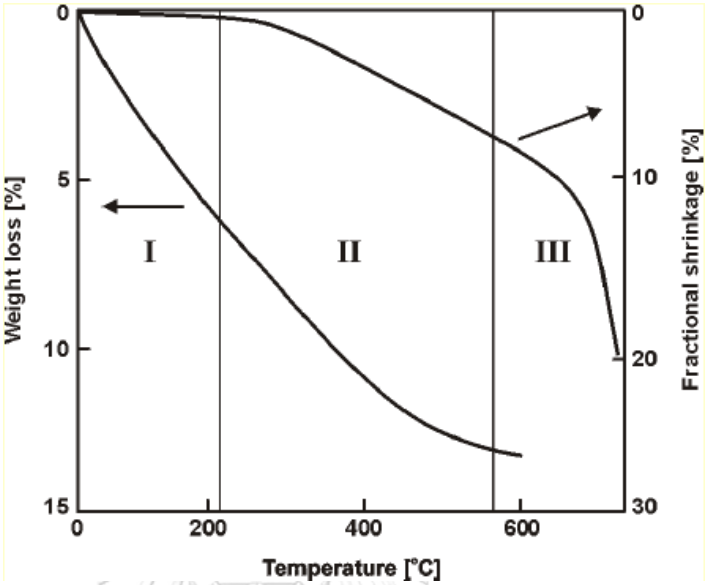

Figure 2.7: Densification stages with fractional linear shrinkage and percent weight loss for a multicomponent borosilicate gel [61].

2.3 Metal oxide gas sensor

2.3.1 Working principle of gas sensor

Gas sensors are devices that can transform the chemical signature of an analytic gas into an electronic signal and are one of the important components of electronic nose technology. At the beginning of the sensing measurement, the sensor is exposed to pure air exhibited a high resistance due to the reaction between the chemisorbed oxygen on the surface and electrons from conduction band. It can be explained by physical adsorption process in the Equation (2.10) and chemical adsorption in the Equations (2.11)-(2.13).

$$O_2(gas) \leftrightarrow O_2(ads) \quad (2.10)$$

$$O_2(ads) + e^-(conduction\ band) \leftrightarrow O_2^-(ads) \quad ; \text{T} < 200\ ^\circ\text{C} \quad (2.11)$$

$$O_2^-(ads) + e^-(conduction\ band) \leftrightarrow 2O^-(ads) \quad ; 200\ ^\circ\text{C} < \text{T} < 400\ ^\circ\text{C} \quad (2.12)$$

$$O^-(ads) + e^-(conduction\ band) \leftrightarrow O^{2-}(ads) \quad ; 200\ ^\circ\text{C} < \text{T} < 400\ ^\circ\text{C} \quad (2.13)$$

When the metal oxide sensors are exposed to pure air, oxygen molecules can be adsorbed on the surface of sensor as a donor or acceptor of charge carriers (Receptor function). Because of the strong electronegativity of oxygen atom, electrons from conduction band of metal oxide materials react with the adsorbed oxygen molecules to produce ionized oxygen species such as O_2^-, O^- [62]. These Equations depend on operate temperature that the adsorbed oxygen molecules receive one negative charge as shown $O_2^-\ (ads)$ at low temperature between 150 and 200 °C. And it is considered as dissociative atom as seen $O^-\ (ads)$ and $O^{2-}\ (ads)$ at high temperature between 200 and 400 °C. The electron concentration would be decreased in the chemical adsorption process. Schematic diagram of band bending after chemisorption of charged species is

shown in Fig. 2.8 where E_C, E_V, and E_F denotes the energy of the conduction band, valence band, and the Fermi level, respectively, while Λ_{air} denotes the thickness of the space-charge layer, and eV surface denotes the potential barrier.

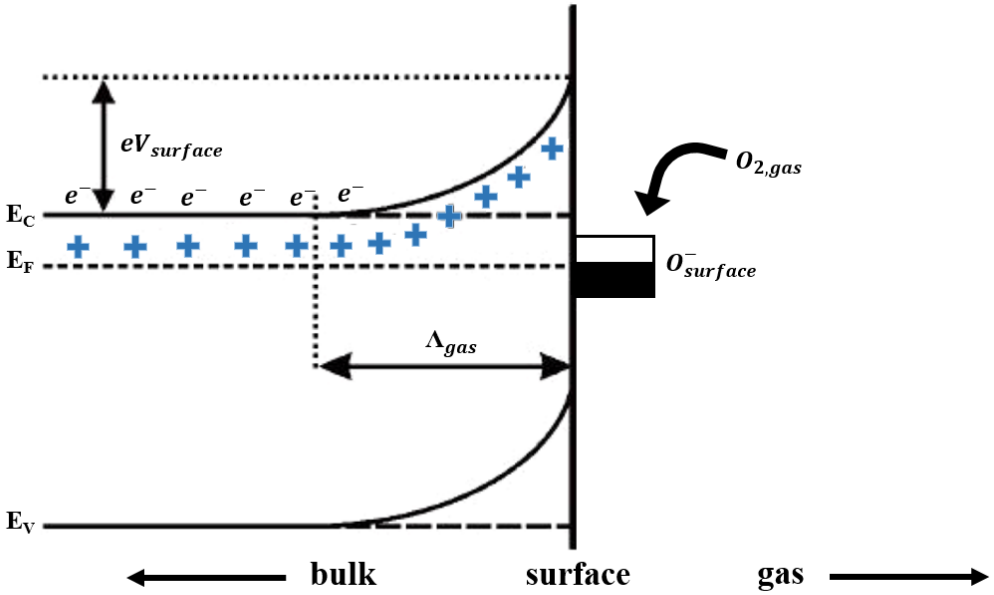

Figure 2.8: Schematic diagram of band bending after chemisorption processes.

It can be seen that the resistance of metal oxide sensors increase. After the test gases was flowed into the reaction chamber, the test gas molecules could be chemisorbed on the surfaces of them according to gas sensing mechanism in the Chapter 5.

If we focus on reaction with a reducing gas, the working principle of the gas sensors is schematically shown in Fig. 2.9. The oxygen adsorption and reaction with a reducing gas occurs on the surface.

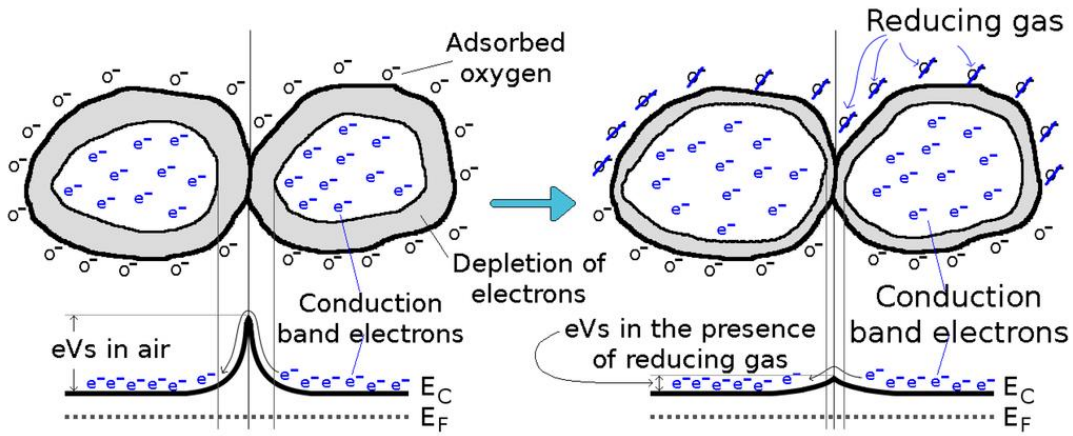

Figure 2.9: Schematic of metal oxide gas sensor where the oxygen and reducing gas can penetrate to interact with each grain [63].

2.3.2 Characteristics of metal oxide gas sensor

In the previous section, the gas sensing mechanism was explained by the ionosorption model. This section, the change of the sensor resistance upon exposure to the target gas in the case of n-type and p-type metal oxide sensors is considered. There are two cases on the characteristics of metal oxide gas sensor.

The first case, oxidizing gas will be considered. It can be reacted with the oxygen ion and keep the electron at the surface and the electron concentrations in the metal oxide will be decreased. In the n-type metal oxide sensors, the majority of carriers are electrons and the conductance decrease after being exposed to oxidizing gas. For the p-type metal oxide sensors, the majority of carriers are holes. The electron concentrations in the metal oxide will be increased. Therefore, the conductance of p-type metal oxide sensors will increase after being exposed to oxidizing gas.

The second case, when the reducing gases are exposed into the flow chamber. The electrons obtained from the chemical reaction in the adsorbed oxygen ion forming

process are given back to the conduction band as shown in Fig. 2.10 below. In the n-type metal oxide sensors, these electrons will increase the carrier concentration and affect to a decrease in the resistance of sensors. For the p-type metal oxide sensors, the electrons go back in to the valence band and recombine with the holes that results in reducing the concentration of holes and affects to an increase in the sensor resistance.

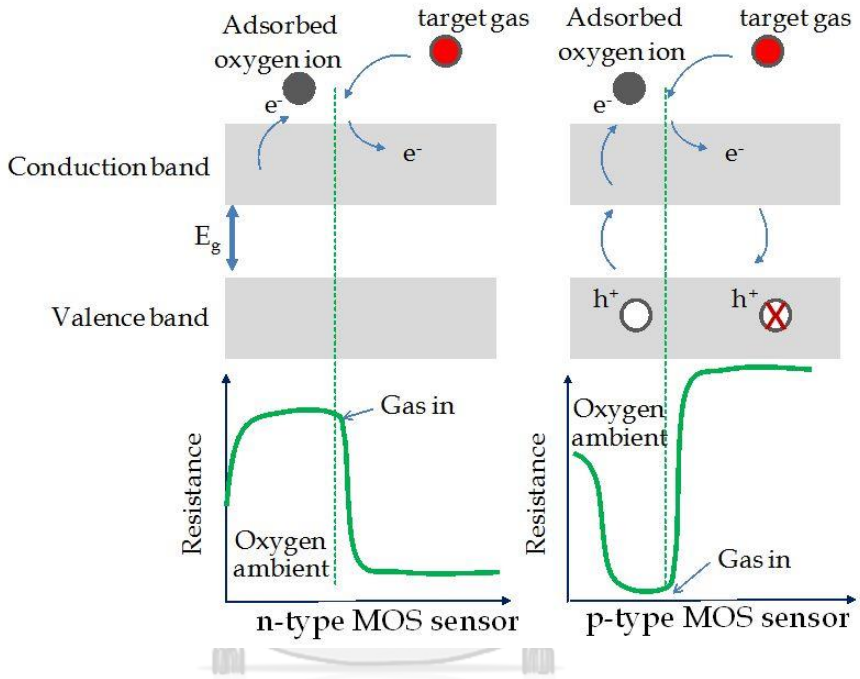

Figure 2.10: Schematic diagram for change of the sensor resistance upon exposure to the target gas (reducing gas) in the case of n-type and p-type metal oxide gas sensors [64].

Gas-sensing performances could be described in terms of the response time, the recovery time, the sensor response and the selectivity. The response time and recovery time are defined as the time that they are different sensor signals between 90% of its steady state and 10% of the initial value (after exposure to the target gas). Figure 2.11 shows a typical signal of a sensor made from n-type semiconductor illustrating the response time and the recovery time under reducing gas. If the recovery time and the

response time values are small number, the performances of such sensor will be considered to be efficiency.

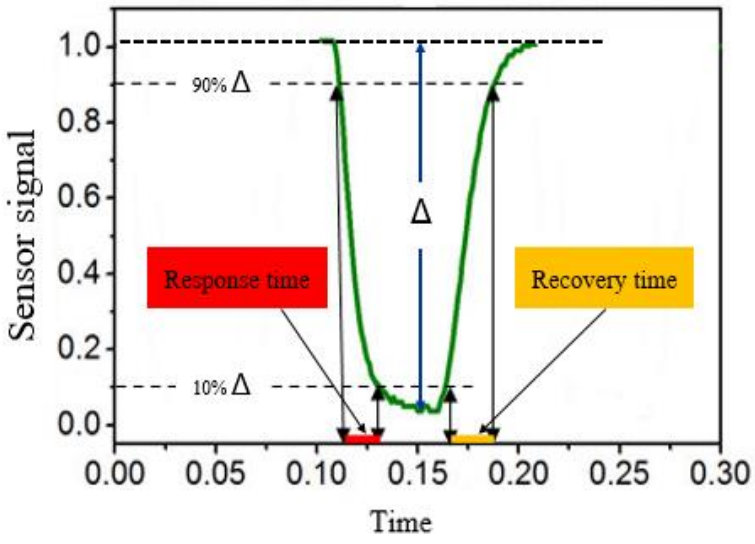

Figure 2.11: A typical signal of a sensor made from n-type semiconductor under reducing gas as a function of time.

2.3.3 Strategy for improvement of gas sensing performance

Surface decoration with noble metal is a powerful method for improvement of gas sensing performance. The working principle of dopant for enhancing the gas sensing performance of pure metal oxide could be described in the catalytic effect.

To provide $k_2 \ll k_{-1}$, the rate of reaction of adsorbed A molecules is much greater than the rate of desorption of unreacted A. Surface reactions can often be explained by the mechanism,

$$A(g) \underset{k_{-1}}{\overset{k_1}{\Leftrightarrow}} A(ads) \xrightarrow{k_2} Products \qquad (2.14)$$

For unimolecules, the rate of product formation is $k_2\Theta_A$ where Θ_A is the surface coverage of A that is number of adsorption sites occupied. The rate of surface reaction (k_r) can be written in the Equation 2.15.

$$k_r = k_2\Theta_A = \frac{k_2 K_A P_A}{1 + K_A P_A} \quad (2.15)$$

where P_A is partial pressure of A, K_A is the adsorption equilibrium constant. The simple Langmuir isotherm equation for adsorption of a single adsorbate on a single-site surface is still frequently applied to ion-exchange reactions [65]. It can be used to determine Θ_A, giving

$$\Theta_A = \frac{K_A P_A}{1 + K_A P_A} \quad (2.16)$$

From the Equation 2.16, the rate of reaction is considered by two limiting rate laws, corresponding to the two extreme behaviors of the Langmuir isotherm:

1. At low pressure ($P_A \longrightarrow 0$), Θ_A is very small.

$$k_r = k_2\Theta_A = K_2 K_A P_A \quad (2.17)$$

2. At high pressures Θ_A is approximately equal to unity, and the reaction is zero order

$$k_r = k_2 \quad (2.18)$$

For biomolecules, the reaction occurs between two molecules which adsorb on different types of surface sites. If we concern the reaction with adsorbed oxygen species, the surface reactions can often be explained by the mechanism,

$$A(ads) + O_2^-(ads) \xrightarrow{k_2} Products \quad (2.19)$$

The reaction rate (k_r) is then,

$$k_r = k_2\Theta_A\Theta_{O_2^-} = k_2\left(\frac{K_A P_A}{1 + K_A P_A}\right)\left(\frac{K_{O_2^-} P_{O_2^-}}{1 + K_{O_2^-} P_{O_2^-}}\right) \quad (2.20)$$

where $\Theta_{O_2^-}$ is constant, giving

$$k_r = (const.)k_2\Theta_A \quad (2.21)$$

$$k_r = k_{eff}\Theta_A \quad (2.22)$$

From the Equation 2.22, it is a linear function with the effective response rate (k_{eff}) that be the slope of this function. The dependence of the effective rate on the noble metal doping concentration represents the reaction order on the catalyst in a chemical kinetic sense.

2.3.4 Gas-sensing performances with Fe-doping in $CaCu_3Ti_4O_{12}$ thin films

In the report of Pongpaiboonkul et, al., the selectivity of CCTO sensors were assessed toward H_2S, NH_3, NO_2, C_2H_5OH, CO, CH_4 and C_2H_2. Fe dopants greatly enhanced the sensor response and selectivity to H_2S as shown in Fig. 2.12. At high H_2S concentration of 10 ppm, the response time decreases from ~40 s to ~8.5 s and the recovery time reduces from ~1100 s to ~500 s as the input Fe-doping level increase from 0 to 9 wt% [41].

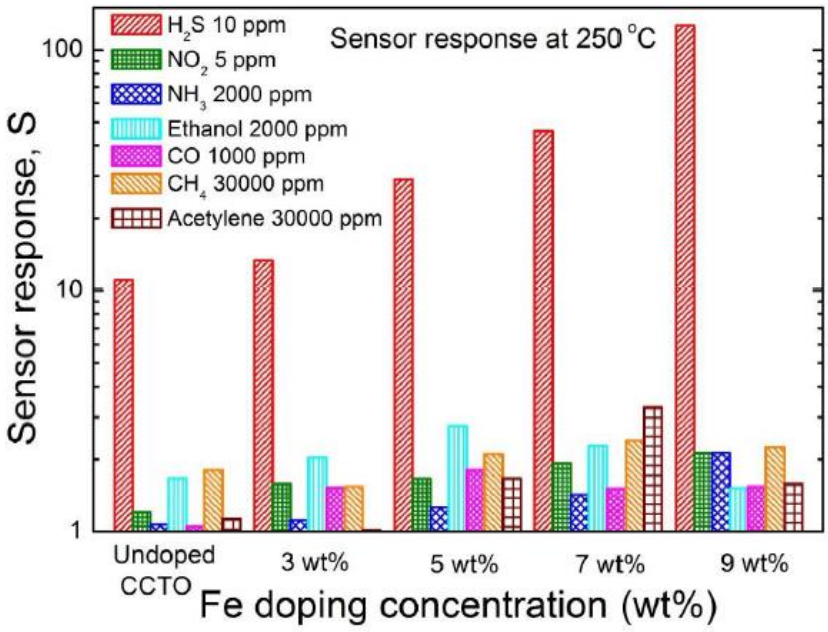

Figure 2.12: Selectivity of histogram of CCTO sensors with different Ag-doping concentrations [41].

The roles of Fe-dopant on gas-sensing mechanisms of CCTO sensor may be explained based on electronic and catalytic effects of substitutional p-type Fe dopants. Generated electrons in conduction band according to the defect reaction represented in Kröger–Vink notation can be described in the Equation 2.23,

$$O_O^x \rightarrow V_O^{\bullet\bullet} + 2e' + \frac{1}{2}O_2 \qquad (2.23)$$

where O_O^x, $V_O^{\bullet\bullet}$, $e'$and O_2 are oxygen site, oxygen vacancy, electron with a single negative charge and oxygen gas, respectively.

Near surface, the CCTO structure interacts with oxygen gas. Some of adsorbed oxygen ions can interact with oxygen vacancies in the lattice. With Fe doping, Fe^{3+} ions substitute on to Ti^{4+} sites. The substitution results in the creation of oxygen vacancies which will accept oxygen gas in air while sintering. It can be explain in Equations 2.24-2.25.

$$Fe_2O_3 \rightarrow 2Fe'_{Ti} + 3O_O^x + V_O^{\bullet\bullet} \quad (2.24)$$

$$V_O^{\bullet\bullet} + \frac{1}{2}O_2 \rightarrow 2h^{\bullet} + O_O^x \quad (2.25)$$

where Fe_2O_3, Fe'_{Ti}, and $h^{\bullet}$ are the quasi-Fe_2O_3 dopant molecule, Fe-Ti substitutional site and hole, respectively. The generated holes will recombine with existing electrons, leading to the annihilation of electrons and the increase of electrical resistance.

When exposing the CCTO film to H_2S (reducing gas), H_2S molecules will adsorb on the sensor surface according to the following Equations 2.26-2.27,

$$H_2S + 3O^-(ads) \rightarrow SO_2 + H_2O + 3e^- \quad (2.26)$$

$$H_2S + 3O^{2-}(ads) \rightarrow SO_2 + H_2O + 6e^- \quad (2.27)$$

The electrons from the surface oxygen species will be released into CCTO conduction band. In addition, Fe dopant in CCTO could be an effective catalyst that can selectively enhance the reducing reaction and response rates with H_2S according to:

$$FeO_x + x \cdot H_2S \rightarrow FeS_x + x \cdot H_2O \quad (2.28)$$

$$FeS_x + \frac{3}{2}x \cdot O_2 \rightarrow FeO_x + x \cdot SO_2 \quad (2.29)$$

CHAPTER III
CHARACTERIZATION TECHNIQUES

For material characterization, we will focus on X-ray Diffraction (XRD), Field Emission Scanning Electron Microscopy (FESEM), Raman Spectroscopy, X-ray Photoelectron Spectroscopy (XPS) technique. These characterization techniques will be explained with the working principle and we will specify the measurements that the details of its were described in this section.

3.1 X-ray Diffraction (XRD)

X-ray diffraction (XRD) technique is an analytical technique widely used to identify the phases in the crystalline material for crystal structure examination. XRD has wide variety applications such as analyzing films as thin as 50 angstroms for texture and phase behaviors, determining crystallite size from the Scherrer Equation, detecting the preferential orientation of the films with the secondary phases or impurity phases in the films and etc. In this section, we will first explain the generation of X-ray and follow by working principle of XRD.

3.1.1 Generation of X-ray

X-rays which are produced from X-ray tube. X-ray are short wavelength in the range of 0.01 to 10 nanometers and high energy waves of electromagnetic radiation in the range of 200 eV to 1 MeV which are characterized by wavelength or photon energy as shown in Fig. 3.1. X-rays are produced by high speed electrons when accelerated electrons collide with the target.

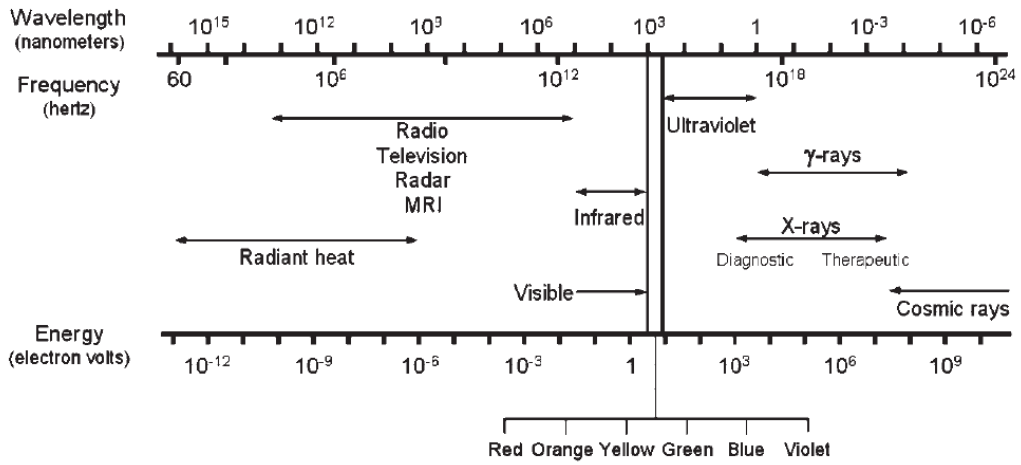

Figure 3.1: The electromagnetic spectrum, presented as a function of wavelength, frequency, and energy. X-rays comprises the high-energy portion of the electromagnetic spectrum [66].

X-ray can be divided into two types of continuous X-ray and characteristic X-ray. It can be shown in Fig. 3.2. Events 1, 2, and 3 describe the incident electrons interacting in the vicinity of the target nucleus, resulting in bremsstrahlung production caused by the deceleration and change of momentum, with the emission of a continuous energy spectrum of x-ray photons. Event 4 demonstrates characteristic radiation emission, where an incident electron with energy greater than the K-shell binding energy collides with and ejects the inner electron creating an unstable vacancy. An outer shell electron transitions to the inner shell and emits an x-ray with energy equal to the difference in binding energies of the outer electron shell and K shell that are "characteristic" of tungsten [67].

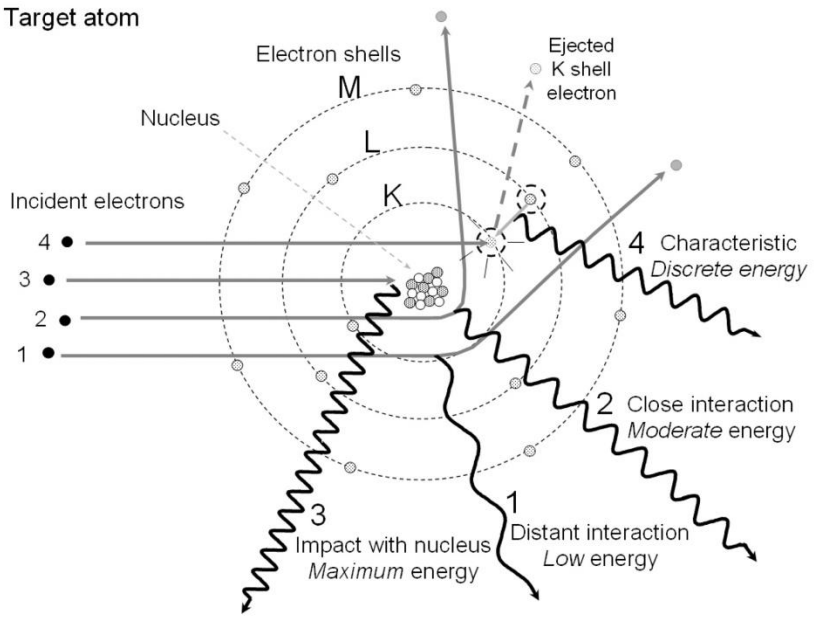

Figure 3.2: X-ray production by energy conversion.

For properties of the Continuous Spectrum, the intensity is zero up to a certain wavelength-short wavelength limit (λ). The kinetic energy of the decelerated electrons converts to the energy of X-ray radiation as shown in the following Equation (3.1).

$$E_k = \frac{1}{2}mv^2 = eV \qquad (3.1)$$

where E_k is the kinetic energy

m is mass of the electron (9.11×10^{-31} kg)

v is electron velocity (m/sec)

e is electron charge (1.6×10^{-19} C)

V is applied voltage (V)

The electrons transfer all their energy into photon energy. It can be described with the Equation (3.2).

$$eV = h\nu \qquad (3.2)$$

where h is plank's constant ($6.62607004 \times 10^{-34}$ J·s), ν is the frequency of the radiation (Hz). Combining this relation with $V = \frac{c}{\lambda}$, the wavelength of X-ray radiation, λ, is related to the acceleration voltage of electrons (V) as shown in the following Equation (3.3):

$$\lambda = \frac{12.398 \times 10^3}{V} \quad (3.3)$$

The total X-ray energy emitted per second depends on the atomic number Z of the target material and on the X-ray tube current. This total X-ray intensity is given by Equation (3.4).

$$I = AiZV^m \quad (3.4)$$

where A is proportionality constant, i is tube current (measure of the number of electrons per second striking the target) and m is the constant ≈ 2.

For the properties of the characteristic spectrum, the diffraction peak with a specific wavelength is created when a hole in the inner shell, created by a collision event, is filled by an electron from higher energy shell. Let a K-shell electron be knocked out and the vacancy can be filled by an electron from the L-shell (K_α radiation) or the M-shell (K_β radiation). Table 3.1 shows characteristic wavelength values (in Å) for common anode materials. There are several lines in the K-set. The strongest are $K_{\alpha_1}, K_{\alpha_1}$ and K_{β_1}. Usually only the K-lines are useful in X-ray diffraction.

Table 3.1: The X-ray characteristics of usual target materials [67].

Materials	**Atomic number**	**Some commonly used X-ray *K* wavelengths (Å)**				**Optimum Voltage (kV)**
		K_{α}**(av.)**	K_{α_1}	K_{α_2}	K_{β_1}	
Cr	24	2.29100	2.28970	2.29361	2.08487	40
Fe	26	1.97376	1.93604	1.93998	1.75661	40
Cu	29	1.54184	1.54056	1.54439	1.39222	45
Mo	42	0.71073	0.70930	0.71359	0.63229	80

3.1.2 Working principle of XRD

The principle of XRD is based on Bragg's law which scans the sample through a range of 2θ (scattering angles) at which peaks of strong scattered intensity may occur, composition is measured. It can be identified positions and intensities of diffraction peaks which are unique to a given chemical compound. The scattering of a monochromatic X-ray beam with one wavelength from crystal planes is shown in Fig. 3.3. This schematic set up is called θ-2θ scan.

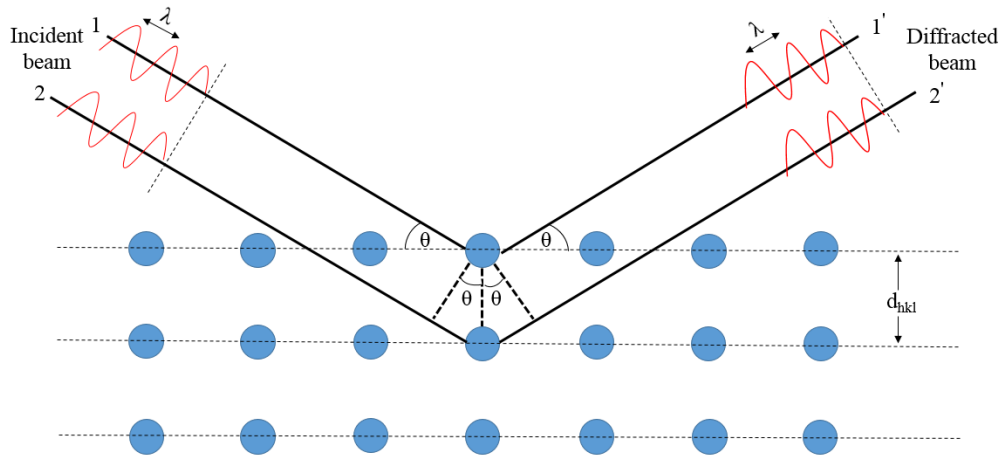

Figure 3.3: Schematic of diffraction to prove Bragg's law.

When an X-Ray beam with a known wavelength is incident to a crystalline solid, the crystalline planes will make the diffraction, according to the general relationship between the wavelength of the incident X-rays, angle of incidence and d-spacing is known as Bragg's Law:

$$2d_{hkl} \sin \theta_{hkl} = n\lambda \tag{3.4}$$

where d_{hkl} is the distance between atomic layers in a crystal.

θ_{hkl} is an incident angle which is the angle between the lattice plane and the incident beam.

λ is the wavelength of the incident X-ray beam.

n is an integer.

The distance between atomic layers in a crystal can be calculated by d-spacing formulas as shown in Table 3.2.

Table 3.2: Formulas of the distance between atomic layers in a crystal structure [68].

Crystal system	***d*-spacing formulas**
Cubic $a = b = c$ $\alpha = \beta = \gamma = 90^{\circ}$	$\frac{1}{d^2} = \frac{h^2 + k^2 + l^2}{a^2}$
Tetragonal $a = b \neq c$ $\alpha = \beta = \gamma = 90^{\circ}$	$\frac{1}{d^2} = \frac{h^2 + k^2}{a^2} + \frac{l^2}{c^2}$
Orthorhombic $a \neq b \neq c$ $\alpha = \beta = \gamma = 90^{\circ}$	$\frac{1}{d^2} = \frac{h^2}{a^2} + \frac{k^2}{b^2} + \frac{l^2}{c^2}$
Hexagonal $a = b \neq c$ $\alpha = \beta = 90^{\circ}, \gamma = 120^{\circ}$	$\frac{1}{d^2} = \frac{4}{3}\left(\frac{h^2 + hk + k^2}{a^2}\right) + \frac{l^2}{c^2}$
Monoclinic $a \neq b \neq c$ $\alpha = \beta = 90^{\circ}, \gamma \neq 120^{\circ}$	$\frac{1}{d^2} = \frac{1}{sin^2\beta}\left(\frac{h^2}{a^2} + \frac{k^2 sin^2\beta}{b^2} + \frac{l^2}{c^2} - \frac{2hlcos\beta}{ac}\right)$
Triclinic $a \neq b \neq c$ $\alpha \neq \beta \neq \gamma \neq 90^{\circ}$	$\frac{1}{d^2} = \frac{1}{V^2}[h^2b^2c^2sin^2\alpha + k^2a^2c^2sin^2\beta + l^2a^2b^2sin^2\gamma$ $+ 2hkabc^2(cos\alpha cos\beta - cos\gamma)$ $+ 2kla^2bc(cos\beta cos\gamma - cos\alpha)$ $+ 2hlab^2c(cos\alpha cos\gamma - cos\beta)$

The CCTO structure type is derived from the cubic perovskite structure. The X-ray measurement was collected by using CuKα_1 (λ = 1.54056 Å) radiation with 40 kV and 40 mA in the 2θ range of 20° to 80° with scan step about 0.02°. For cubic crystal systems, all three linear parameters are identical, so a single lattice constant is used to describe a cubic unit cell. It can be calculated by the Equations (3.5)-(3.8).

$$\frac{1}{d^2} = \frac{h^2+k^2+l^2}{a^2} \tag{3.5}$$

From Bragg's Law, we can get the Equation (2.6).

$$d_{hkl} = \frac{n\lambda}{2sin\theta_{hkl}} \tag{3.6}$$

By combining (3.5) and (3.6), we can gain a new Equation:

$$\left(\frac{n\lambda}{2a}\right)^2 = \frac{sin^2\theta}{h^2+k^2+l^2} \tag{3.7}$$

$$sin^2\theta = \frac{n^2\lambda^2}{4a^2}(h^2+k^2+l^2) \tag{3.8}$$

For a particular incident x-ray wavelength and cubic crystal of unit cell size a, this Equation predicts all possible Bragg angles at which diffraction can occur from planes (*hkl*).

3.2 Field Emission Scanning Electron Microscopy (FESEM)

The field emission scanning electron microscopy (FESEM) uses a focused beam of electrons to generate an image or to analyze the specimen. It is developed from ordinary SEM. Electrons are liberated from a field emission source that is the main differences between FESEM and SEM (thermionic emission source). Schematic diagram of FESEM is shown in the Fig. 3.4.

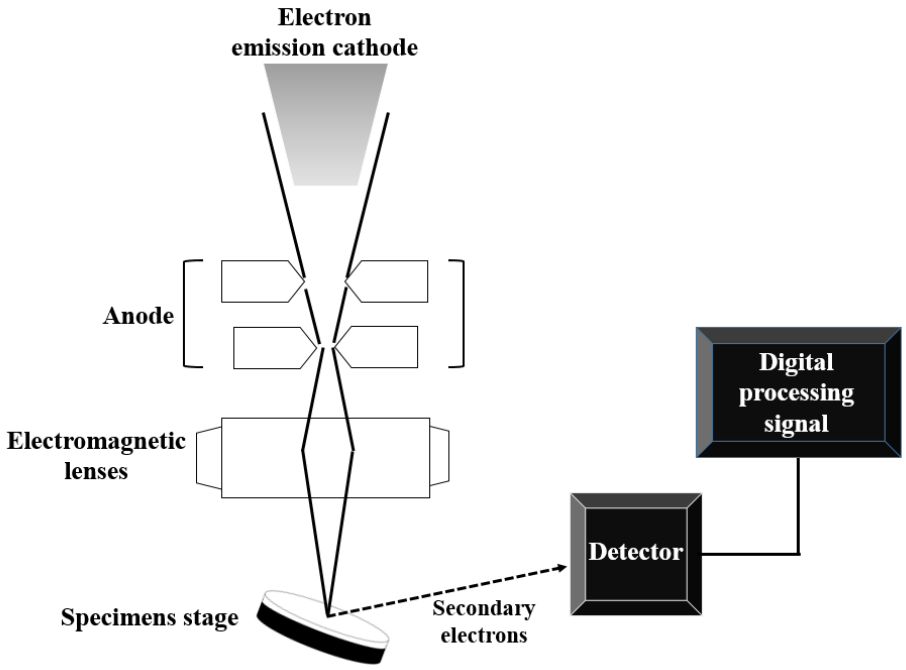

Figure 3.4: Schematic of FESEM showing electron emission gun, anode, electromagnetic lenses, sample, secondary electron detector, digital processing signal.

A field emission source (FES), also called a cold cathode field emitter, does not heat the filament. The FES is a wire of tungsten (W) created into a sharp point with the small tip radius (~100 nm) for concentrated electric field. Electrons are accelerated in

a high electrical field gradient within the high vacuum column these so-called primary electrons are focused and deflected by electronic lenses to produce a narrow scan beam that bombards the object. The acceleration voltage between cathode and anode is commonly in the order of magnitude of 0.5 to 30 kV and the apparatus requires an extreme vacuum (~10^{-6} Pa). The primary electron beam interacts with the atoms at the surface (down to 1 μm depth) of the sample generating low energy secondary electrons, the energy of which is governed by the surface topography [69]. Figure. 3.5 shows a variety of signals at surface and sub-surface of the sample.

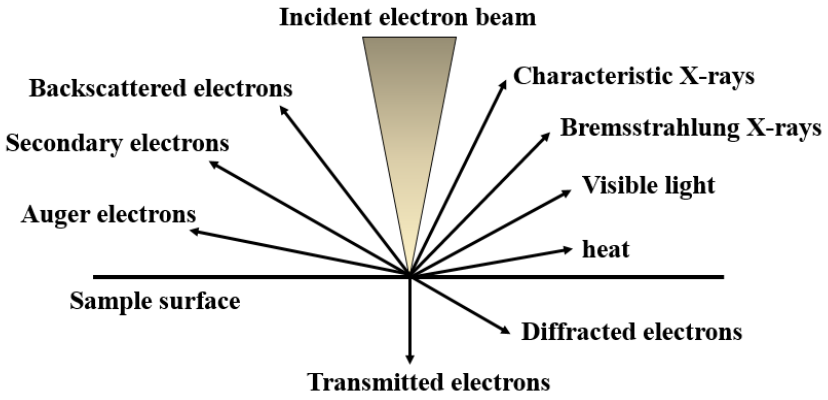

Figure 3.5: Interaction between the incident electron beam and sample surface.

As shown in the Fig. 3.6, the secondary electrons (50-500 Å) occurred near the sample surface approximately 10 nm in depth with the energy about 3-5 eV. By scanning the sample and collecting the secondary electrons, an image of the topography of the surface is constructed. I will use FESEM technique to obtain the surface morphologies and cross section views of undoped and Ag-doped CCTO thin films deposited on silicon and alumina substrates.

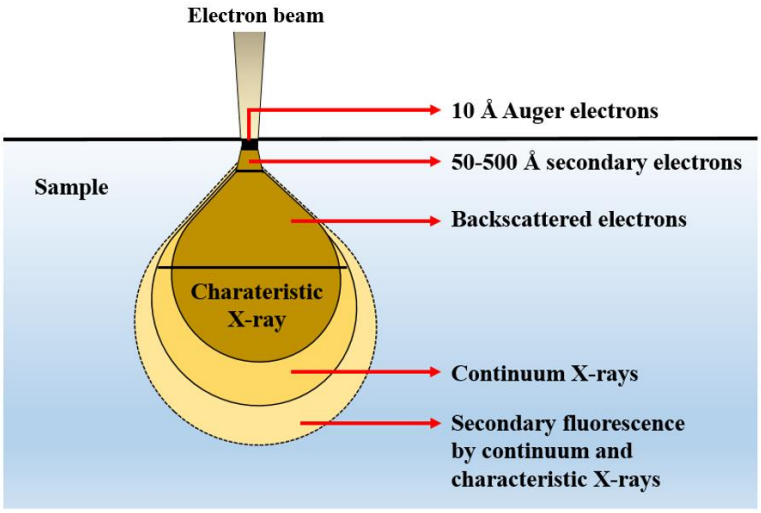

Figure 3.6: A schematic of various possible results of electron hitting a sample.

In addition to secondary electrons imaging, Energy Dispersive X-ray Spectroscopy (EDS or EDX) analysis is used for the elemental analysis or chemical characterization of a sample. The EDX system detects the X-photons emitted by the sample after excitation by the electron beam. The energies of the emitted X-photons that are characteristic of an element's atomic structure to be identified uniquely from one another [70]. EDX technique is useful to determine each element existing in undoped and Ag-doped CCTO thin films deposited on silicon substrates, especially to verify the doping concentrations in the films.

3.3 Raman Spectroscopy

Raman spectroscopy is a form of molecular spectroscopy that involves the scattering of electromagnetic radiation by atoms or molecules. The Raman scattered light occurs at wavelengths that are shifted from the incident light by the energies of molecular vibrations [71]. It can be derived by considering the vibration mode structure of a simple diatomic molecule as shown in Fig. 3.7. Hook's law is used in approximation.

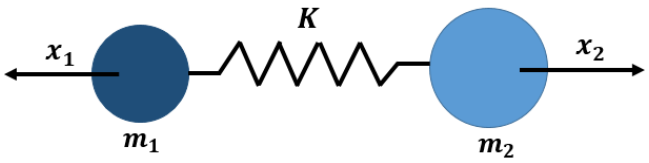

Figure 3.7: A simple diatomic molecule.

It is considered in Hook's law as shown in the Equation (3.5)-(3.7).

$$F = -Kx \tag{3.5}$$

$$\frac{m_1 m_2}{m_1+m_2}\left(\frac{d^2x_1}{dt^2}+\frac{d^2x_2}{dt^2}\right) = -K(x_1+x_2) \tag{3.6}$$

$$\mu\frac{d^2q}{dt^2} = -Kq \tag{3.7}$$

where μ is reduced mass,

q is the molecular displacement.

In the classical derivation of the Raman effect, internal vibrational motion with eigen frequency ν_m is shown in the Equation (3.8).

$$q = q_0 \cos(2\pi\nu_m \cdot t) \tag{3.8}$$

It is govern by the polarizability of electron cloud around the molecule. When the electric field of the incident light interacts with the molecules, it interferes with the molecule's vibration, inducing a dipole moment. Induced dipole moment (P) is described with electric field (E) due to electromagnetic wave with frequency v_0 as shown in the Equation (3.9).

$$P = \alpha E = \alpha E_0 \cos 2\pi v_0 \cdot t \tag{3.9}$$

For a small amplitude of vibration, the polarizability (α) is a linear function of q,

$$\alpha = \alpha_0 + (\frac{\partial \alpha}{\partial q})_{q=0} \cdot q + \cdots \tag{3.10}$$

Then, we can form

$$P = \alpha_0 E_0 \cos(2\pi v_0 \cdot t) + (\frac{\partial \alpha}{\partial q})_{q=0} \cdot q_0 \cos(2\pi v_m \cdot t) \cdot E_0 \cos(2\pi v_0 \cdot t)$$

$$P = \alpha_0 E_0 \cos(2\pi v_0 \cdot t) + \frac{1}{2}(\frac{\partial \alpha}{\partial q})_{q=0} q_0 E_0 \begin{bmatrix} \cos(2\pi\{v_0 - v_m\} \cdot t) \\ + \cos(2\pi\{v_0 + v_m\} \cdot t) \end{bmatrix} \tag{3.11}$$

By applying the linear approximation, it can be seen that the first term represents Rayleigh scattering; the frequency is presented by v_0, which means there has been no change in the frequency. This is also known as elastic scattering. The second term of linear approximation produces Stokes and anti-Stokes scattering, and these are represented by a change in the frequency, with the frequency variables denoted by negative v_m and positive v_m [71]. Raman from the particle point of view can be visualized by a quantum energy diagram as shown in Fig. 3.8.

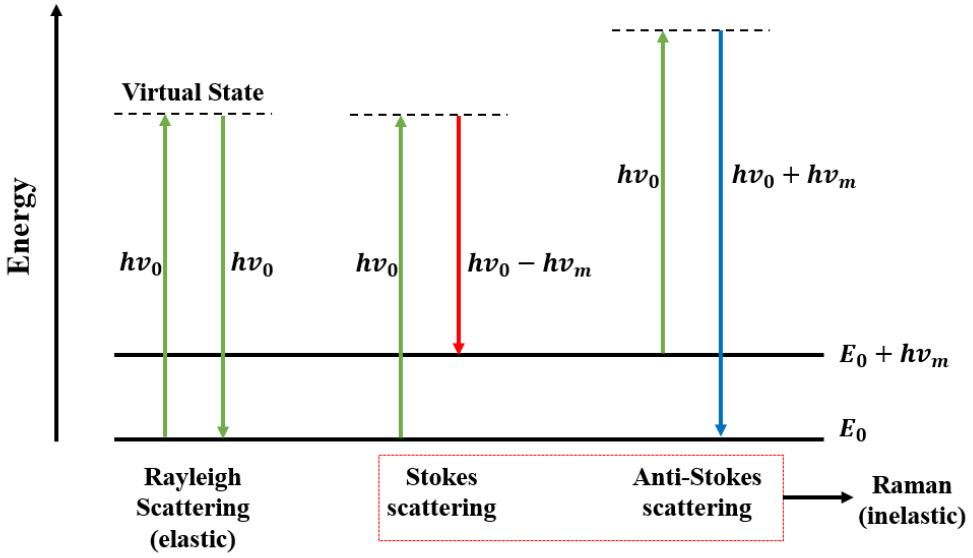

Figure 3.8: Energy Scheme for Photon Scattering.

A Raman spectrum is a plot of the intensity of Raman scattered radiation as a function of its frequency difference from the incident radiation (usually in units of wavenumbers, cm^{-1}). This difference is called the Raman shift [71].

3.4 X-ray Photoelectron Spectroscopy (XPS)

X-ray photoelectron spectroscopy (XPS) is a form of electron spectroscopy in which a sample is irradiated with a beam of monochromatic x-rays and the energies of the resulting photoelectron are measured. XPS is widely used surface analysis technique. It is a very helpful technique in obtaining information about oxidation state and atomic composition based on analyzed compounds. In XPS, the sample is placed in a high vacuum environment under the best vacuum conditions achievable (below 10^{-8} mbar) and exposed to a low-energy (~1.5 keV) monochromatic x-ray source in order to provoke the photoelectric effect described by Albert Einstein [72]. Then, the incident

X-rays cause the ejection of core-level electrons from sample atoms. The energy spectrum of the emitted photoelectrons is determined by means of a high-resolution electron spectrometer. After that detector can detect the kinetic energy and which provides the information to determine the kind of elements present in the sample. Schematic representation of the X-ray photoelectron process is shown in the Fig. 3.9.

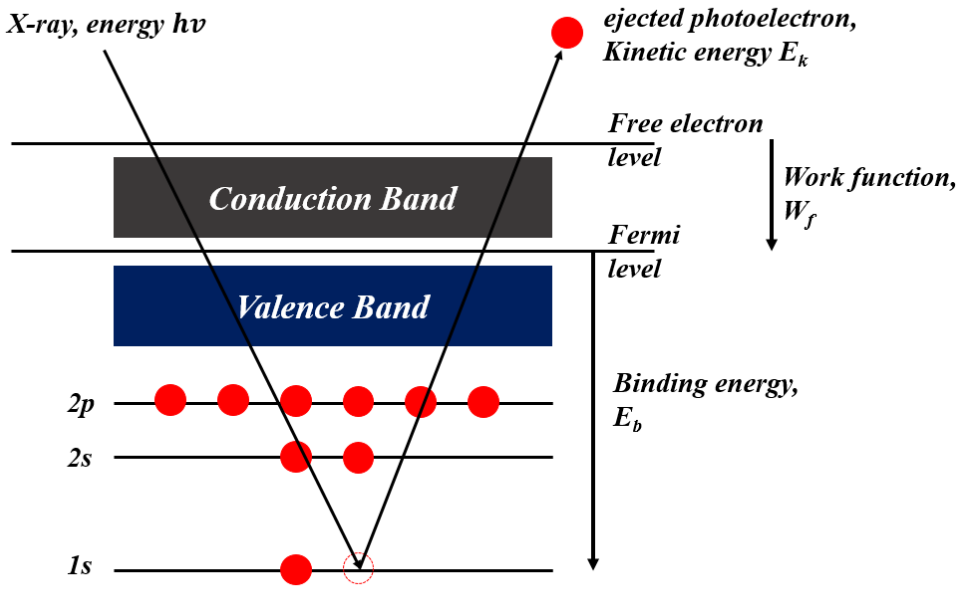

Figure 3.9: Schematic representation of the X-ray photoelectron process.

The atoms in the sample are ionized and the electrons with binding energies (E_b) absorb photons with energy $h\nu$ and escape from the sample body with kinetic energy E_k. It is determined by the following Equation (3.12).

$$E_k = h\nu - E_b - W_f \qquad (3.12)$$

where W_f is the material work function and it can be defined in the Equation (3.13),

$$W_f = E_{vacuum} - E_f \qquad (3.13)$$

The X-ray photoelectron spectroscopy detects the electron energies. It can be identified the elements and oxidation states of the atoms in a sample. The XPS spectrum shows a number of emitted electrons against their kinetic energy. In general, the data is plotted with the intensity of X-ray produced and the binding of the electron that got kicked out of the shell. We will attempt to use XPS technique to confirm the existence of Ag doping in the CCTO films deposited on silicon substrates

CHAPTER IV
EXPERIMENTAL DETAILS

4.1 CCTO preparation

In this chapter, the experimental details are divided into three main parts. In the beginning of the chapter, we will focus on CCTO films prepare by a solution sol-gel method (SSG) that use glacial acetic as dissolution. Undoped CCTO and Ag-doped CCTO thin films prepared using two silver compounds were cast on alumina substrates for gas sensor fabrication. At the end of this chapter, the details of coplanar gas sensor fabrication, sensor response measurements are explained.

4.1.1 Synthesis of CCTO and Ag-doped CCTO precursors

The procedure for CCTO film preparation is summarized as shown in Fig. 4.1. The precursors are calcium acetate hydrate ($Ca(C_2H_3O_2)_2 \cdot xH_2O$, Sigma, 99%), copper (II) acetate monohydrate ($Cu(II)(C_2H_3O_2) \cdot H_2O$, Fluka, 99%), titanium (IV) isopropoxide ($Ti(OCH(CH_3)_2)_4$, Sigma, 97%). The composition of calcium: copper: titanium: oxygen: without doping will be controlled to 1:3:4:12 which is the atomic ratio of pure CCTO. The CCTO thin films devices will be fabricated for gas sensing applications including the sensor response and the selectivity. The different Ag compounds used in this study are silver acetate ($AgCH_3CO_2$, MERCK, 98.5%) and silver perchlorate ($AgClO_4$, ALORICH, 97%). Each compound was added into the separate precursor solution and also the concentration of Ag was varied upon on each

own capability in dissolving in acetic acid. The specimens of $CaCu_3Ti_4O_{12}$ modified with the different Ag compounds ($AgCH_3CO_2$: Ag doping = 0, 0.3, 0.6, and 0.9 wt% and $AgClO_4$: Ag doping = 0, 1, 3, 5, 7, and 9 wt%) were prepared by adding into the sol precursor solutions, which would be used to deposit sensing films.

In the first step, Ag compounds were dissolved into glacial acetic acid (25.0 ml) on hot plate at 120 °C. Then, 0.855g of calcium acetate dehydrate and 2.943 g of copper (II) acetate dehydrate were added into the sol precursor solutions and maintained under magnetic stirring for 24 h at room temperature. After that 6.13g of titanium (IV) isopropoxide, 3 ml of ethylene glycol and 3 ml of formamide were added into the mixture. The solution was sealed and continued heating at 120 °C for 4-5 h. Then, the solution was poured into 50 ml lab bottle at room temperature for 24 h. After that, the films were spun by using spin coater. I will explain in the next section.

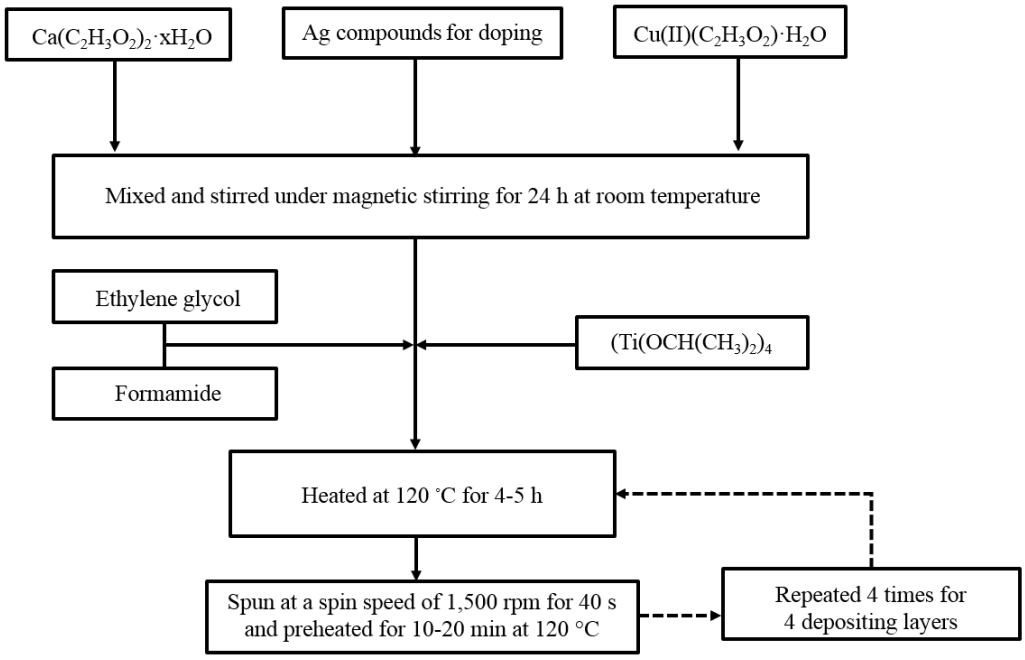

Figure 4.1: The flow chart of the process of sol-gel preparations for the CCTO thin films with different Ag compounds.

4.1.2 Ag-doping preparation

In this thesis, the Ag-doped CCTO films with different silver compounds were prepared by a sol-gel technique. Silver compounds such as silver acetate ($AgCH_3CO_2$) and silver perchlorate (Ag) were used as the dopants in the precursor. To prepare silver (Ag) doped films, the solubility of silver compounds in acetic acid was considered. Table 4.1 shows the Ag-doping concentrations that be used silver acetate in the precursor. It can be seen that 0.9 wt% of silver acetate can be added in acetic acid. It may be expected that silver acetate can be dissolved in acetic acid more than 0.9 wt% of Ag doping concentration. However, silver acetate is saturated with acetic acid when the Ag doping concentration is beyond 1 wt%.

Table 4.1: Ag-doping concentrations and weights of $AgCH_3CO_2$ in acetic acid 25 g.

Ag-doping concentrations (wt%)	**Weights of $AgCH_3CO_2$ in acetic acid 25 g**
0.3	0.01496 g
0.6	0.02992 g
0.9	0.04488 g

In addition, the higher Ag-doping concentrations were expected in this thesis. It may be efficiency in gas-sensing properties. Therefore, I also selected the second silver compound for adding in the precursors. Silver perchlorate was chosen for the best candidate based on the good solubility in acetic acid. Table 4.2 shows the Ag doping concentrations that be used silver perchlorate in the precursor. However, the gas sensing results including other characterizations of the films prepared using two different silver compounds were described in the Chapter 5.

Table 4.2: Ag-doping concentrations and weights of $AgClO_4$ in acetic acid 25 g.

Ag-doping concentrations (wt%)	Weights of $AgClO_4$ in acetic acid 25 g
1	0.0637
3	0.1912
5	0.3187
7	0.4461
9	0.5736

4.1.3 Substrate preparation and conditions for film deposition

Both undoped CCTO and Ag-doped CCTO thin films sensors were fabricated for gas sensing applications including the sensor response and the selectivity. Four layers of depositing films were grown on substrates. Silicon and alumina are used as substrates. Silicon substrates were cut into small pieces of area approximately 1.0x1.0 cm^2. Alumina substrates were cut into small pieces of area approximately 2.5x2.5 cm^2 for the purpose of making gas sensor arrays.

This section, I will focus on substrate cleaning because of an important part for growing films with good quality. All substrates were cleaned by chemical process in order to remove the impurities such as some particles and dust that might be left from the cutting process before the spin coating process. In each cycle, the substrates were cleaned by acetone and isopropanol (IPA) for 15 min repeating two times in ultrasonic bath. Then, they were heated approximately 80 °C for liquid evaporation before using spin coating technique. Furthermore, I will focus on substrate information which are used for coating CCTO films. Silicon wafer (Si) with (100) orientation has a cubic

structure with a lattice spacing of 5.43 Å and a thermal expansion coefficient of $4.05x10^{-6}$ K^{-1}. Table 4.3 shows some physical properties of Si single crystal substrate.

Table 4.3: Silicon Single Crystal Substrate Properties.

Physical properties of Si (100) substrates	
Crystallographic structure	Cubic phase a=b=c=5.43 Å
Twinning structure	Twin free
Color	Shiny gray (Polished side)
Density	2.33 g/cm^3
Melting point	1420 °C
Thermal expansion	$4.05x10^{-6}$ K^{-1}
Dielectric constant	~11.9 at 300 K

Alumina (Al_2O_3) has a rhombohedral structure. Polycrystalline alumina is used in this work for gas sensing fabrication with the thermal expansion coefficient of $8.2x10^{-6}$ K^{-1}. Table 4.4 shows the summary of some physical properties for alumina substrate.

Table 4.4: Al_2O_3 Substrate Properties.

Physical properties of Al_2O_3 substrates	
Crystallographic structure	Rhombohedral phase lattice constant a=b=4.759 Å and c=12.993 Å
Twinning structure	Twin free
Color	White
Density	3.85 g/cm^3
Melting point	2052 °C
Thermal expansion	~$8.18x10^{-6}$ K^{-1}
Dielectric constant	~9.8 at 300 K

4.1.4 Spin coating process

Undoped and Ag-doped CCTO thin films were spun on both silicon and alumina substrates by spin coating technique at room temperature. The prepared precursors were spun on both substrates at a spin speed of 1,500 rpm for 40 s. Then, they were preheated for 10-20 minutes at 120 °C in order to dry the gel and remove remaining organic compounds before annealing under a fixed temperature and fixed time in the air atmosphere. Spin coating and heating was repeated to 800 °C for one hour in air and then cooled to room temperature.

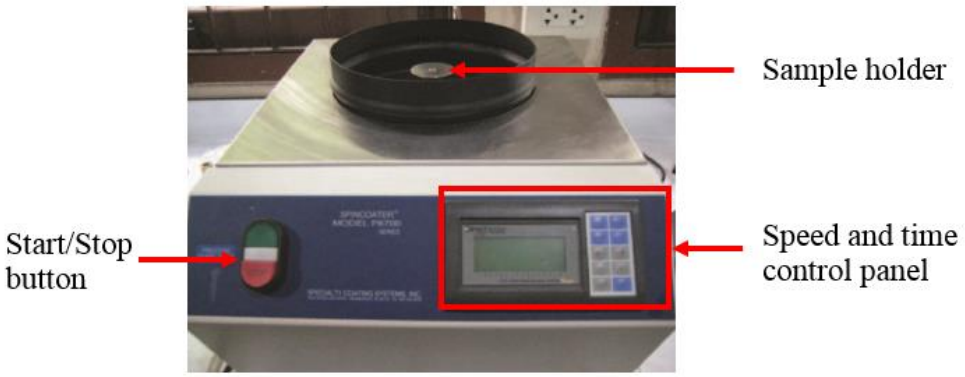

Figure 4.2: The spin coater (model P6700 series).

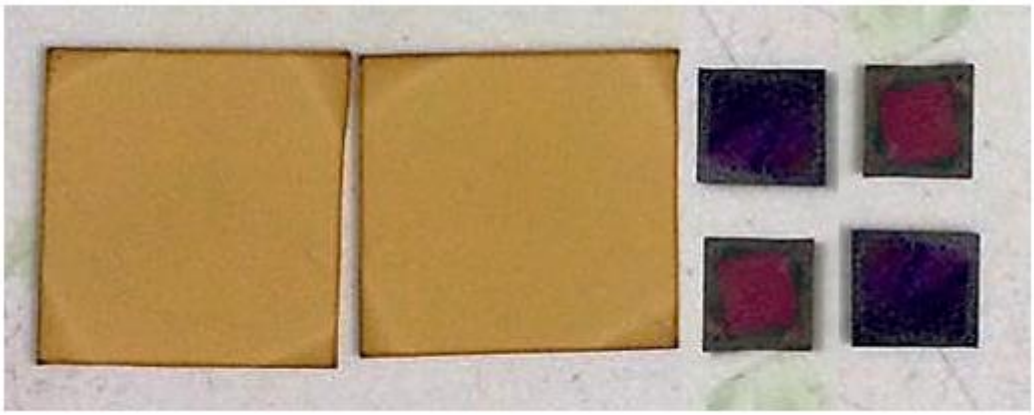

Figure 4.3: Ag doped CCTO films on alumina and silicon substrates.

The CCTO films were structurally characterized by X-ray diffraction (XRD), Field emission scanning electron microscopy (FESEM), energy dispersive X-ray spectroscopy (EDX), Raman spectroscopy and X-ray photo electron spectroscopy. The obtained films on alumina and silicon substrates were confirmed their structures by XRD technique at Scientific and Technological Research Equipment Centre Chulalongkorn University (STREC). The X-ray measurement was collected by using CuK-α_1 (λ = 1.5406 Å) radiation with 40 kV and 40 mA in the 2θ range of 20° to 80° with scan step about 0.02°. And information of film surface morphology on silicon and alumina substrates were obtained from FESEM (SU-8000, Hitachi) at Thai Microelectronics Center (TMEC). The elemental analysis of Ag-doped films on alumina substrates was achieved by performing EDX measurements on EDAX, AMETEK at National Electronics and Computer Technology Center (NECTEC). EDX operated at 10 kV were used for the elemental analysis of films. The oxidation state of the atoms in the Ag-doped CCTO thin films was indicated by XPS, AXIS Ultra DLD at Thailand Center of Excellent in Physics (ThEP center) and the Petroleum and Petrochemical College, Chulalongkorn University. Raman spectroscopy (NT-MDT, NTEGRA) with a 633 nm wavelength laser source was used to gain further insight into the composition and the structure of the Ag-doped CCTO films.

4.2 Fabrication of gas sensor

For gas sensor application, alumina substrates utilize for Ag-doped CCTO thin film preparation because they are cheap and easy to purchase from many companies. Alumina substrates used in this thesis are made from alumina powders that were compact to be dense substrates with the thickness of 0.4 mm. As known alumina

substrates are good insulator and good thermal conductivity, they normally are used to fabricate as substrate for gas sensor. Due to the roughness of alumina substrates, four-layered Ag-doped CCTO deposition was applied to fabricate the gas-sensing devices for application based on their gas-sensing properties. Then, CCTO thin films grown with different growth conditions on alumina substrates were sputtered with Au/Cr electrode as coplanar patterns for detection the quantity of gases. The photolithography process using a positive photoresist and electrode deposition were used as shown in Fig. 4.4.

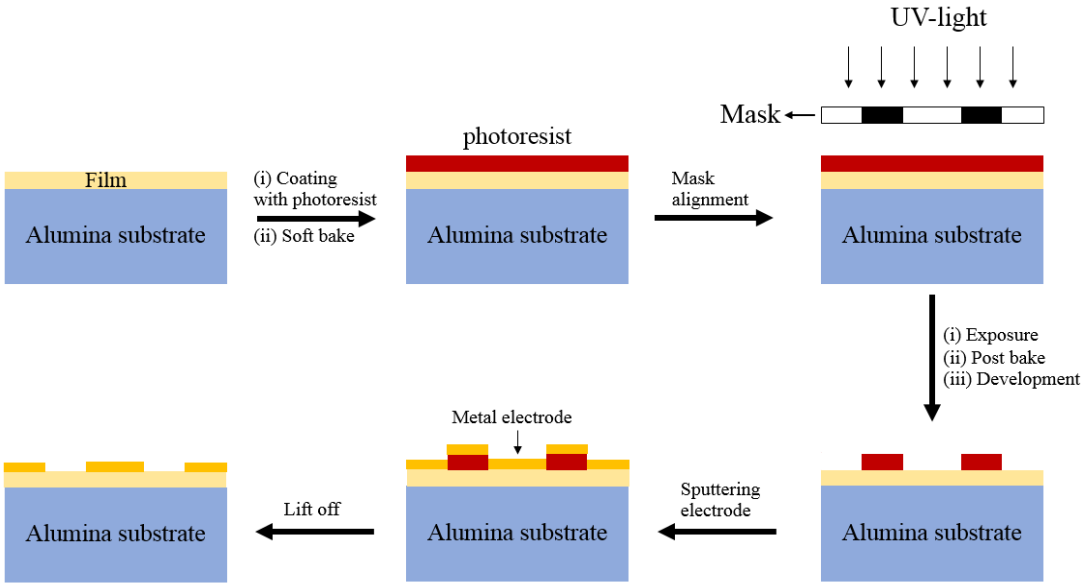

Figure 4.4: Photolithography process of patterning metal electrodes using a positive photoresist.

4.2.1 Photolithography process

Photolithography process is one of the most important technology in the production of advanced integrated circuits. Undoped and Ag-doped CCTO thin films

cast on 0.5 nm thick alumina substrates followed by patterning coplanar interdigitated by photo-lithography. The process follows the following basic steps:

The first step, the wafer is spin coated with resist to form a uniform ~1 μm thin film of resist on the surface as shown in Fig. 4.5. It was spun with high-speed at 3000 rpm for 90 seconds and then heated at 115 °C for 60 seconds on hot plate.

Figure 4.5: Spin coating the substrate with the photoresist.

The second step, a mask made with a positive photoresist (AZ 4620, Microchem Inc.) was applied by dropping the photoresist onto the CCTO surface until it was cover the whole surface as shown in Fig. 4.6. The wafer is exposed with ultraviolet light through a mask which contains the desired pattern as shown in Fig. 4.7.

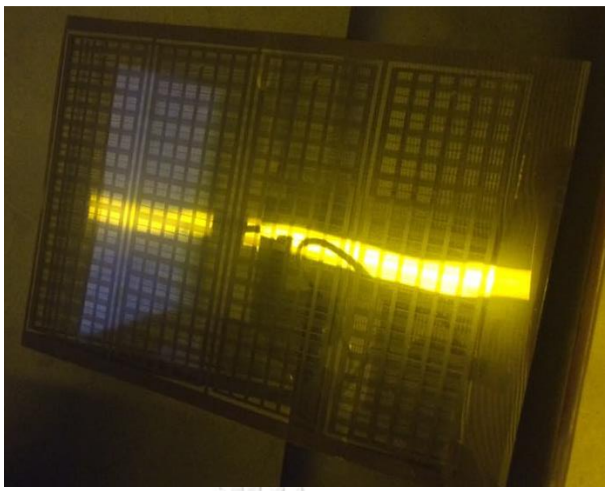

Figure 4.6: The interdigitated shadow mask.

Figure 4.7: UV light through the mask onto the coated wafer.

The third step, the wafer was gently shaken in developer to aid the dissolution of the exposed photoresist and the irradiated area is washed away in the case of positive resist and then the films with the pattern on seen in the Fig. 4.8 will be deposited

electrodes to fabricate the sensors. I will explain the electrode deposition in the next section.

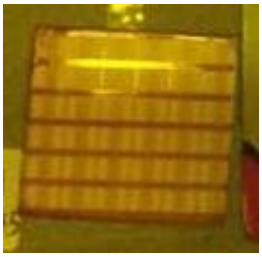

Figure 4.8: The pattern on surface film after developing.

4.2.2 Electrode deposition

From Fig. 4.9, undoped CCTO and Ag-doped CCTO were cast on 0.4 mm thick alumina substrates followed by patterning coplanar interdigitated electrodes. The electrode and photoresist under exposure to a UV-light were lift-off with acetone in an ultrasound bath at room temperature. The gas sensors were baked at 400 °C in air for removing any remnants of organic compounds from surface of films. Electrodes were made by sputtering chromium (~50 nm) and then gold (~300 nm) layers on the substrates with photoresist patterns , having the interdigit spacing of 100 μm [73]. An array of sensors was cut using a dicing saw into several individual sensors for gas testing in a flow chamber with the area of 4.2mm x 5mm as shown in Fig. 4.10.

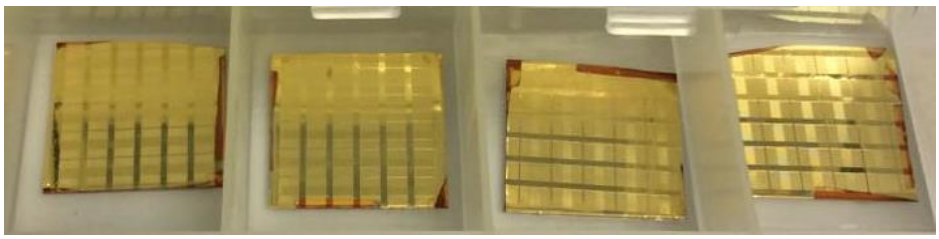

Figure 4.9: Electrodes on surface of films by sputtering.

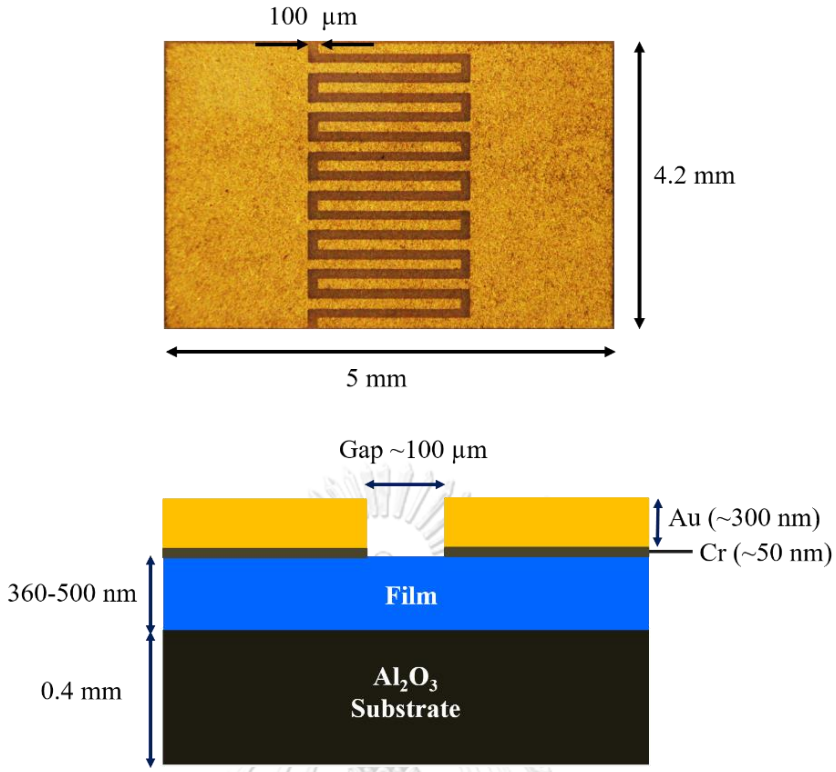

Figure 4.10: Photograph and schematic drawing of a gas-sensing device.

4.3 Gas sensing properties measurement

The sensors were mounted on a heating stage and connected to a resistance meter. A stainless steel cylindrical chamber 12 cm in diameter and 15 cm in height provided with a conical gas distributor with a diameter of 8 cm and a height of 6 cm to uniformly spread the gas onto all sensors. A standard flow through technique was employed to test the gas sensing properties of the sensors. The desired concentrations of target gases were obtained by mixing standard gas with dry synthetic air at a constant total flux of 2L/min. The standard H_2S gas sources were balanced in synthetic air with the calibrated concentrations of 100 ppm. All the measurements were conducted in a temperature-stabilized sealed chamber at 20 °C. An external NiCr heater driven by a

regulated DC power supply was used to set different operating temperatures between 150 and 350 °C. The schematic of gas sensing measurement set up is demonstrated in Fig. 4.11.

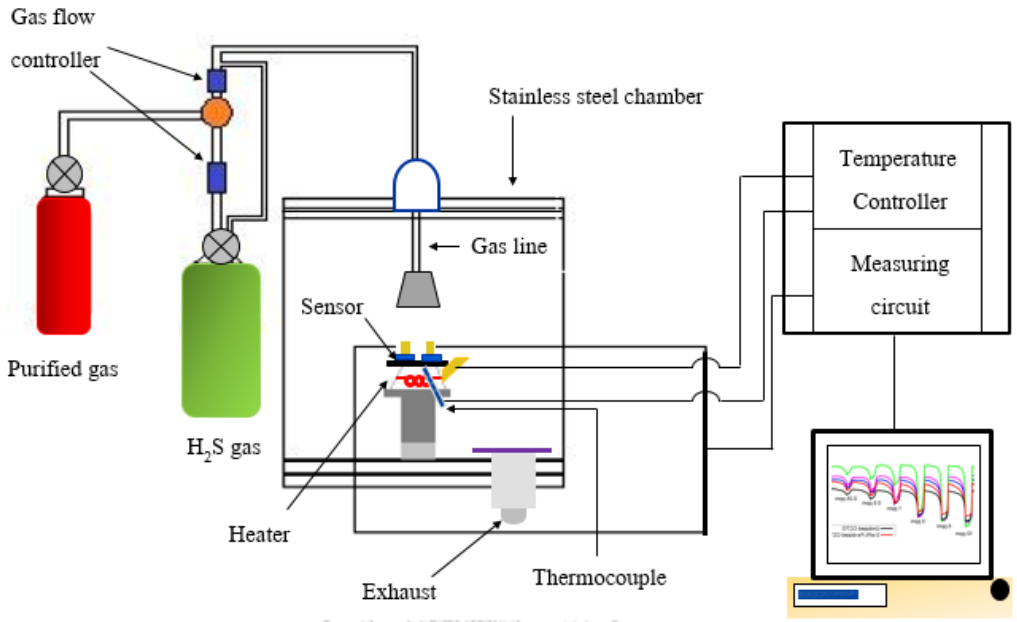

Figure 4.11: Schematic set up for gas sensing measurement.

In this work, both undoped CCTO and Ag-doped CCTO thin films were tested for selective sensing to H_2S (hydrogen sulfide), relative to ammonia (NH_3), hydrogen (H_2), nitrogen dioxide (NO_2) and ethanol vapor (C_2H_5OH). The resistance of the sensors was monitored under gas flow at temperatures between 150-350 °C. The gas sensor response, R is defined as follows:

$$R = \frac{R_a}{R_g} \quad \text{for reducing gases} \qquad (4.1)$$

or

$$R = \frac{R_g}{R_a} \quad \text{for oxidizing gases} \qquad (4.2)$$

where R_a is the electrical resistance of gas sensors in pure dry air and R_g is the sensor electrical resistance in the presence of the target gases [74].

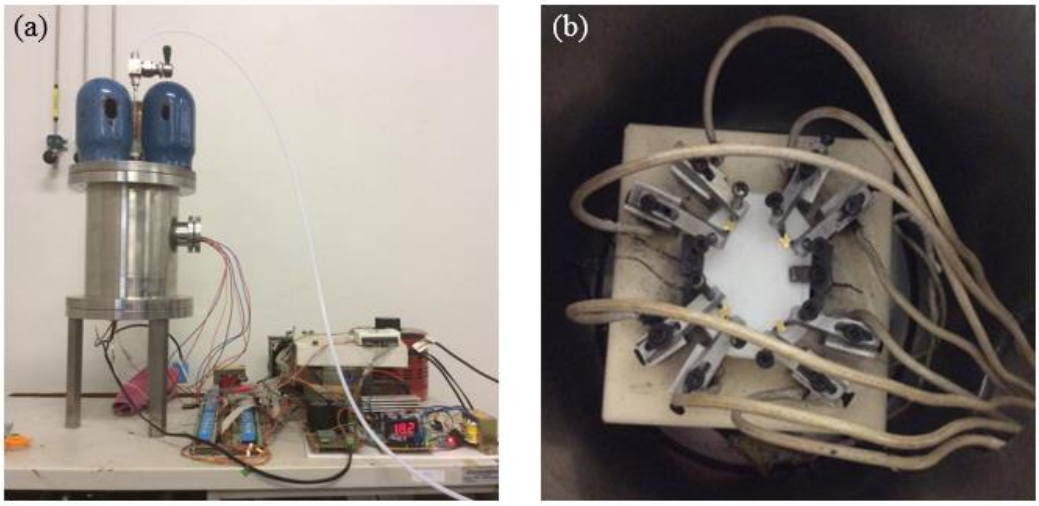

Figure 4.12: (a) The gas chamber for gas sensing measurements with temperature controller and (b) the probes are contacted the sensing devices in the chamber.

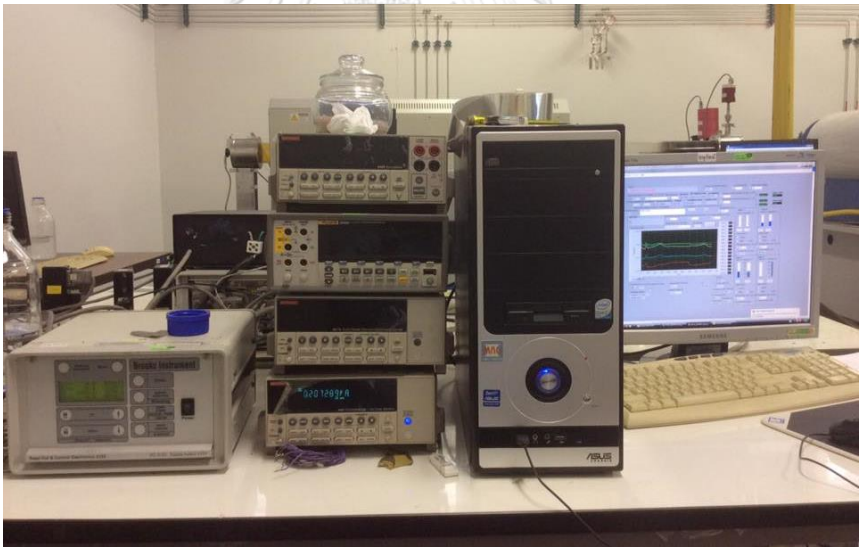

Figure 4.13: A set of gas sensing processor.

The probes are contacted the sensing devices in the chamber for gas sensing measurements and operating temperature can be varied by temperature controller as shown in Fig. 4.12. A set of gas sensing processor is used to control the gas-sensing measurement.

CHAPTER V
RESULTS AND DISCUSSION

In this chapter, the results and discussion from the experiments are divided into two sections. For the first section, we will show the results and discussion for silver acetate as the dopants in CCTO films. The crystal structure and surface morphology of the undoped and Ag-doped CCTO films grown on Si (100) and alumina substrates are shown in the sub-section 5.1.1. In the sub-section 5.1.2, oxidation state and weight percentage of Ag in CCTO films will be discussed. In the sub-section 5.1.3, the vibration modes of the Ag-doped CCTO films were studied. In the sub-section 5.1.4 and 5.1.5, we will show gas sensing results of various reducing and oxidizing gases and mechanisms for enhanced H_2S gas sensing performance of the Ag-doped CCTO films, respectively. The second section is about the results and discussion for silver acetate as the dopants in CCTO films. We will explain why the results were not as expected. These are illustrated by the EDX spectra and gas-sensing properties of Ag-doped CCTO films.

5.1 Results and discussion for silver acetate as the Ag dopant in CCTO films

5.1.1 The crystal structure and surface morphology of the undoped and Ag-doped CCTO films grown on Si (110) and alumina substrate

The crystal structure of undoped and Ag-doped CCTO films containing Ag concentration of 0.3, 0.6, 0.9 wt% (0.6%, 1.1%, 1.7% by mole, respectively) were studied using X-ray diffraction (XRD) technique. Figure 5.1 and 5.2 show typical θ-2θ X-ray diffraction patterns of CCTO thin films on the silicon substrates and the alumina substrates, respectively. The characteristic of CCTO peaks in Fig. 5.1 and 5.2 are at 2θ = 34.4°, 49.4°, 61.8° and 77.4° corresponding to the (220), (400), (422) and (600) planes, respectively. The diffraction patterns of the CCTO films closely agree with the standard CCTO reflections (JCPDS 21-0140) which are all consistent with the cubic perovskite CCTO structure. The strong (h 0 0) peaks from the silicon substrates also can be seen in Fig. 5.1. As seen in Fig. 5.2, the alumina substrate carrying the interdigitated gold electrodes gives rise the dominant diffraction peaks of Al_2O_3 phase and Au peaks. The crystal structure of CCTO and Ag-doped CCTO films on alumina substrates also agrees with the CCTO structure regardless of the two types of substrates used in this work. No shifts are observed in the peaks upon doping, meaning that the CCTO is not distorted to a significant extent at the doping levels of Ag used in this work.

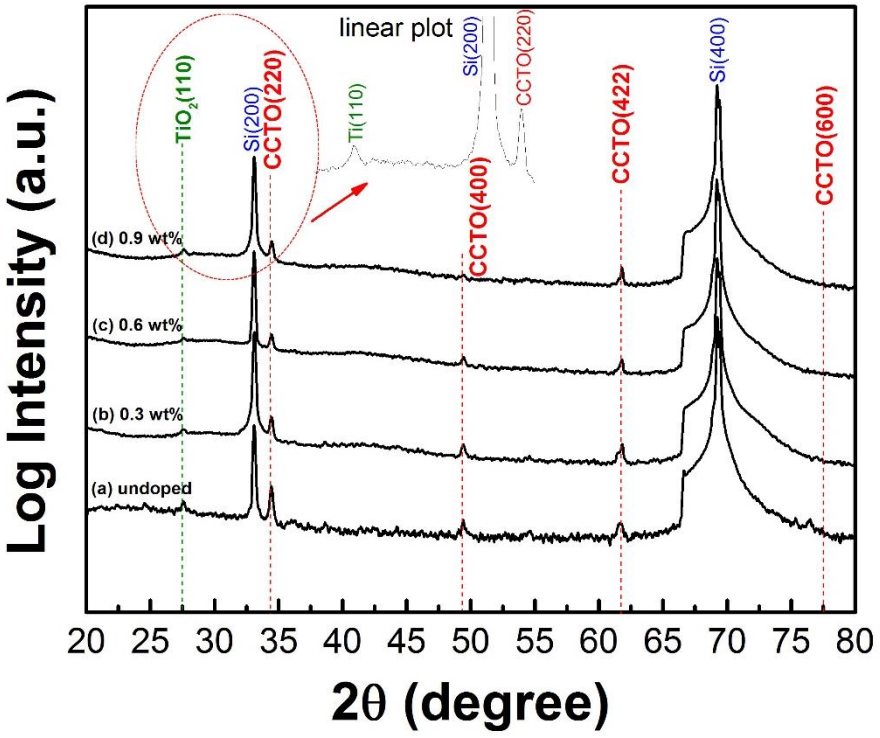

Figure 5.1: X-ray diffraction patterns of Ag-doped CCTO films on silicon substrates.

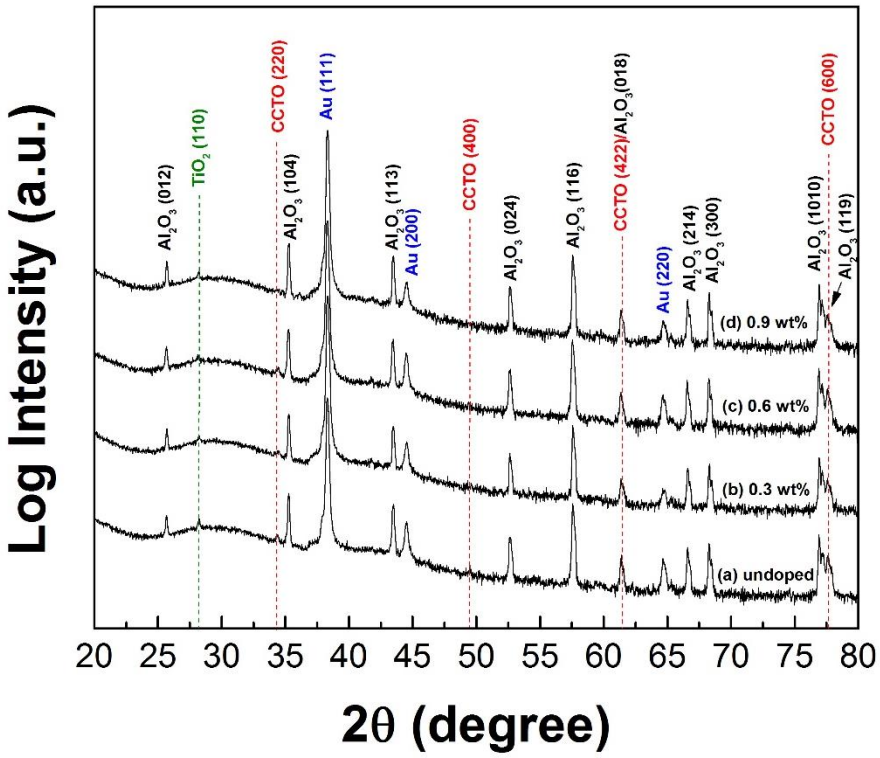

Figure 5.2: X-ray diffraction patterns of Ag-doped CCTO films on alumina substrates.

The calculated lattice constant of our CCTO thin films is 7.359±0.003 Å which is slightly lower than that for bulk CCTO (7.391 Å). The intensity and the FWHM of CCTO peaks decreased as increasing in Ag concentrations which is consistent with the Ag substitution in the CCTO structure. This confirms the existence of substituting Ag to CCTO sites. The CCTO films are relatively pure and contained only very small amounts of TiO_2 impurities evidenced some weak diffraction signals and there are no signs of any Ag oxides in XRD patterns.

Surface morphology of CCTO films on silicon substrates with different Ag doping concentrations are shown in Fig. 5.3 (a)-(d). With Ag doped CCTO films, grains become smaller and more uniform with the rod shaped morphology depend on Ag doping. The rod shaped morphology is formed from four or more grains with the mean length of ~200-300 nm. Figure 5.4 (a)-(d) show a cross section image of CCTO films with different Ag concentrations on silicon substrates. The film thickness for four-layered deposition is approximately 540 nm for undoped CCTO films and approximately 330-440 for Ag-doped CCTO films. The thickness for Ag-doped CCTO films is smaller than that of undoped films due to having smaller grains and more holes. With these reasons, when the next precursor was dropped on to the previous film surface it tends to cover to holes as well as cover the whole surface. It can be seen that the surface of silicon substrates (see Fig. 5.4) is much smoother than that of alumina substrates (see Fig. 5.6). These results are easy to estimate the thickness for one-layered deposition. It is known that the surface of alumina substrates is quite rough. In order to cover some cracks and holes appeared on the surface of alumina substrates, the same four-layered deposition was applied on alumina substrates to fabricate CCTO thin films devices for application based on their gas-sensing properties.

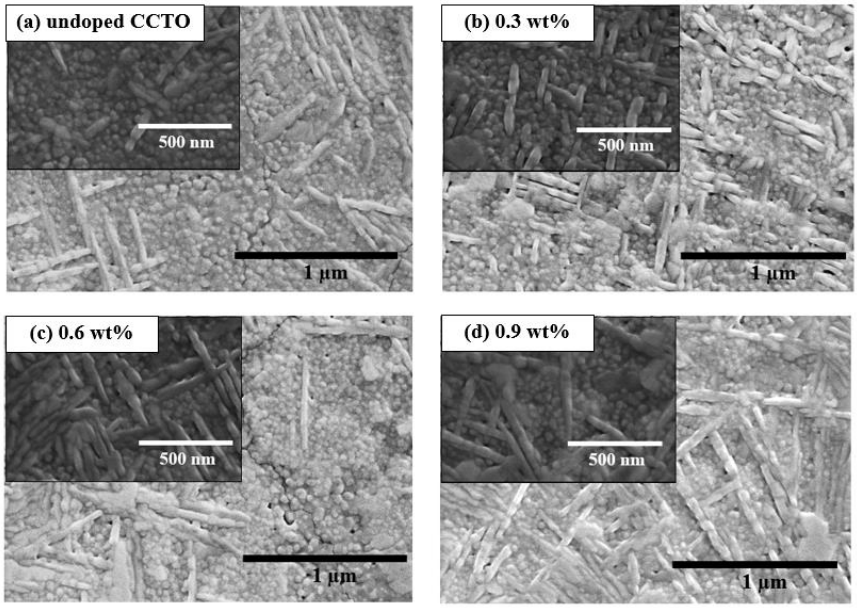

Figure 5.3: FESEM images of CCTO films on silicon substrates annealed at fixed temperature 800 °C (a) undoped, (b) 0.3 wt% Ag, (c) 0.6 wt% Ag, and (d) 0.9 wt% Ag.

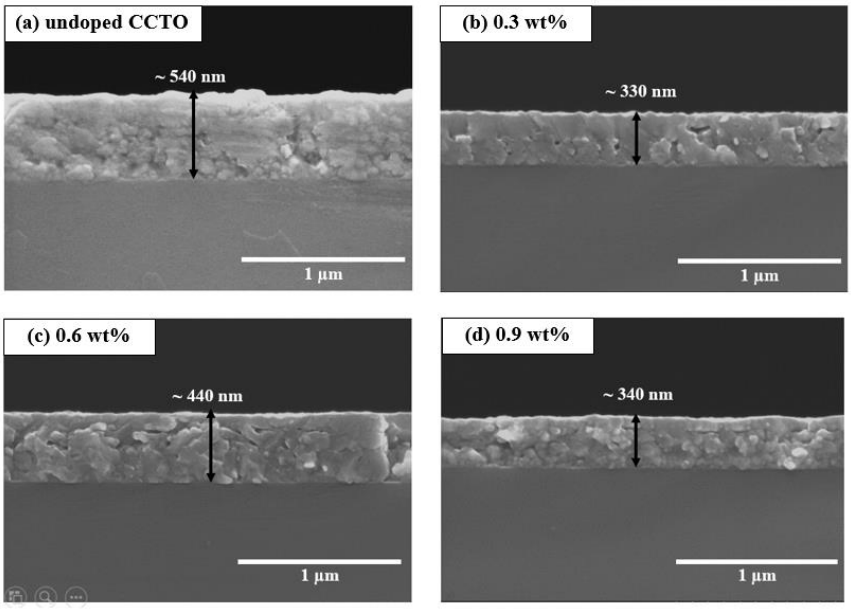

Figure 5.4: Cross section of CCTO films on silicon substrates annealed at fixed temperature 800 °C (a) undoped, (b) 0.3 wt% Ag, (c) 0.6 wt% Ag, and (d) 0.9 wt% Ag.

Surface morphology of CCTO films on alumina substrates with different Ag doping concentrations are shown in Fig. 5.5 (a)-(d). The undoped CCTO film has granular morphology with particle diameters in the 10-25 range. This granular morphology agrees with previously reported CCTO films deposited via chemical sol-gel method [41, 75]. The appearance of the surface in the case of the Ag-doped CCTO films is in marked difference with the pure CCTO films. There appear to be three main particle distributions on the surface, a granular from similar to that in pure CCTO, a clustered form and elongated crystal. In addition, it can be observed that the granular size becomes smaller and more uniform as the silver doping level increases. At the same time, rod-like CCTO crystals appear to become increasingly important. The clustered particles do not appear to have a clear trend being more or less similar among all the Ag-doping levels studied. The rod shaped particles have a mean length of ~200-300 nm and appear to have a highly correlated orientation either in one direction or perpendicular to that direction. The origin of these elongated particles is not clear at this time. The fact that the X-ray diffraction experiments did not reveal additional phases as well as the preferential orientation suggest that these rod-like particles are CCTO crystals with highly anisotropic growth. Shape inducing effects involving nanorods in the presence of silver ions are recurrent phenomenon. The surface morphology Ag-nanoparticles/TiO_2 composite thin films also exhibit some spherical/rod-like and partially agglomerated particles on the surface of the films [76] and gold nanorods are commonly synthesized by introducing Ag as a catalyst for the nanorod growth [77]. A likely explanation is that Ag tends to adsorb predominantly on particular faces of the growing crystal where it slows down their growth while other planes continue to grow and dominate the final particle shape [77].

Figure 5.6 (a)-(d) show a typical cross section image of Ag-doped CCTO thin films on alumina substrates. Due to the roughness of alumina substrates, it can be seen that the film thickness for four-layered deposition is considerably varying between 220 to 500nm. The cross sectional view of the films reveals that some properties and voids exist in the films

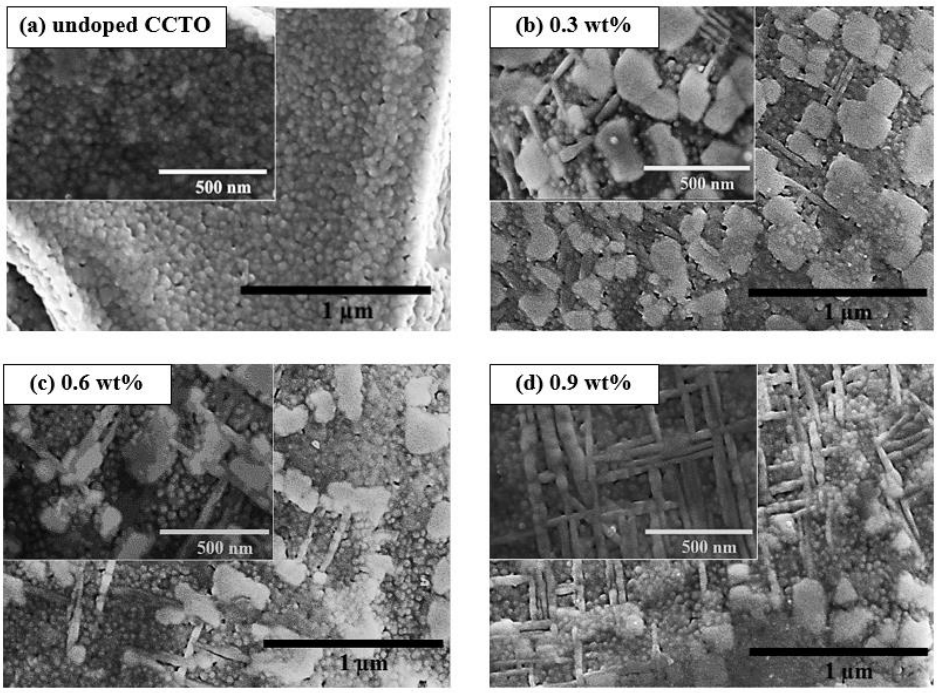

Figure 5.5: FESEM images of CCTO films on alumina substrates annealed at fixed temperature 800 °C (a) undoped, (b) 0.3 wt% Ag, (c) 0.6 wt% Ag, and (d) 0.9 wt% Ag.

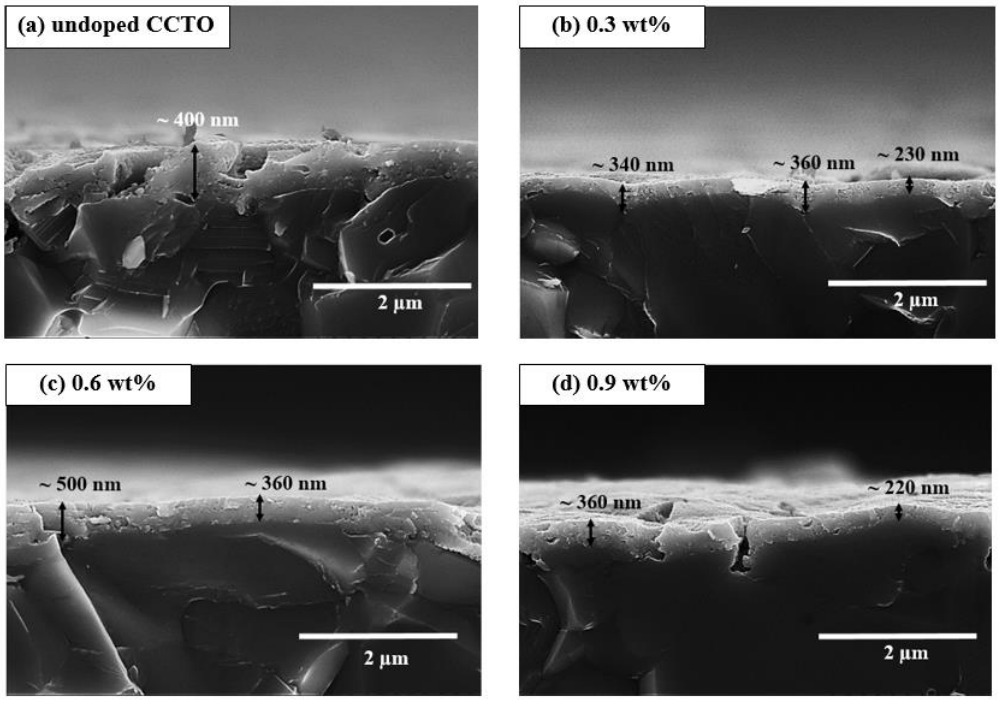

Figure 5.6: Cross section of CCTO films on alumina substrates annealed at fixed temperature 800 °C (a) undoped, (b) 0.3 wt% Ag, (c) 0.6 wt% Ag, and (d) 0.9 wt% Ag

5.1.2 Oxidation state and weight percentage of Ag in CCTO films

XPS measurement can be confirmed the oxidation states of the elements in the Ag-doped CCTO films. Figure 5.7 shows a typical XPS survey spectrum for the Ag-doped CCTO film. The expected elemental peaks including Ca 2p, Cu 2p, Ti 2p and O 1s were examined with high-resolution scans, respectively. Signals due to silver were not observed in the survey spectrum of the doped films when the films were prepared from the small doping concentration. These results cannot confirm that the silver dopants are added in the films.

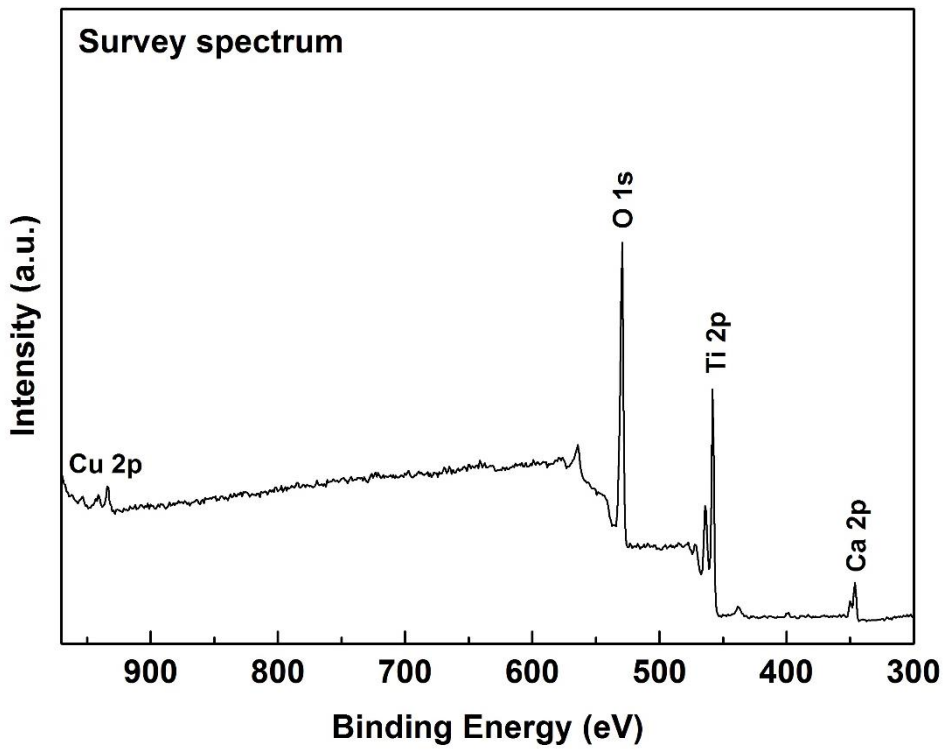

Figure 5.7: X-ray photoelectron spectra of survey spectrum for the Ag-doped CCTO films.

Figure 5.8 shows the X-ray photoelectron spectra (XPS) of (a) Ca 2p, (b) Cu 2p, (c) Ti 2p and (d) O 1s core levels for Ag-doped CCTO films. The Ca 2p signal (Fig. 5.8(a)) could be related to two dominant Gaussian peaks of Ca $2p_{3/2}$ and Ca $2p_{1/2}$ at

binding energies of 346.6 and 350.0 eV, which might be assign to the typical Ca^{2+} oxidation state with 12 oxygen atoms [41]. The secondary peaks with no 12 oxygen atoms of Ca $2p_{3/2}$ and Ca $2p_{1/2}$ at binding energies of 347.5 and 351.0 eV. The Cu 2p core level spectrum (Fig. 5.8(b)) comprised the spin orbit doublets of Cu $2p_{3/2}$ and Cu $2p_{1/2}$ that can be assigned the main peaks at 933.7 and 953.3 eV and satellite peaks at 941.8 and 962.1 eV. Both Cu $2p_{3/2}$ and Cu $2p_{1/2}$ consist of three components which could be all assigned to Cu^{+}, Cu^{2+} and Cu^{2+} with 6 oxygen atoms [78]. In the case of the core level of Ti 2p (Fig. 5.8(c)), the spin doublets of Ti $2p_{3/2}$ and Ti $2p_{1/2}$ also contained the main peaks at 458.5 and 464.2 eV, respectively, which were shown the typical Ti^{4+} oxidation state of TiO_6 [79, 80]. The O 1s in Fig. 5.8(d) could be decomposed into two main peaks at binding energies of 529.8 and 531.5 eV, which might be related to lattice oxygen (O^{2-}) and the chemisorbed oxygen species on the surface (O_2^-), respectively [81].

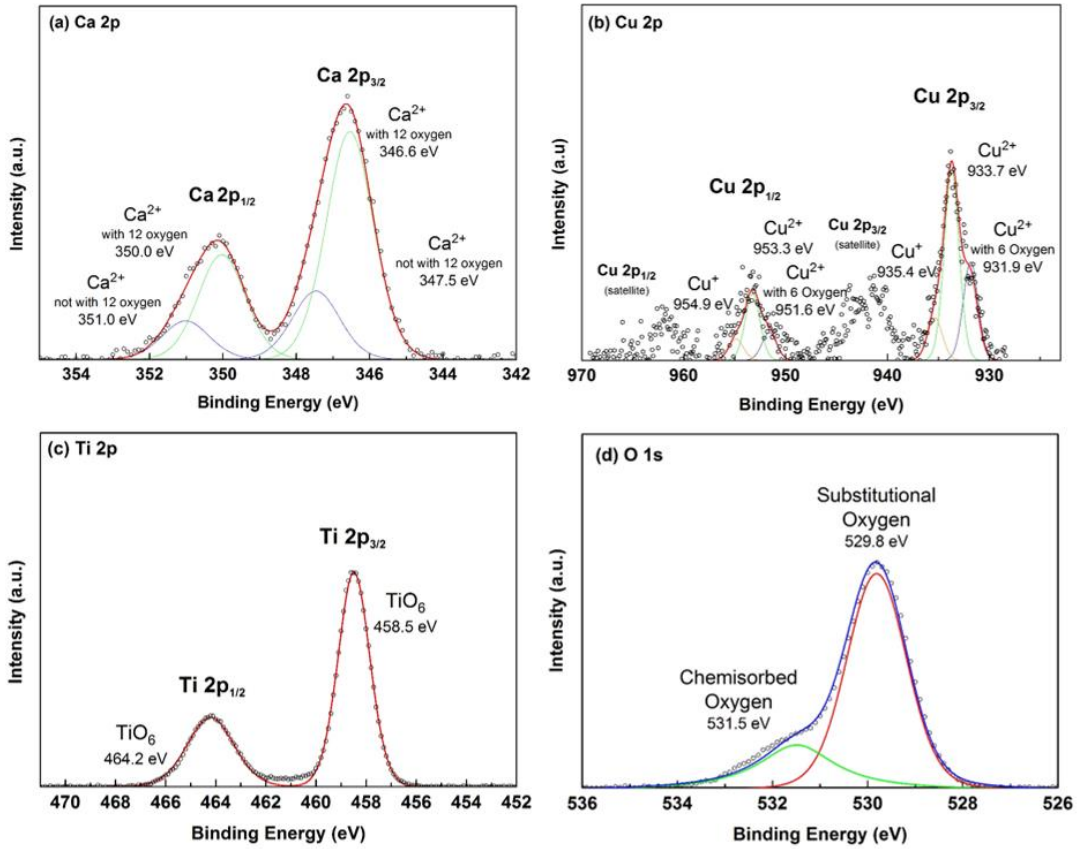

Figure 5.8: X-ray photoelectron spectra (XPS) of (a) Ca 2p, (b) Cu 2p, (c) Ti 2p and (d) O 1s core levels for Ag-doped CCTO films.

In the case of the core level of Ag 3d (Fig. 5.9) for Ag-doped CCTO films, the signal of Ag cannot be detected from XPS measurement. The oxidation state of silver has only one state that is Ag^{+}. It can be seen that it is so noisy in the expected range. The silver peak can be occurred to two dominant Gaussian peaks of Ag $3d_{3/2}$ and $3d_{5/2}$ at binding energies of 374.3 and 368.27 eV [82]. Therefore, it cannot be fitted Gaussian function for data interpretation. This spectrum cannot confirm that the silver dopants are added in the films. However, I have attempted to detect the silver signals using XPS technique. I have used XPS machines from two different places, AXIS Ultra DLD at Thailand Center of Excellent in Physics (ThEP center) and the Petroleum and Petrochemical College, Chulalongkorn University. I expected that the silver

concentrations in the films are too small to detect with the limit of the XPS instruments used in this study. Also as we know, XPS is a surface-sensitive quantitative spectroscopic technique that measures the elemental composition only on the surface and ~10 nm depth from the surface (top 0 - ~10 nm). Later on in next section, I will show the results from EDX and Raman techniques that confirmed the existence of silver dopant in the films.

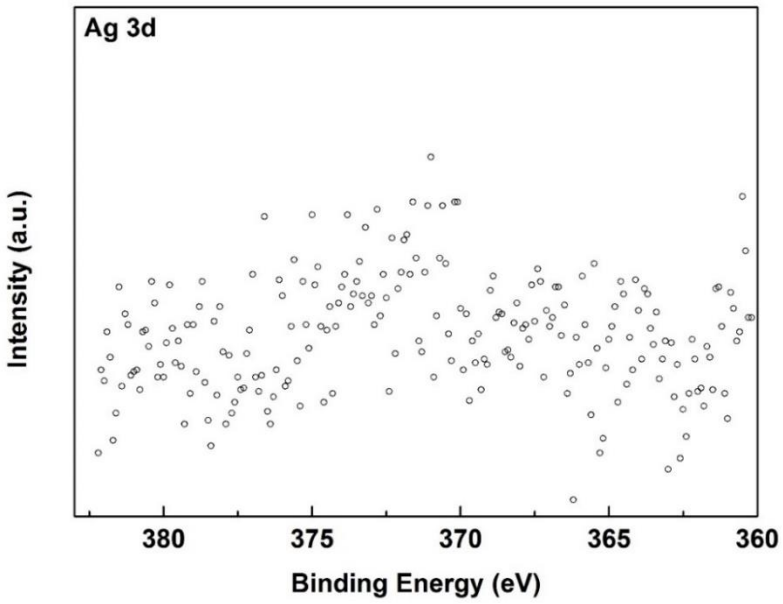

Figure 5.9: X-ray photoelectron spectra (XPS) of Ag 3d core level for Ag-doped CCTO films.

The EDX spectra of 0 and 0.9 wt% Ag-doped CCTO films are shown in Fig. 5.10 (a) and (b), respectively. Both undoped CCTO and Ag-doped CCTO thin films exhibit signatures of calcium (Ca), copper (Cu), titanium (Ti), and oxygen (O). Signals due to silver were only observed when the films were prepared from Ag containing precursor solutions, confirming that Ag-doped films were obtained. And Table 5.1 shows Characteristic X-ray line energies (keV) in the EDX spectra of the undoped CCTO film and 0.9 wt% Ag-doped CCTO film.

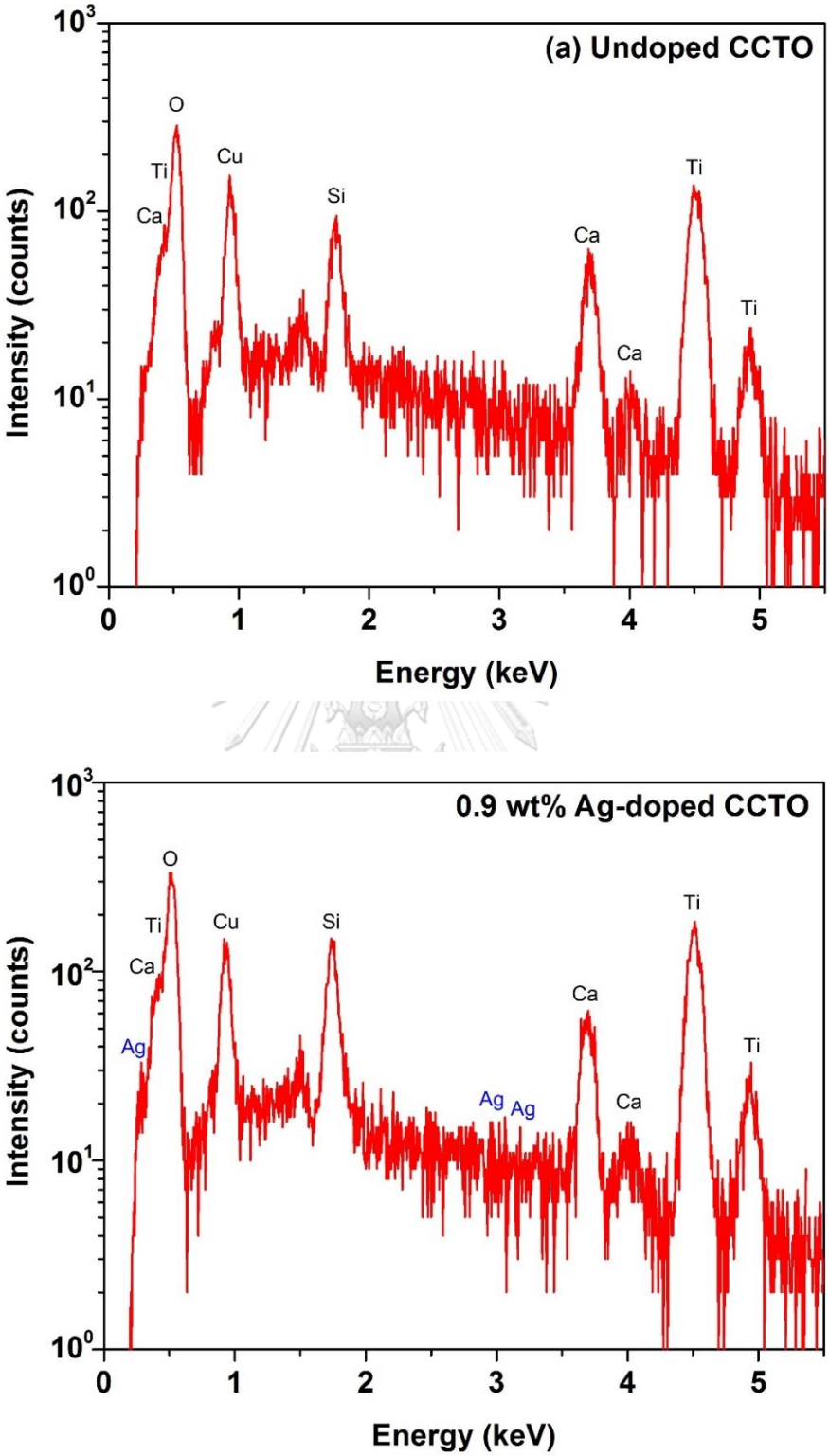

Figure 5.10: The EDX spectra of (a) the undoped CCTO film and (b) 0.9 wt% Ag-doped CCTO film.

Table 5.1: Characteristic X-ray line energies (keV) in the EDX spectra of the undoped CCTO film and 0.9 wt% Ag-doped CCTO film.

Element	K-series (KeV)			L-series (KeV)		
	$K\alpha_1$	$K\alpha_2$	$K\beta_1$	$L\alpha_1$	$L\alpha_2$	$L\beta_1$
Ca	3.69168	3.68809	4.0127	0.3413	0.3413	0.3449
Cu	-	-	-	0.9297	0.9297	0.9498
Ti	4.51084	4.50486	4.93181	0.4522	0.4522	0.4584
O	0.5249	0.5349	-	-	-	-
Ag	-	-	0.27676	2.98431	2.97821	3.15094

Table 5.2 shows the stoichiometry of undoped and Ag-doped CCTO on silicon substrates with different concentration in both of percent by weights and atoms. Figure 5.11 shows the plot of measured Ag doping concentrations and the concentration of Ag in precursor solutions. It can be seen that the linear trend with increasing input Ag concentration in the precursor solution has two characteristics. This data is used to calculate atomic and weight percentages of Ag doping concentrations of all CCTO films. With increasing input Ag concentration in the precursor solution at 0.3 wt% to 0.9 wt%, the measured Ag doping concentration occurred mainly from 0.21 wt% or 0.06 at% to 0.70 wt% or 0.18 at%. From these results, they can be confirmed that Ag is doped into the film.

Table 5.2: The stoichiometry of undoped and Ag-doped CCTO on silicon substrates with different concentration in both of percent by weights and atoms.

Ag doping concentration (wt%)	[Element] in the films									
	Ca		Cu		Ti		O		Ag	
	wt%	at%	wt%	at%	wt%	at%	wt%	at%	wt%	at%
0	6.40	4.23	20.91	8.71	30.11	16.65	42.58	70.42	0	0
0.3	7.80	5.55	17.24	7.74	39.28	23.41	35.47	63.24	0.21	0.06
0.6	7.82	5.50	12.54	5.57	43.31	25.49	35.94	63.32	0.39	0.11
0.9	7.96	5.59	10.63	4.71	44.79	26.32	35.92	63.20	0.70	0.18

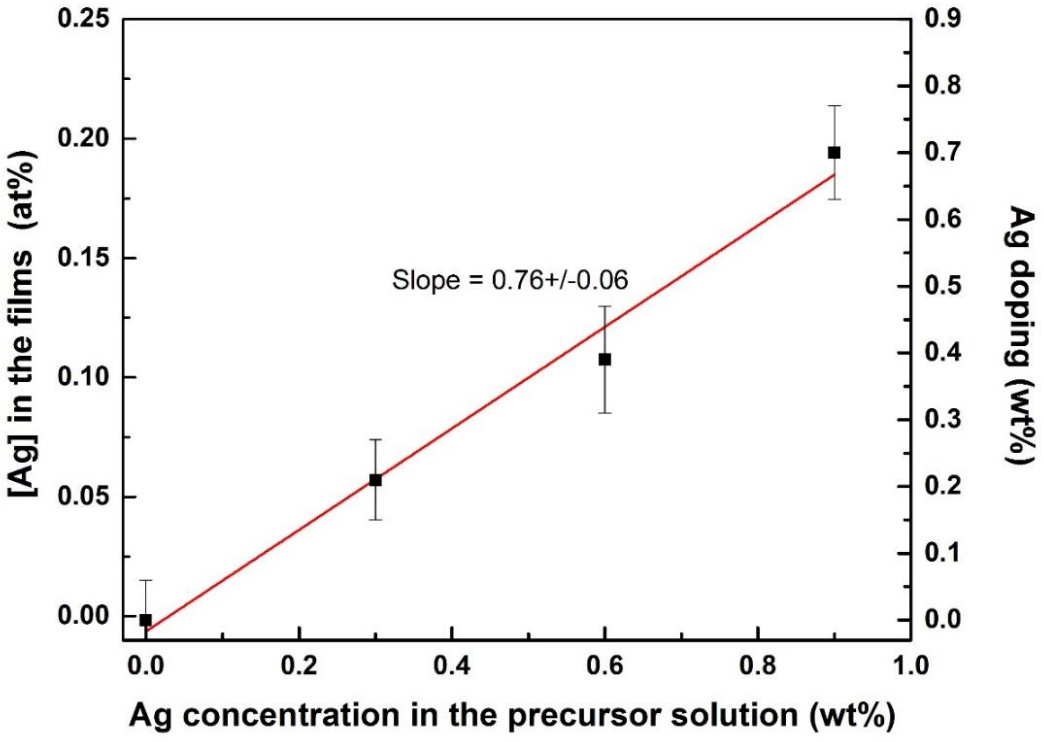

Figure 5.11: The plot of measured Ag doping concentrations and the concentration of Ag in precursor solutions.

Due to the chemical similarity between silver and copper, I expected that Ag atoms will occupy some the Cu sites in the CCTO lattice. To verify this, I observed

dependence of the composition as obtained from EDX analysis versus the aimed film composition as expected from the silver concentration adding in the precursor solution. Figure 5.12 shows the plot of measured Ag doping concentrations and the concentration of Ag in precursor solutions. These data revealed a linearly increasing trend in the Ag concentration in the films and a concerted linearly decreasing trend in the copper content of the films. No clear dependence on the Ag doping was seen in the titanium and calcium contents for the films. These results not only confirm that doping is taking place but also that Ag substitutes the copper positions of the CCTO lattice.

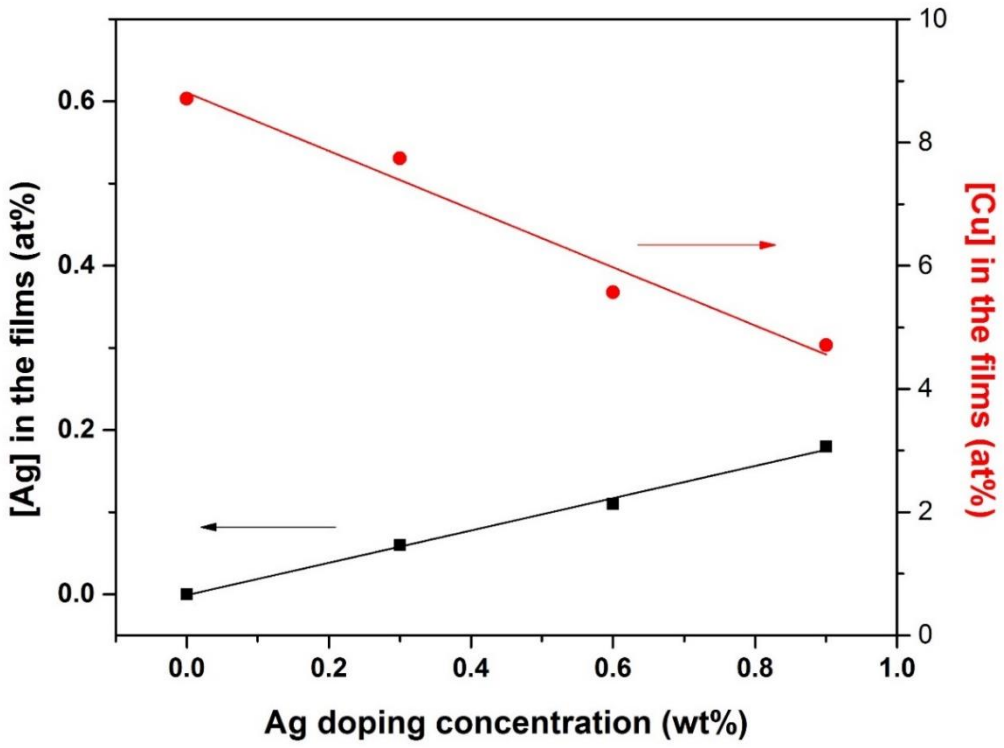

Figure 5.12: The plot of measured Ag and copper concentrations in atomic percent (at%) versus expected the weight percent (wt%) of Ag in CCTO based on silver content of precursor solutions.

In addition to the particular line scan intensity distributions with longitudinal and transverse rod shape displayed in Fig. 5.13 and 5.14, one other interesting finding is that the stoichiometry represented by the Ca, Cu, Ti, O and Ag atoms in the 0.9 wt% Ag-doped CCTO film. These results are not clear at this time. Silver maybe adsorb on the surface of the films and can be formed to the final particle shapes. However, there is no clear that a small signal of silver atom in the films appeared only in rod shape areas.

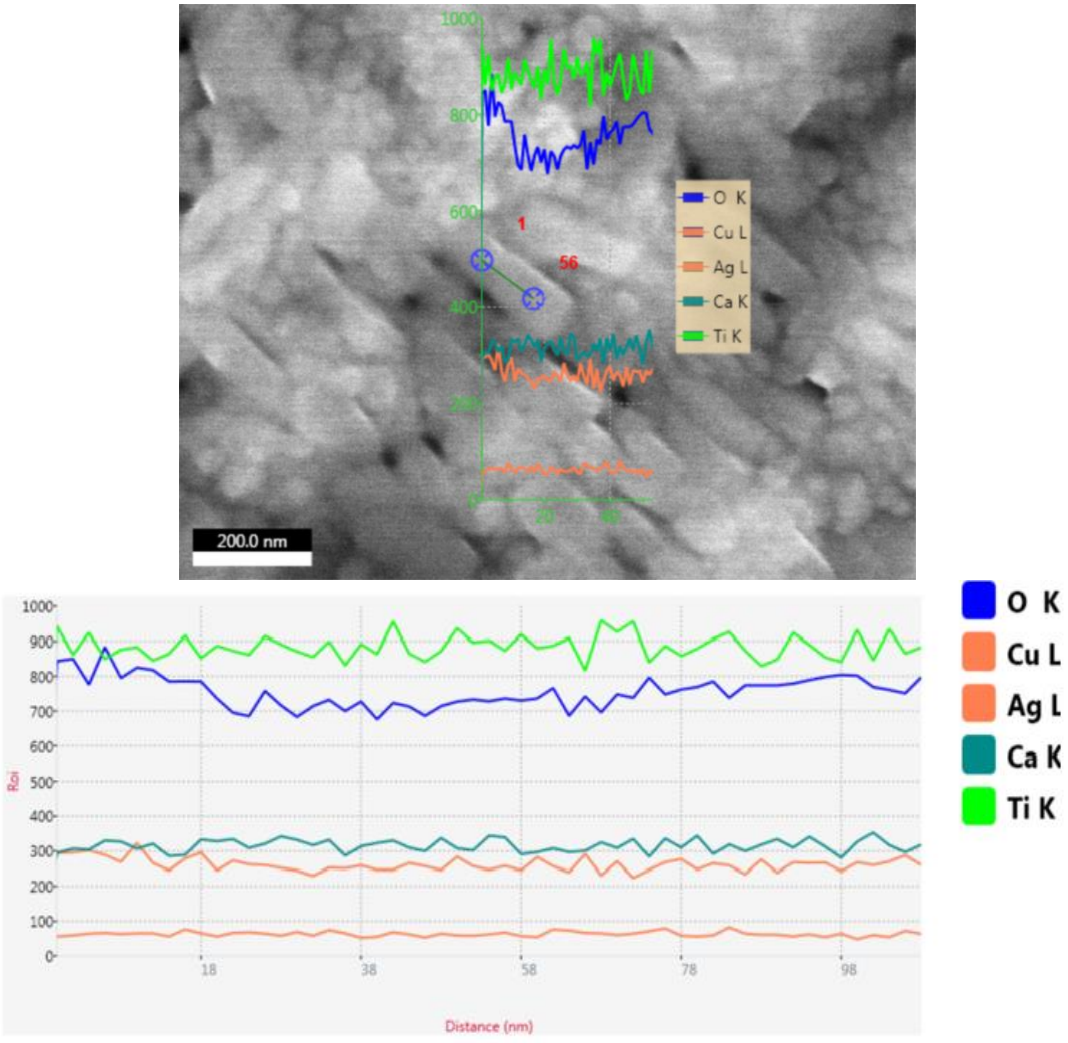

Figure 5.13: The EDX line scan image along rod shape in longitudinal direction of 0.9 wt% Ag-doped CCTO film on silicon substrate annealed at fixed temperature 800 °C.

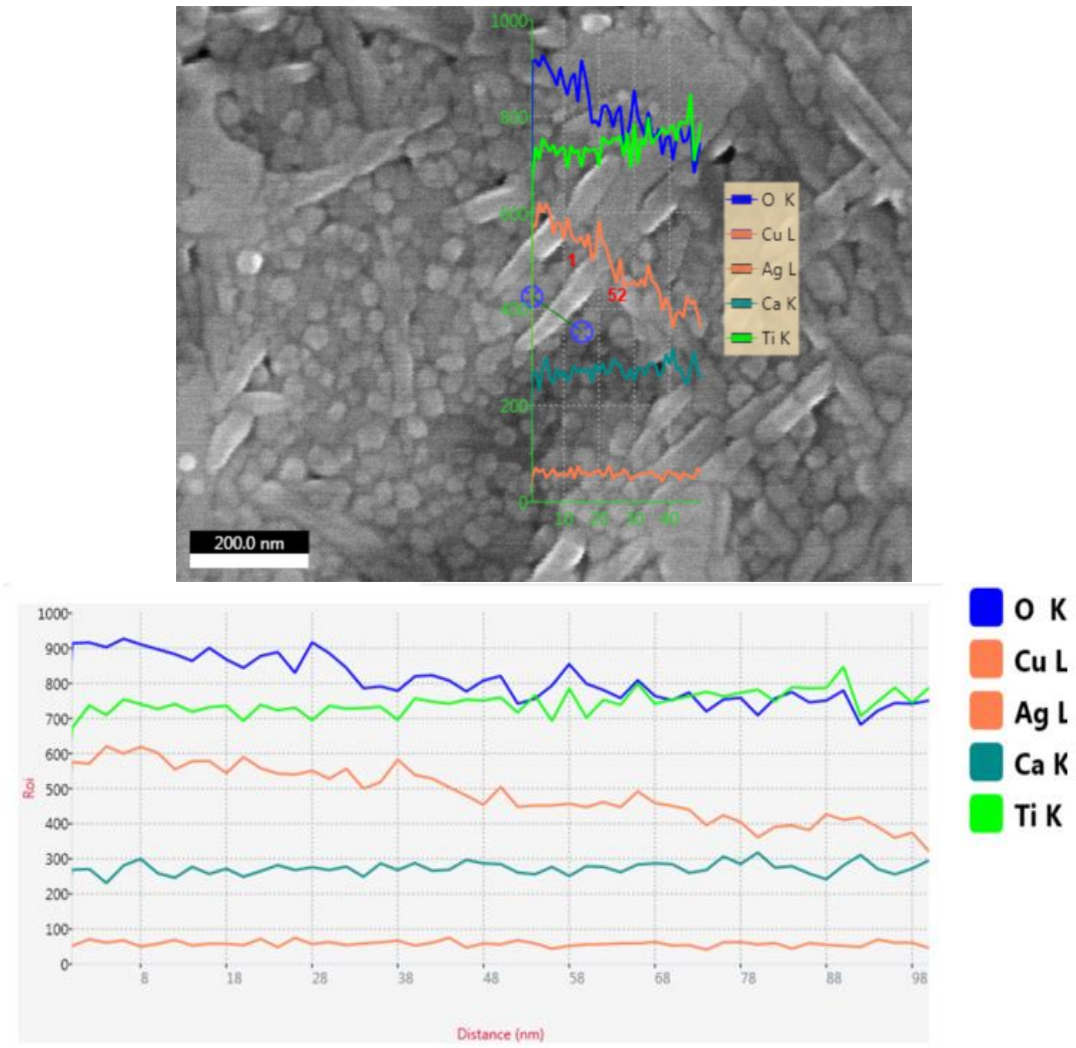

Figure 5.14: The EDX line scan image along rod shape in transverse direction of 0.9 wt% Ag-doped CCTO film on silicon substrate annealed at fixed temperature 800 °C.

5.1.3 Vibration modes of the Ag-doped CCTO films

Raman experiments were carried out to confirm the chemical CCTO structure and the Ag doping of the sensing films. The Raman spectra of the undoped CCTO thin films and Ag-doped CCTO thin films are presented in Fig. 5.15 and 5.16 showing intense bands in the range of 100-1200 cm^{-1}. All samples exhibited the three main peaks at 445, 509 and 577 cm^{-1}. The most dominant peaks at 445 and 509 cm^{-1} can be

associated with the rotation like *Ag*-symmetry of TiO_6. A peak at 577 cm^{-1} can be assigned to *Fg*-symmetry of Ti-O-Ti bending. The band at 750 cm^{-1} is associated with the symmetric stretching-breathing mode of the TiO_6 cage [83]. The weak peak at 246 cm^{-1} may be attributed to O-Ti-O bending mode like seen in $CaTiO_3$ [84]. All these signatures are consistent with the CCTO perovskite structure [41]. Impurities are not significant, with weak bands assigned to rutile TiO_2 seen at 145 and 608 cm^{-1} [85].

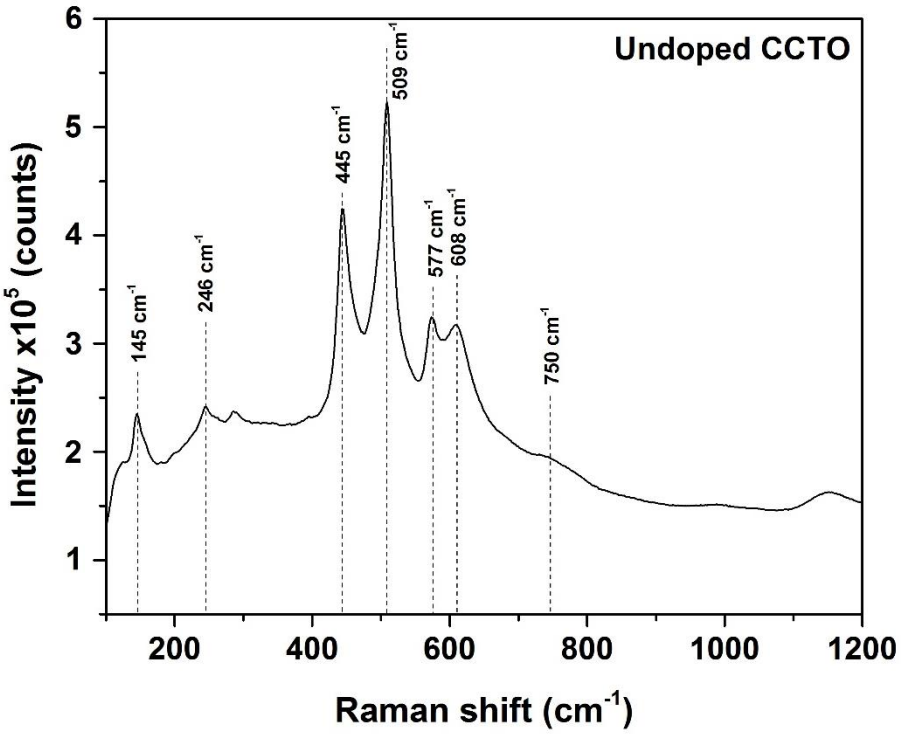

Figure 5.15: Raman spectra of undoped CCTO film.

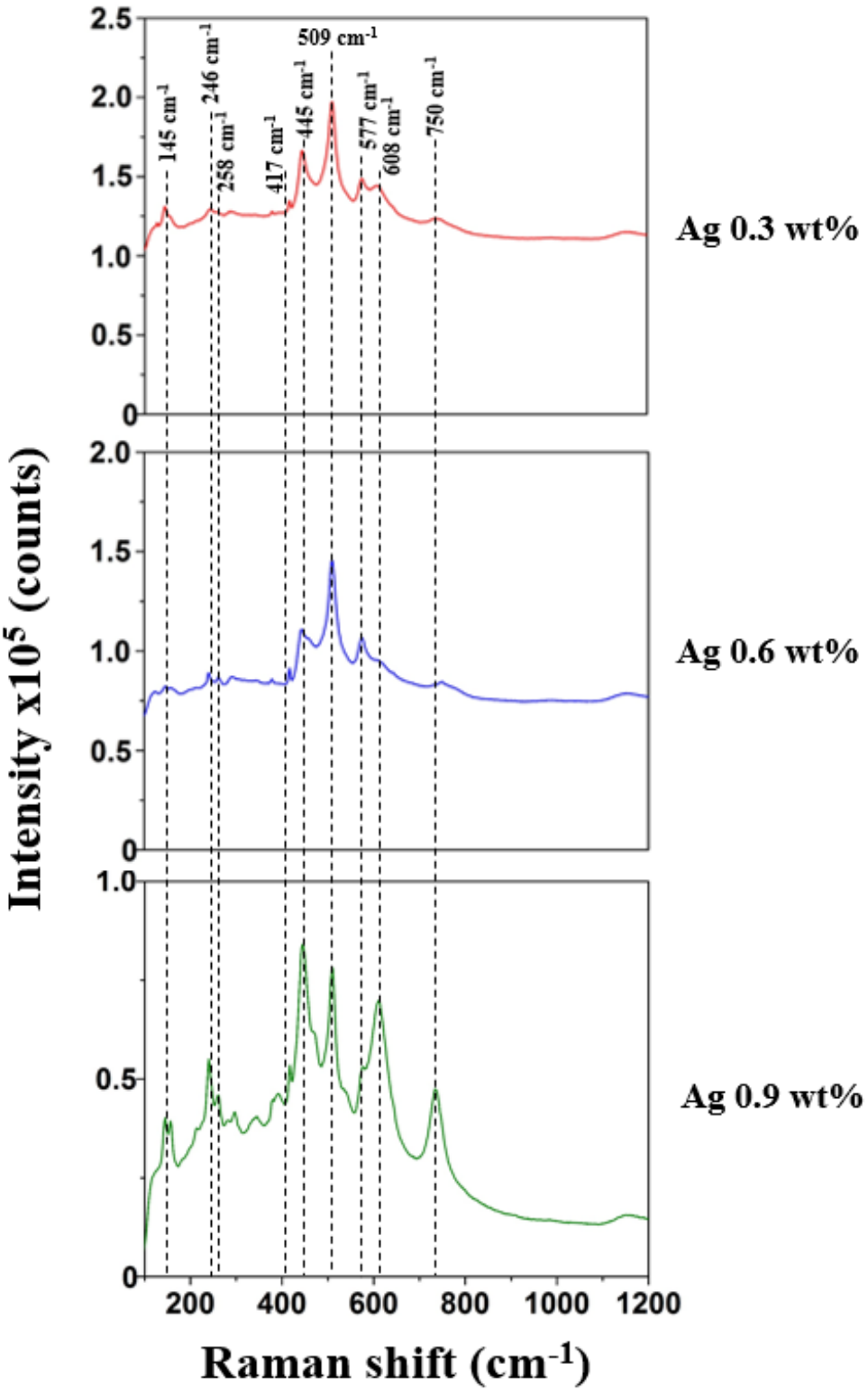

Figure 5.16: Raman spectra of Ag-doped CCTO film.

Figure 5.15 and 5.16 show the Raman spectra of the undoped CCTO films and Ag-doped CCTO films, respectively. It can be seen that the intensity of undoped CCTO films is higher than intensity of Ag-doped CCTO films. The Ag-O vibrations have signatures appearing in the Raman spectrum in the 230-1100 cm^{-1} range [86]. In particular, these results show that the peak at 258 cm^{-1} depends on the level of silver doping concentration and thus it is attributed to one of these vibrational modes of Ag-O bonds [87]. These peaks were fit to a Gaussian curve after subtracting a background to estimate their intensity and verify the correlation between the silver signal and the silver doping concentration. The Equation for two Gaussians fitting is shown in Equation (5.1). In two Gaussians fitting, the Gaussian function is the distribution function for uncorrelated variates the half-maximum points of x_0 and x_1 having a bivariate normal distribution and equal standard deviation (σ_0 and σ_1)

$$f(x_0, x_1) = C + A_0 * \exp\left(\frac{-(x-x_0)^2}{(2*\sigma_0)^2}\right) + A_1 * \exp\left(\frac{-(x-x_1)^2}{(2*\sigma_1)^2}\right) \qquad (5.1)$$

where A_0, A_1 are Raman intensity peak area of the first peak and the second peak.

C is the y-intercept value in term of the intensity.

It can be added the error bars in the results are shown in the Fig. 5.17. In agreement with the EDX analysis, the Raman spectra reveal that as the silver content on the sol-gel precursor solutions is increased, the intensity of the silver peaks increase linearly, further confirming the silver doping of the sensing films.

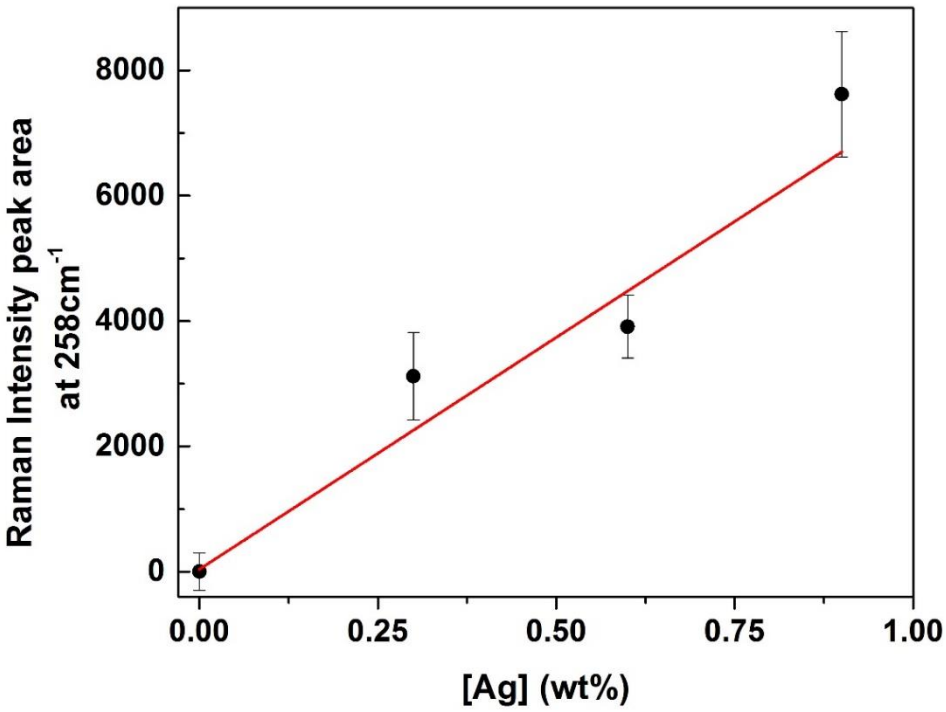

Figure 5.17: The correlation of Ag-O vibration with the silver doping concentration.

5.1.4 Gas sensing results of various reducing and oxidizing gases

The sensing devices made with undoped CCTO films typically had resistances in the range of 10^7-10^8 ohms in the temperature range of 150-350 °C in an air atmosphere. Figure 5.18 shows that the resistance of all silver-doped gas sensors decrease more drastically than that of the undoped CCTO one upon exposure to H2S pulses. The sensor response of the film sensors was tested at the operating temperatures of 150, 200, 250, 300, and 350 °C at H_2S concentration in the range of 0.2-10 ppm in air. Figure 5.16 shows resistance changing of the CCTO films with different the amount of Ag dopants under exposure to various H_2S pulses at different concentrations at an operating temperature of 250 °C. Upon silver doping the resistance tends to decrease approximately one order of magnitude. It is clear that the Ag-doped CCTO sensing

devices show the characteristic switch-on-switch-off response to alternating exposure to H_2S and air with a much higher response with increasing silver doping. Exposure of the sensors to H_2S gas caused an extraordinarily large decrease in resistance in all silver doped gas sensors and a less pronounced decrease for the undoped CCTO sensors. More importantly, the magnitude of the resistance drop decreases with H_2S gas concentration. It is be seen the trend of graph that tends to decrease with decreasing H_2S concentrations. At all H_2S concentrations that be used for H_2S gas testing, 0.9 wt% Ag doped CCTO is the highest resistance changing. And the undoped CCTO sensor is the lowest resistance changing. It illustrates the resistance of all CCTO sensors rapidly decreases after exposing H_2S. It can be confirmed that these films are a typical n-type semiconducting behavior.

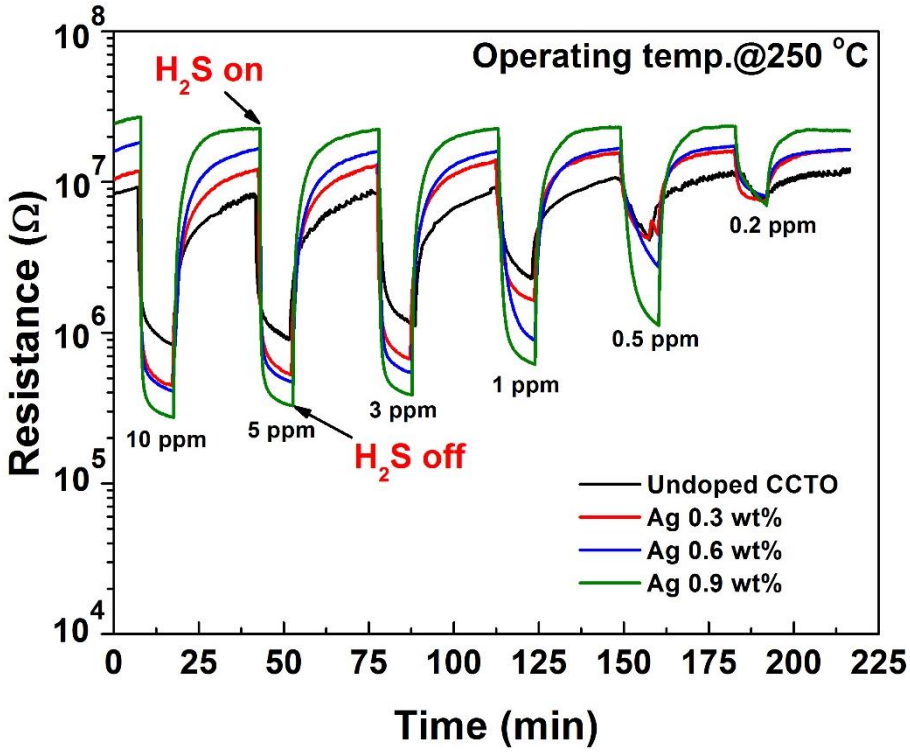

Figure 5.18: Resistance changes for undoped CCTO and Ag-doped CCTO exposed to H_2S gas at 250 °C.

Figures 5.19 and 5.20 show the film sensor response as a function of sensor operating temperature and gas concentration, respectively. The sensor response first rises and then falls with increasing temperature reaching the highest value (~100) for the sensor made with 0.9 wt% Ag-doped CCTO at 250 °C. The optimum operating temperature decreases as the silver doping level increase while the film sensor response increases considerably as shown Fig. 5.19. The response of the Ag-doped CCTO sensors varies nonlinearly at H_2S concentrations smaller than ca. 3 ppm but it becomes nearly linear in the 3-10 ppm range. As seem in Fig. 5.20, the better affinity of the silver doped films towards reacting with at H_2S is evidenced by the nearly tenfold increase of the sensor response when going from undoped CCTO to 0.9 wt% Ag-doped CCTO operating at 250 °C.

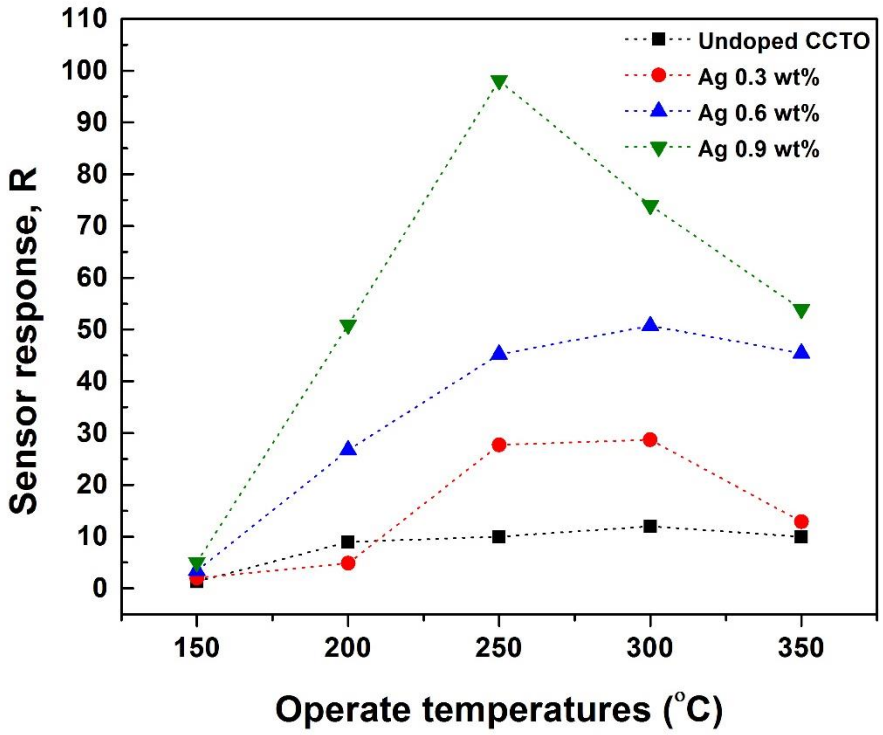

Figure 5.19: Response rate of undoped CCTO and Ag-doped CCTO with operating temperature ranging from 150 to 350 °C to 10 ppm H_2S.

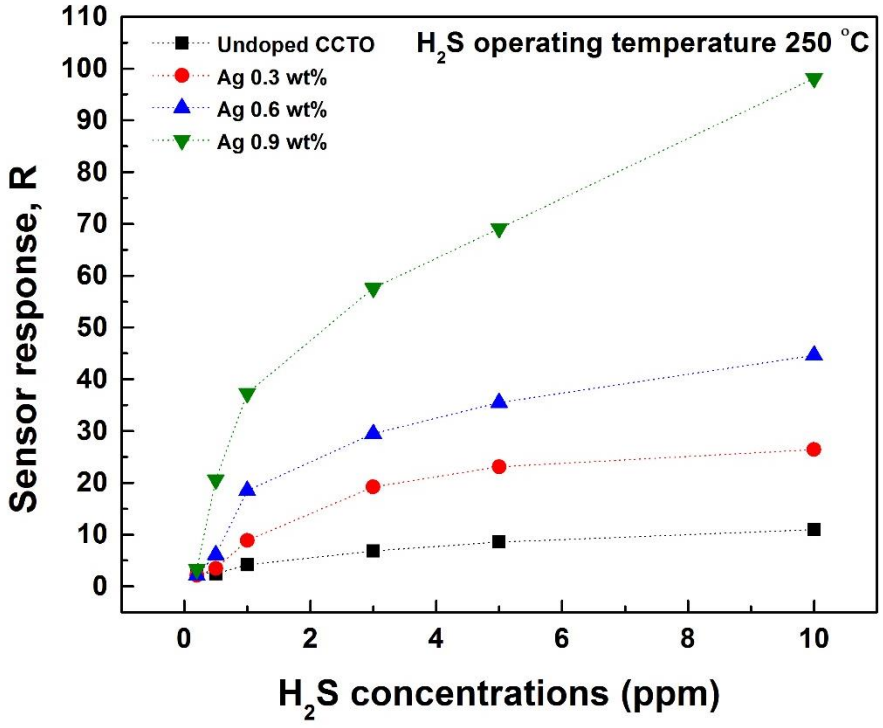

Figure 5.20: Sensor response as a function of H_2S gas concentrations for CCTO sensors with different Ag doping concentration operating at a fixed temperature 250 °C.

To characterize the dynamic behavior of the CCTO films, the response and recovery times were examined. The response time for the gas sensors is defined as the time it takes to the electrical resistance to vary between the 10% and 90% of the steady state resistance obtained after sudden exposure to the stream containing H_2S gas. Analogously the recovery time is measured upon sudden switching from the stream containing the H_2S to pure dry air [88, 89]. Figure 5.21 and 5.22 show the response and recovery times of the Ag-doped CCTO sensors in the presence of H_2S with concentrations varying in the 0.2 to 10 ppm range. The response and recovery times are longest for undoped CCTO, and tent to decrease with silver doping. When the sensors

operate at higher H_2S concentration the response time decreases while the recovery time increases. The response and recovery times of 0.9 wt% Ag-doped CCTO sensor to 0.2, 0.5, 1, 3, 5 and 10 ppm H_2S are 355 and 379 s, 154 and 542 s, 56.7 and 645 s, 13.3 and 833 s, 5.62 and 887 s, 2.96 and 630 s, respectively. On one hand, a shortening of the response time is to be expected from an increase of the occupation of active sites where H_2S binds on the film surface at higher target gas concentration. On the other hand, longer recovery times are in line with removal of larger concentrations of the excess electrical carriers deposited in the film by the reaction with the target gas. So, the smallest number of response and recover times belong to 0.9 wt% Ag-doped CCTO sensor to 10 ppm H_2S. These results can be indicated that 0.9 wt% Ag-doped CCTO sensor has excellent response to H_2S.

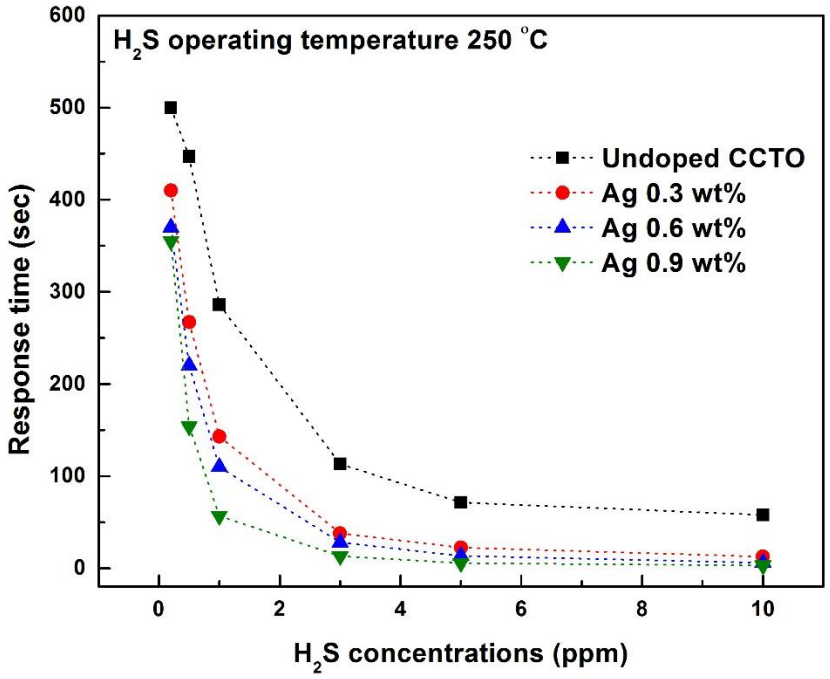

Figure 5.21: The typical response time of Ag-doped CCTO sensor to different H_2S concentrations (from 0.2 to 10 ppm).

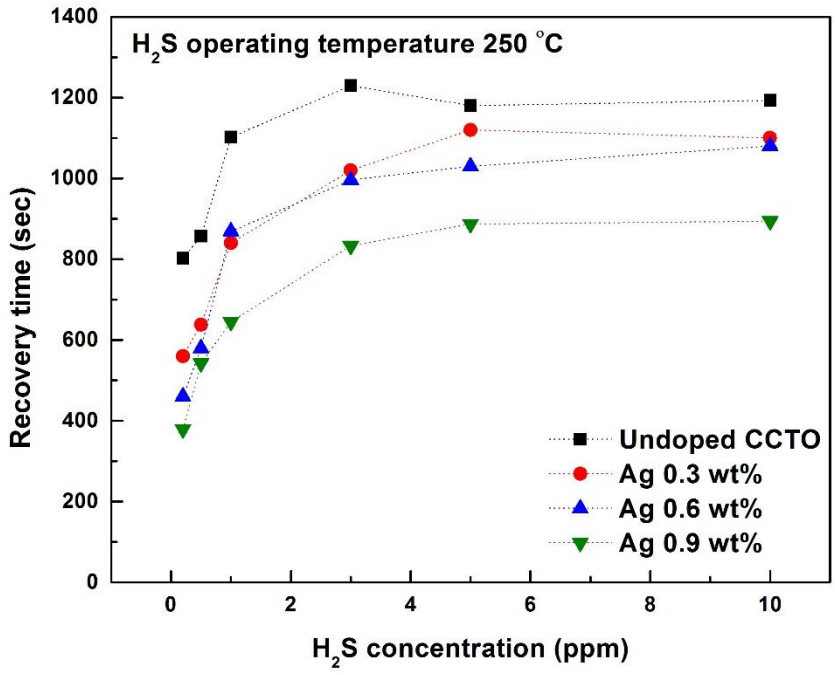

Figure 5.22: The typical recovery time of Ag-doped CCTO sensor to different H_2S concentrations (from 0.2 to 10 ppm).

Ideally a gas sensor should be able to selectively respond to a single component. Thus, the selectivity is a very important performance parameter of gas sensor. Insight about the selectivity to H_2S was obtained by measuring the response of the Ag-doped CCTO sensors towards NH_3, H_2, NO_2 and C_2H_5OH beside H_2S. These tests were conducted at the optimum temperature of 250 °C found for H_2S. The results are shown in the histogram of Fig. 5.23. All CCTO sensors exhibit a high contrast in the relative response to the tested gases, with highest response to H_2S, a small response to NO_2 and negligible response to NH_3, H_2 and C_2H_5OH which were at concentrations 2 to 3 orders of magnitude higher than that for H_2S. The selectivity for H_2S of CCTO film sensors tends to improve with silver doping, and the highest Ag doping level exhibited the highest response contrast.

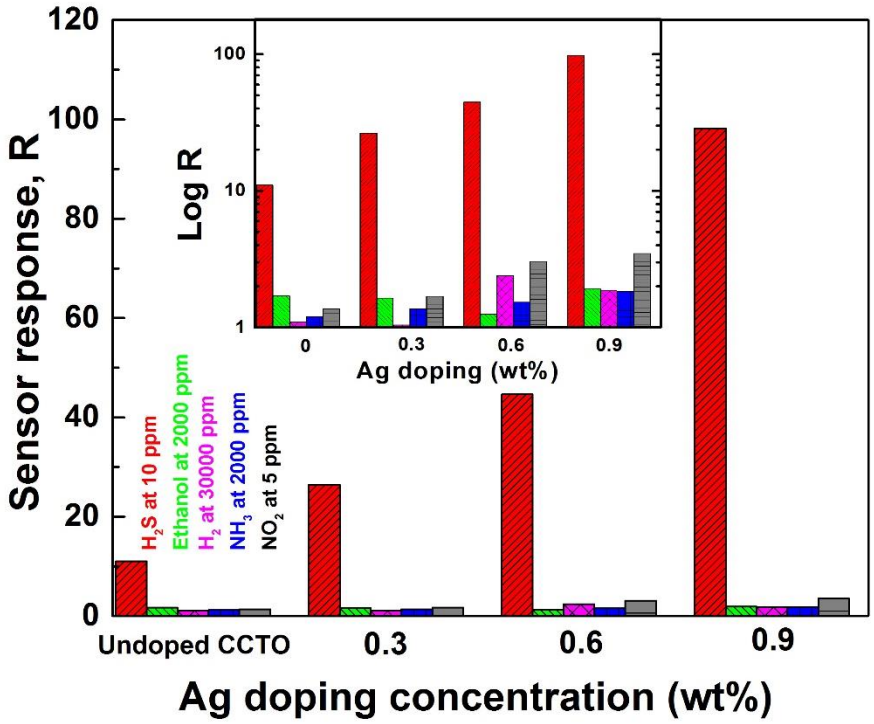

Figure 5.23: Selectivity histograms exhibited by the undoped CCTO and Ag-doped CCTO sensors towards various gases at 250 °C.

Sensor response of films with different gases were obtained by taking the response rate from selectivity histograms to plot as shown in Fig 5.24. It can be seen that all test gases exhibited small response below 5. Also the trends in the graphs for ethanol and H_2 testing are not linear as compared with the results from the H_2S gas testing. It can be concluded that the surface area of the films does not relate the sensor response of films rather than the reaction between specific gases (e.g. NH_3, NO_2, H_2S) and CCTO film surface.

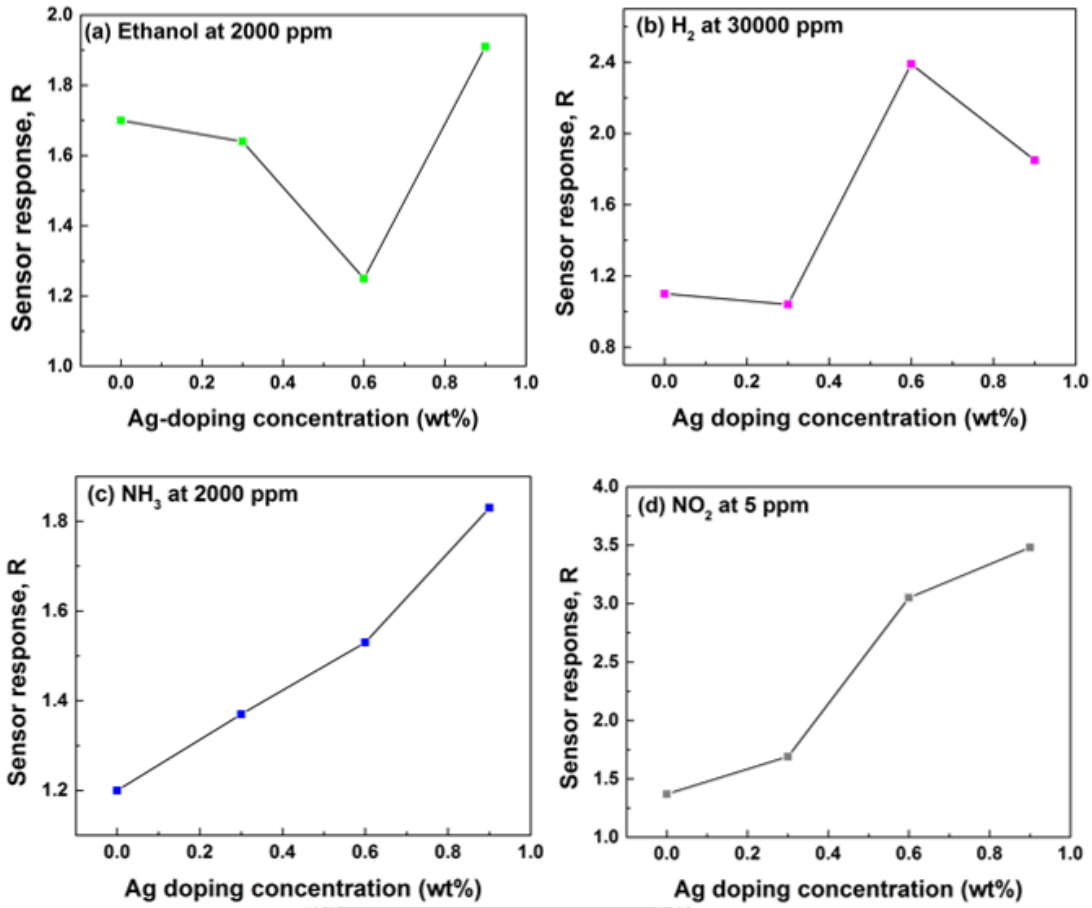

Figure 5.24: Sensor response of undoped CCTO and Ag-doped CCTO with operating at a fixed temperature 250 °C to different gases (a) Ethanol at 2000 ppm, (b) H_2 at 30000 ppm, (c) NH_3 at 2000 ppm and (d) NO_2 at 5 ppm.

Gas sensing response of recently reported metal oxide sensors towards H_2S and several gases, the 2 wt% Ag-doped α-Fe_2O_3 nanoparitcles exhibited the maximum response (220) to H_2S at 100 ppm [11]. It's too high H_2S concentration. In addition, it displays a low optimal operating temperature compared with our work. The Ag/TiO_2 nanofibers at the same H_2S concentration with our work, have higher optimal operating temperatures (350 °C) [15]. Ag doped SnO_2 on ceramic substrate exhibited the sensor

response of 91.2 to high concentration of H_2S at low operate temperature [90]. It was investigated the effect of Ag-doped CCTO thin films towards H_2S and finally to compare with that of Fe-doped CCTO thin films. In particular, 9 wt% Fe-doped CCTO sensor exhibited the highest response of ~126 to 10 ppm H_2S [41]. The response rate of 0.9 wt% Ag-doped CCTO sensor is higher than 7 wt% Fe-doped CCTO sensor. And the response time of 0.9 wt% Ag-doped CCTO is smaller than 9 wt% Fe-doped CCTO. It can be concluded in the Table 5.3. Thus, Ag-doped CCTO sensor with small doping concentration exhibits an excellent candidate for developing H_2S sensors operating at low-temperatures.

Table 5.3: Comparison H_2S-sensing properties between Ag-doped CCTO and Fe-doped CCTO.

Gas-sensing properties	**Undoped CCTO**	**Fe-doping concentrations (wt%)**				**Ag-doping concentrations (wt%)**		
		3	**5**	**7**	**9**	**0.3**	**0.6**	**0.9**
Sensor response	11.0	13.4	29.0	46.0	126.4	26.4	44.6	98.7
Response time (sec)	57.9	~30	~20	~10	~8.5	12.5	5.94	2.96
Recovery time (sec)	1,192.97	~1,100	~900	~800	~500	1,100	1,080	894

5.1.5 Mechanisms for enhanced H_2S gas sensing performance of the Ag-doped CCTO films

It is generally accepted that in the absence of the target gas the sensing material will be in a state deprived of carriers by effects of oxygen reactions at the surface. The first step is the chemisorption of oxygen which involves the reactions [91].

$$\begin{aligned} O_2^{gas} + e_{surf}^- &\rightleftarrows O_{2\ adsorbed}^- \\ O_2^{gas} + 2e_{surf}^- &\rightleftarrows 2O_{adsorbed}^- \\ O_{2\ adsorbed}^- + 2e_{surf}^- &\rightleftarrows 2O_{adsorbed}^- \end{aligned} \qquad (5.2)$$

The electrons supplied by the oxide become trapped at the sites where oxygen species attach losing their charge carrier nature. Oxygen may also react with crystal defects that contain an oxygen deficiency at certain metal ion (denoted by $V_O^{\bullet\bullet}$). In this process oxygen diffuses until it encounters the oxygen vacancy and becomes bound to the corresponding metal ion, immobilizing a pair of electrons at that lattice point.

$$\frac{1}{2}O_2^{gas} + V_O^{\bullet\bullet} + 2e^- \rightleftarrows O_{lattice}^{2-} \qquad (5.3)$$

In an n-type semiconductor material like CCTO [41, 83] the chemisorption of oxygen extracts electrons from the conduction band and reduces the conductivity of the material. Concurrently with the charge carrier trapping, an accumulation of negative charges at the surface and a depletion of carriers in the proximity of the surface leads to band bending [92]. The effects of the band bending are similar to the field effect modulation of the conductivity in field effect transistors.

Upon exposure to the reducing H_2S target gas, competitive replacement of trapped oxygen ions, as well as adsorption followed by reaction with adsorbed oxygen species sets in, injecting excess electrons in the materials [93, 94].

$$
\begin{aligned}
&H_2S_{(gas)} \underset{k_{-1}}{\overset{k_1}{\rightleftarrows}} H_2S_{adsorbed} \\
&2H_2S_{adsorbed} + 3O^-_{2\ adsorbed} \xrightarrow{k_2} 2SO_2 + H_2O + 3e^- \\
&H_2S_{adsorbed} + 3O^{2-}_{adsorbed} \xrightarrow{k'_2} SO_2 + H_2O + 6e^- \\
&5O^x_{lattice} + H_2S_{adsorbed} \xrightarrow{k''_2} SO_4^{2-} + H_2O + 3V_O^{\bullet\bullet} + 6e^-
\end{aligned}
\qquad (5.4)
$$

These processes neutralize the carrier depletion, repopulates the conduction band and reverts the band bending, effectively increasing the conductivity of the sensor. These results clearly suggest that the presence of silver atoms play a role on these surface reactions. The strong affinity of silver ions for sulfur is a well-known fact. This is why adding Ag to the composition of the films for fabricating sensors would have beneficial effects on their sensing abilities. While this has indeed been observed, the actual mechanism by which Ag make the sensors more sensitive and selective can vary depending on the host material used [95]. It has been argued that silver can act in two possible ways. On one hand, silver can provide highly specific binding sites on the CCTO surface to facilitate the adsorption of H_2S increasing the response for the same amount of target gas [15]. On the other hand, silver may also provide catalytic centers to the oxidation of adsorbed H_2S molecules which injects electrons into the conduction band of the CCTO at which change the conductivity of the films [11].

Insight about the role of silver doping in CCTO for the sensing H_2S may be obtained by inspection of dependence of response time or recovery time of these doped CCTO sensors as a function of silver doping. The zero order expectation is that the rate

of conversion of H_2S from the gas phase into carriers injected in the film follows the Langmuir isotherm,

$$\Theta_{H_2S} = \frac{K_{H_2S} \cdot P_{H_2S}}{1 + K_{H_2S} \cdot P_{H_2S}} \quad (5.5)$$

where Θ_{H_2S} is the surface coverage, P_{H_2S} is partial pressure of H_2S, K_{H_2S} is the adsorption equilibrium constant. In the sensing measurements, the partial pressure of H_2S is very low leading to the limiting case, $\Theta_{H_2S} \approx K_{H_2S} \cdot P_{H_2S}$. The rate k_r at which H_2S reacts with the oxygen species from the surface is proportional to the surface coverage of H_2S, $k_r = k_2 \cdot \Theta_{H_2S}$. The rate of resistance change is directly related to the charge carrier concentrations in the CCTO film. Thus the resistance change is expected to be proportional to k_r. Based on these premises, I first obtain the response rates by taking the reciprocal of the response times shown in Fig. 5.21 which indeed yield nearly linear functions of the H_2S concentration at all the Ag doping levels. The slope of these plots represents the effective response rate (k_{eff}), for which the dependence on the silver doping concentration is plotted in the inset on Fig. 5.25.

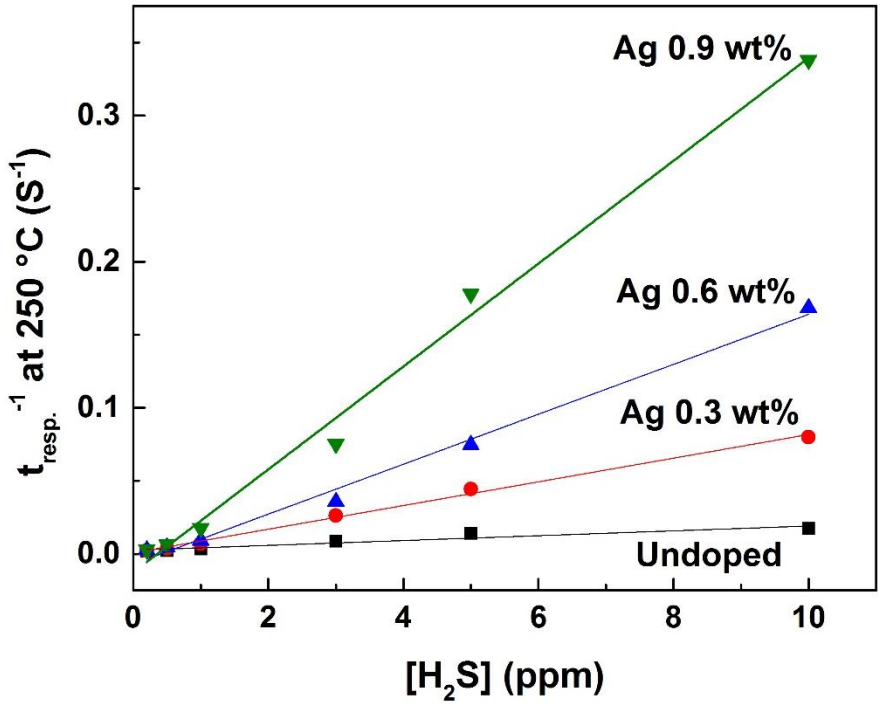

Figure 5.25: Dependence of the sensor response rate on H_2S concentration.

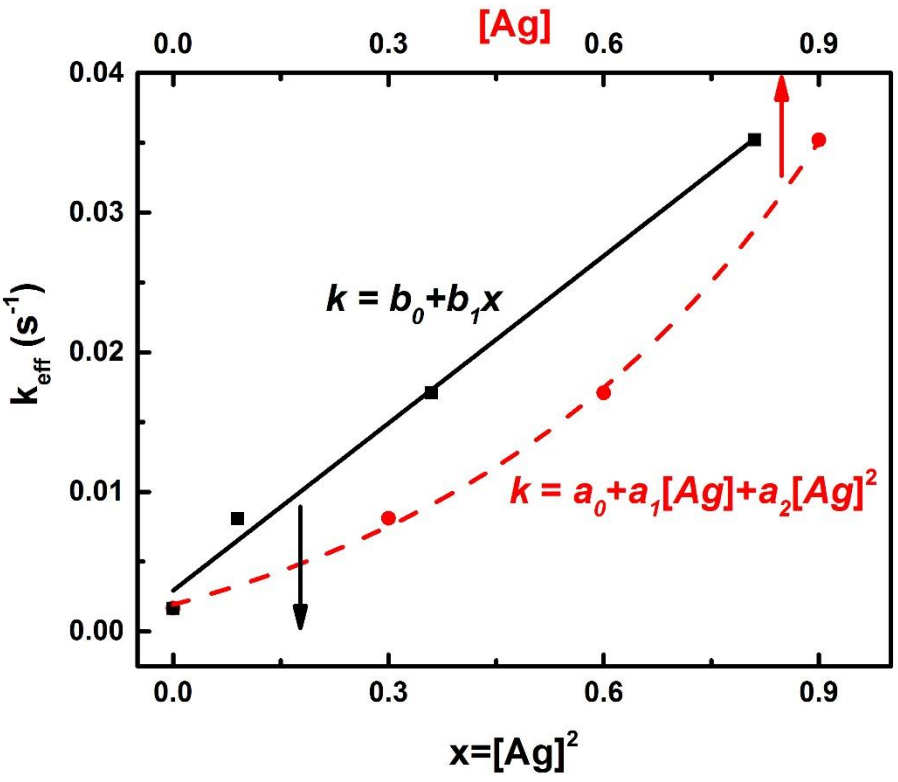

Figure 5.26: The specific response rate versus the square of the silver doping concentration (black squares) and linear fit (black solid line). The red solid circles represent the specific sensing response rate versus the silver doping concentration and the red dashed line is a quadratic fit.

The dependence of the effective rate on the silver doping concentration represents the reaction order on the catalyst in a chemical kinetics sense as shown in Fig. 5.26. Interestingly the effective rate depends quadratically on the silver doping concentration. If the rate determining reaction step in the response of the sensor involves a catalytic step promoted by silver ions, then the effective response rate would be linearly proportional to the concentration of the catalyst. This result may be rationalized by taking onto consideration that the silver atoms can interconvert between the Ag^{+} ion and the Ag^{0} state via a single electron transfer. Although the reaction in Equation 5.4 appear to be a single step they most likely involve a more complex mechanism with sequential electron transfer. Adsorption of H_2S may take place by sharing electrons between the sulfur atom and the binding silver ion site forming a chemical bond, as well as via hydrogen-bonding to oxygen species at the surface. Electron transfer from the sulfur ion into the silver ion causes the Ag-S bond to break at the same time the Ag^{+} ion gets reduced to Ag^{0} while the H_2S gets oxidized to a hydrosulfide radical (HS•). Because silver cannot take a second electron, the HS• cannot be further oxidized to S^{0} until a second silver ion can take a second electron. The reaction at this point may proceed by binding to a second Ag^{+} ion in close proximity which then abstracts a second electron to form a sulfur atom and Ag^{0}. The reduced silver atoms in the CCTO lattice rise the Fermi level, essentially sharing the extra

electron with the conduction band. The fate of the sulfur atom is essentially a combustion with surface adsorbed oxygen species ultimately leading to the formation of SO_2 gas. I would like to represent this mechanism in a pictorial way on Fig. 5.27.

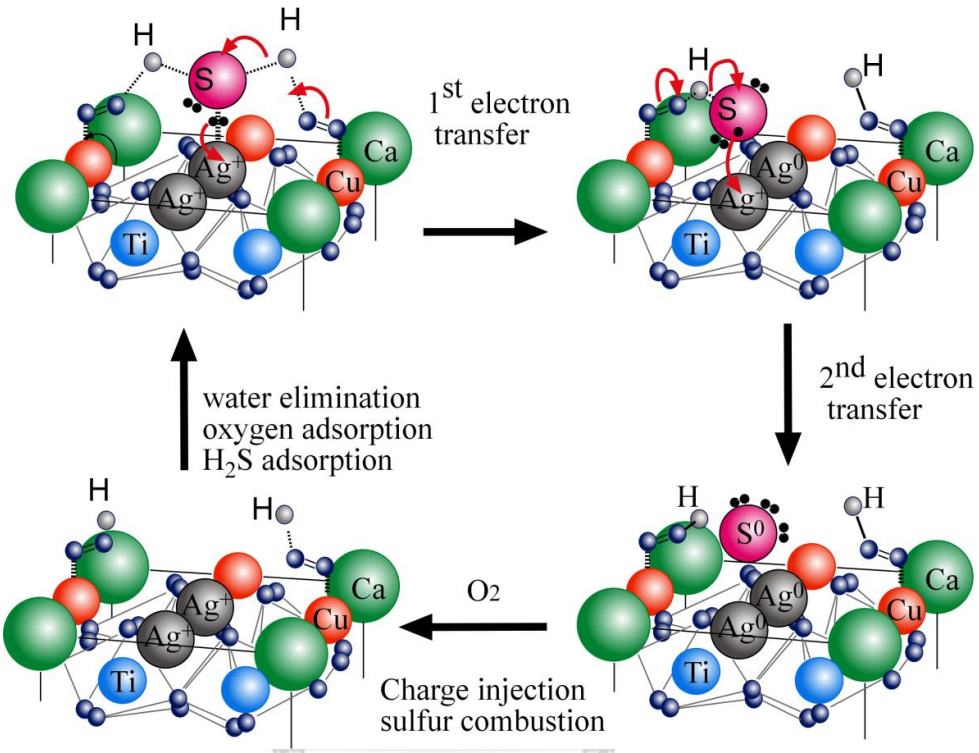

Figure 5.27: Schematic representation of a catalytic cycle with sequence of events that would be consistent with a second order dependence on the silver doping concentration of CCTO.

The possibility for this mechanism relies on the existence of surface catalytic sites containing two silver atoms at distances comparable to the dimensions of the H_2S molecule. Although our CCTO films are polycrystalline, at the length scale of the reaction site we can assume that crystal facets with the characteristic crystal structure are exposed. It is not unlikely to find two silver ions in the same unit cell substituting a

pair among the 18 of copper ions present in the facets of CCTO cell. The atom substitution probability is given by a Poisson distribution, which naturally leads to a quadratic dependence of the abundance of the sites having two silver ions substituting copper ions per unit cell facet, and also goes in line with the quadratic dependence on the silver doping. It is important to remark that our interpretation is a zeroth order explanation of silver doping effect. According to this hypothesis, the enhancement of H_2S response by silver doping should settle in a plateau once there are two or more silver ions per CCTO unit cell corresponding to more than 10 mole%, which is much higher than the maximum Ag doping level that can be achieved by this sol-gel method. Thus, the optimal Ag doping concentration cannot be experimentally verified within this work. Furthermore, the crystal and band structures of CCTO are expected to be significantly altered at very high Ag doping levels, causing a change in the gas-sensing mechanism that may not conform to the current proposed model of this system. Hence, additional experimental and theoretical studies will be needed to further determine the effect of Ag doping at high concentrations. Nevertheless, the findings of this work suggest that dopants that strongly interact with sulfur via the transfer of two electrons such as Mn, Mo, Co and Ni are promising candidates for enhancing the CCTO response towards H_2S.

Catalytic reaction was considered from the amount of Ag-doping concentrations. Silver dopants make the sensors more sensitive to different H_2S gas concentrations. Figure 5.28 shows the response time of Ag-doped CCTO sensors in the presence of Ag-doping concentrations with different H_2S concentrations varying in the 0.2 to 10 ppm range. It can be seen that the response times are tend to decrease with

silver doping. Therefore, catalytic reaction and surface reaction can even cause an enhanced sense of sensing.

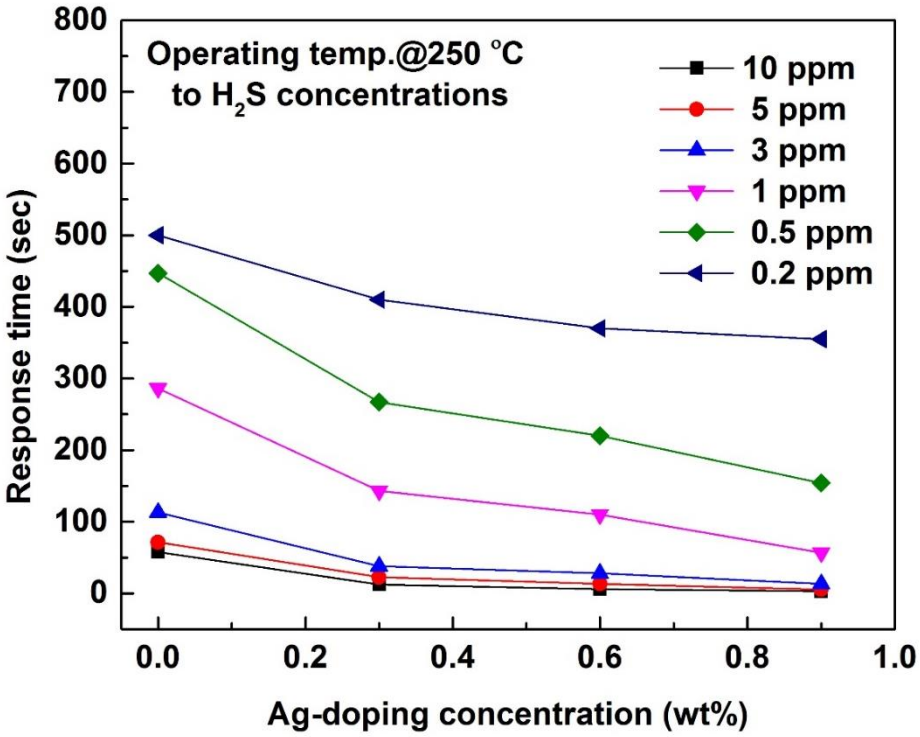

Figure 5.28: The response time of the Ag-doped CCTO sensors with different H_2S gas concentrations at a fixed temperature 250 °C.

5.2 Results and discussion for silver perchlorate as the Ag dopant in CCTO films

From Table 4.1, silver acetate has a limit of solubility. The limit for Ag-doping of silver acetate is 0.9 wt%. We have searched other silver compounds that can be highly dissolved in the precursor. Silver perchlorate will be excellent candidate for Ag-doped CCTO preparation because it has a high solubility in acetic acid as shown in Appendix C. The crystal structure of Ag-doped CCTO films containing Ag concentrations of 1, 3, 5, 7 and 9 wt% were studied using XRD technique. It is similar to the XRD results of silver acetate as the Ag dopant in CCTO films that were shown in the previous section (see Fig. 5.1 ad 5.2). The EDX spectra of 9 wt% Ag-doped CCTO films was shown in Fig. 5.29. In fact, I tried to detect silver signals in all films, but all the plots are the same thus here I only show the result from the maximum silver doping concentration. The spectra confirmed the presence of calcium (Ca), copper (Cu), titanium (Ti), and oxygen (O) the film and silver (Ag) cannot be detected in the doped film. Table 5.3 shows the stoichiometry of undoped and 9 wt% Ag-doped CCTO on silicon substrates with different concentration in the percent by weights. It can be seen that the stoichiometry of undoped film is similar to 9 wt% Ag-doped CCTO film. In addition, the intensity of Cu peak 9 wt% Ag-doped CCTO does not decrease. It can be confirmed that silver cannot be add in the films.

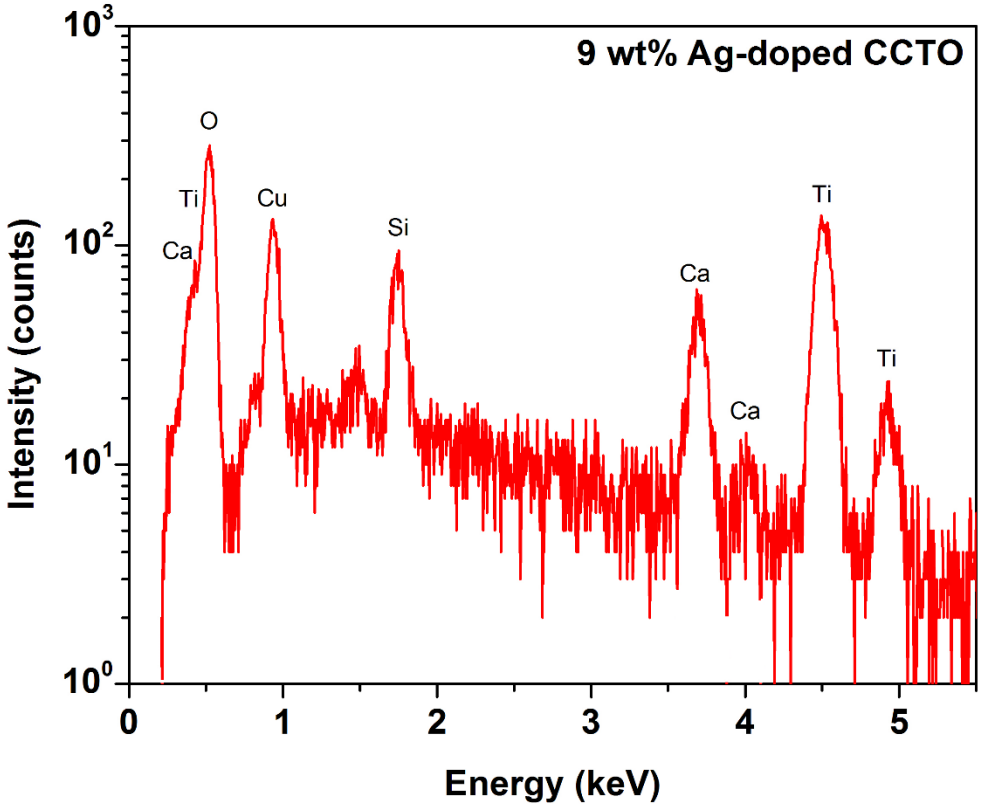

Figure 5.29: The EDX spectra of 9 wt% Ag-doped CCTO film.

Table 5.4: The stoichiometry of undoped and 9 wt% Ag-doped CCTO on silicon substrates with different concentration in the percent by weights.

Ag doping concentration (wt%)	[Element] in the films (wt%)				
	Ca	Cu	Ti	O	Ag
0	6.40	20.91	30.11	42.58	0
9	6.82	19.20	31.45	42.51	0.02

It can be confirmed that silver dopants were not added into the precursors from gas sensing properties. Figure 5.30 shows the change in resistance of 9 wt% Ag-doped CCTO film under exposure to various H_2S pulses at different concentrations at an operating temperature of 250 °C. It can be seen that the response rate is approximately

11. It is almost the same with the undoped film that is shown in the previous section (see Fig. 5.18).

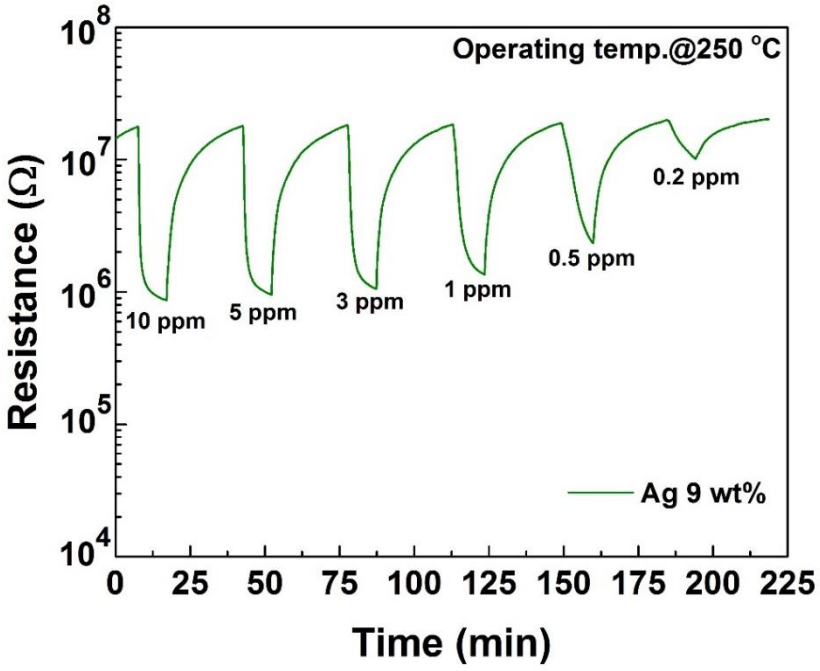

Figure 5.30: Change in resistance of 9 wt% Ag-doped CCTO film under exposure to various H_2S pulses at different concentrations at an operating temperature of 250 °C.

CHAPTER VI
CONCLUSION

In this thesis work, I have used two silver compounds (silver acetate and silver perchlorate) acting as dopants to synthesize the Ag-doped CCTO films by a sol-gel spin coating technique. For each batch of precursor, either silver acetate or silver perchlorate was added into separate precursor solutions. For the first silver compound, I have chosen silver acetate to be the dopant because it is a compound of acetate which are the same acetate starting compounds like copper acetate and calcium acetate. Silver acetate with small concentrations up to 0.9 wt% (~1.7% by mole) can be dissolved in the precursors. For the second silver compound, silver perchlorate was selected to be a candidate as one of possible dopants because of higher solubility in acetic acid. However, I discovered that it is not be a good candidate to synthesize Ag-doped CCTO thin films because no silver signals were detected in EDX experiment and the sensing response value was the same (~ 11 at H_2S concentration = 10 ppm) as that of undoped CCTO films. The reasons why using silver perchlorate did not work in my experiment are still questionable. Thus, most of characterizations of the films including their sensing properties reported in this thesis are from the Ag-doped CCTO thin films prepared by using silver acetate as a silver dopant.

Silicon (Si (100)) and alumina (Al_2O_3) substrates were used for the Ag-doped CCTO thin films deposition. In Chapter 5, I have explained and illustrated the CCTO thin film depositions, their characterizations and gas sensing properties as well as their results. For the conclusion of this study, I will conclude as follow:

According to XRD patterns on silicon and alumina substrates, they confirmed the structure of CCTO and investigated small amount of impurities evidenced some weak diffraction TiO_2 (110) rutile signals and there are no signs of any Ag oxides in XRD patterns. It is also interesting to note that with increase in Ag concentrations, the intensity of CCTO peaks decrease. It can be confirmed that the Ag doping can occur in the films without distorting the crystal structure of CCTO. From surface morphology on silicon and alumina substrates, it exhibited some spherical/rod-like disperse on surface with the doped films. The cross section image of the Ag-doped CCTO films on alumina substrate that the film thickness is approximately 360 to 500 nm for four layers. The film thickness is approximately 330 to 540 nm for four-layered deposition on silicon substrates. XPS analysis confirmed the oxidation state of the elements in the CCTO films. It cannot detect the silver signal with the oxidation states due to small amount of silver doping in the films and the limitation of the XPS instruments that can measure only elemental compositions from top surface to about 10 nm depth from the surface. Fortunately, EDX analysis could be used to confirm the presence of Ag atoms in the Ag-doped CCTO thin film. Even though, the only doped film is presented the spectra of silver (Ag) that is too low because of small doping concentration but the Ag signals increased as the doping concentration increased and the Cu signals decreased. This could indicate that silver substitutes the copper positions of the CCTO lattice. In addition, I also confirmed the existence of silver doping in the films with Raman experiments. The Raman spectra of the CCTO films with different Ag doping concentration are highly defined, showing intensive bands in the range of 100-1200 cm^{-1}. It can be confirmed that the silver signals appeared from the vibration mode of Ag-O

bonds at 258 cm^{-1}. Their integrated peak areas increase linearly with Ag-doping concentration increase from 0.3 to 0.9 wt%.

For gas sensing properties, the sensor response of CCTO sensors was operated as a function of gas concentration and operating temperatures of 150, 200, 250, 300 and 350 °C toward various gases including H_2S, NH_3, H_2, NO_2 and C_2H_5OH. Both undoped CCTO and Ag-doped CCTO thin films is selective to H_2S against NH_3, H_2, NO_2 and ethanol vapor. Silver doped CCTO films can be used as the active medium for constructing H_2S gas sensors in such a low concentration range of 0.2 to 10 ppm at the optimal operating temperature of 250 °C. The doped film sensor showed stability and relatively shorter response and recovery times than the undoped film. The sensor response of the sensor depends on the doping level, achieving a sensor response on the order of 100 at silver concentrations of 0.9 weight %. The silver doped CCTO films are remarkably selective, with typically 100 to 1000 times higher response to H_2S than H_2, NH_3, NO_2 and ethanol vapor. Comparison between H_2S-sensing properties of Ag-doped CCTO and Fe-doped CCTO film, 0.9 wt% (1.7% by mol) Ag-doped film shows better performance than that of 7 wt% (51.2% by mol) Fe-doped CCTO film such as a smaller response time while keeping small doping concentrations. The response time of 0.9 wt% Ag-doped CCTO (2.96 s) is shorter than that for 9 wt% Fe-doped CCTO (~8.5 s). Silver ions appear to play a catalytic role in enhancing the response of the sensors, likely involving sites with a pair of silver ions in close proximity. Therefore, Ag-doped CCTO films with small doping concentration constitutes an excellent candidate for developing H_2S sensors operating at low-temperatures of 250 °C and Ag-doped CCTO films still display a good H_2S selectivity.

Future works:

For more characterization of the sensing material in the future, X-ray Absorption Fine Structure Spectroscopy (XAFS) will be characterized to determine the small silver signal of the Ag-doped CCTO films. XAFS uses the x-ray photoelectric effect and the wave nature of the electron to determine local structures around selected atomic species in materials. And Auger Electron Spectroscopy (AES) should be used in this future work because it is an analytical technique used to determine the elemental composition and the chemical state of the atoms in the surface of a solid material. Relaxation in AES is larger than in XPS. Chemical effects in XPS will not directly correspond with those of Auger. Therefore, these techniques maybe used to confirm to the small silver dopants in the Ag-doped CCTO films.

For gas-sensing properties, the sensor response of Ag-doped CCTO film sensors should be improved with several methods such as the utilization of heterogeneous interface. Ag/SnO_2 nanocomposite with quick response and recovery behavior upon exposure to H_2S as low as 1 ppm at working temperature as low as 70 °C prepared by the sol-gel method, has been reported [96]. Consequently, we should try to prepare the films using other methods to improve gas-sensing properties with high sensor response by increasing the surface area.

REFERENCES

[1] P.-G. Su, Y.-T. Peng, Fabrication of a room-temperature H_2S gas sensor based on PPy/WO_3 nanocomposite films by in-situ photopolymerization, Sensors and Actuators B: Chemical, 193 (2014) 637-643.

[2] J. Lindenmann, V. Matzi, N. Neuboeck, B. Ratzenhofer-Komenda, A. Maier, F.M. Smolle-Juettner, Severe hydrogen sulphide poisoning treated with 4-dimethylaminophenol and hyperbaric oxygen, Diving and hyperbaric medicine, 40 (2010) 213-217.

[3] S.S. Kim, J.Y. Park, S.-W. Choi, H.S. Kim, H.G. Na, J.C. Yang, C. Lee, H.W. Kim, Room temperature sensing properties of networked GaN nanowire sensors to hydrogen enhanced by the Ga_2Pd_5 nanodot functionalization, International Journal of Hydrogen Energy, 36 (2011) 2313-2319.

[4] S. Dhall, K. Sood, R. Nathawat, Room temperature hydrogen gas sensors of functionalized carbon nanotubes based hybrid nanostructure: Role of Pt sputtered nanoparticles, International Journal of Hydrogen Energy, 42 (2017) 8392-8398.

[5] S. Xu, K. Kan, Y. Yang, C. Jiang, J. Gao, L. Jing, P. Shen, L. Li, K. Shi, Enhanced NH_3 gas sensing performance based on electrospun alkaline-earth metals composited SnO_2 nanofibers, Journal of Alloys and Compounds, 618 (2015) 240-247.

[6] A.A. Mane, A.V. Moholkar, Orthorhombic MoO_3 nanobelts based NO_2 gas sensor, Applied Surface Science, 405 (2017) 427-440.

[7] S.P. Patil, V.L. Patil, S.S. Shendage, N.S. Harale, S.A. Vanalakar, J.H. Kim, P.S. Patil, Spray pyrolyzed indium oxide thick films as NO_2 gas sensor, Ceramics International, 42 (2016) 16160-16168.

[8] A.C.o.G.I. Hygienists, Threshold Limit Values for Chemical Substances and Physical Agents and Biological Exposure Indices, American Conference of Governmental Industrial Hygienists, 1995.

[9] D.W.H. Fam, A.I.Y. Tok, A. Palaniappan, P. Nopphawan, A. Lohani, S.G. Mhaisalkar, Selective sensing of hydrogen sulphide using silver nanoparticle decorated carbon nanotubes, Sensors and Actuators B: Chemical, 138 (2009) 189-192.

[10] G. Korotcenkov, Metal oxides for solid-state gas sensors: What determines our choice?, Materials Science and Engineering: B, 139 (2007) 1-23.

[11] Y. Wang, Y. Wang, J. Cao, F. Kong, H. Xia, J. Zhang, B. Zhu, S. Wang, S. Wu, Low-temperature H_2S sensors based on Ag-doped α-Fe_2O_3 nanoparticles, Sensors and Actuators B: Chemical, 131 (2008) 183-189.

[12] Y. Wang, X. Cui, Q. Yang, J. Liu, Y. Gao, P. Sun, G. Lu, Preparation of Ag-loaded mesoporous WO_3 and its enhanced NO_2 sensing performance, Sensors and Actuators B: Chemical, 225 (2016) 544-552.

[13] Y. Tang, Z. Li, X. Zu, J. Ma, L. Wang, J. Yang, B. Du, Q. Yu, Room-temperature NH_3 gas sensors based on Ag-doped γ-Fe_2O_3/SiO_2 composite films with sub-ppm detection ability, Journal of Hazardous Materials, 298 (2015) 154-161.

[14] D.N. Chavan, G.E. Patil, D.D. Kajale, V.B. Gaikwad, P.K. Khanna, G.H. Jain, Nano Ag-Doped Thick Film: A Low-Temperature Gas Sensor, Journal of Sensors, 2011 (2011) 8.

[15] S. Ma, J. Jia, Y. Tian, L. Cao, S. Shi, X. Li, X. Wang, Improved H_2S sensing properties of Ag/TiO_2 nanofibers, Ceramics International, 42 (2016) 2041-2044.

[16] K.S. Yoo, S.D. Han, H.G. Moon, S.-J. Yoon, C.-Y. Kang, Highly Sensitive H_2S Sensor Based on the Metal-Catalyzed SnO_2 Nanocolumns Fabricated by Glancing Angle Deposition, Sensors (Basel, Switzerland), 15 (2015) 15468-15477.

[17] V.B. Gaikwad, M.K. Deore, P.K. Khanna, D.D. Kajale, S.D. Shinde, D.N. Chavan, G.H. Jain, Studies on Gas Sensing Performance of Pure and Nano- Ag Doped ZnO Thick Film Resistors, in: S.C. Mukhopadhyay, G.S. Gupta, R.Y.-M. Huang (Eds.) Recent Advances in Sensing Technology, Springer Berlin Heidelberg, Berlin, Heidelberg, 2009, pp. 293-307.

[18] J. Sukunta, A. Wisitsoraat, A. Tuantranont, S. Phanichphant, C. Liewhiran, Highly-sensitive H_2S sensors based on flame-made V-substituted SnO_2 sensing films, Sensors and Actuators B: Chemical, 242 (2017) 1095-1107.

[19] S. Kabcum, N. Tammanoon, A. Wisitsoraat, A. Tuantranont, S. Phanichphant, C. Liewhiran, Role of molybdenum substitutional dopants on H_2S-sensing enhancement of flame-spray-made SnO_2 nanoparticulate thick films, Sensors and Actuators B: Chemical, 235 (2016) 678-690.

[20] V. Kruefu, A. Wisitsoraat, A. Tuantranont, S. Phanichphant, Ultra-sensitive H_2S sensors based on hydrothermal/impregnation-made Ru-functionalized WO_3 nanorods, Sensors and Actuators B: Chemical, 215 (2015) 630-636.

[21] K. Inyawilert, A. Wisitsoraat, A. Tuantranont, S. Phanichphant, C. Liewhiran, Ultra-sensitive and highly selective H_2 sensors based on FSP-made Rh-substituted SnO_2 sensing films, Sensors and Actuators B: Chemical, 240 (2017) 1141-1152.

[22] S. Kabcum, D. Channei, A. Tuantranont, A. Wisitsoraat, C. Liewhiran, S. Phanichphant, Ultra-responsive hydrogen gas sensors based on PdO nanoparticle-

decorated WO_3 nanorods synthesized by precipitation and impregnation methods, Sensors and Actuators B: Chemical, 226 (2016) 76-89.

[23] M.S. Barbosa, P.H. Suman, J.J. Kim, H.L. Tuller, J.A. Varela, M.O. Orlandi, Gas sensor properties of Ag- and Pd-decorated SnO micro-disks to NO_2, H_2 and CO: Catalyst enhanced sensor response and selectivity, Sensors and Actuators B: Chemical, 239 (2017) 253-261.

[24] S.A. Patil, L.A. Patil, D.R. Patil, G.H. Jain, M.S. Wagh, CuO-modified tin titanate thick film resistors as H_2-gas sensors, Sensors and Actuators B: Chemical, 123 (2007) 233-239.

[25] Y.-S. Shim, L. Zhang, D.H. Kim, Y.H. Kim, Y.R. Choi, S.H. Nahm, C.-Y. Kang, W. Lee, H.W. Jang, Highly sensitive and selective H_2 and NO_2 gas sensors based on surface-decorated WO_3 nanoigloos, Sensors and Actuators B: Chemical, 198 (2014) 294-301.

[26] A. Katoch, S.-W. Choi, H.W. Kim, S.S. Kim, Highly sensitive and selective H_2 sensing by ZnO nanofibers and the underlying sensing mechanism, Journal of Hazardous Materials, 286 (2015) 229-235.

[27] W. Zhang, B. Yang, J. Liu, X. Chen, X. Wang, C. Yang, Highly sensitive and low operating temperature SnO_2 gas sensor doped by Cu and Zn two elements, Sensors and Actuators B: Chemical, 243 (2017) 982-989.

[28] Y. Qin, G. Fan, K. Liu, M. Hu, Vanadium pentoxide hierarchical structure networks for high performance ethanol gas sensor with dual working temperature characteristic, Sensors and Actuators B: Chemical, 190 (2014) 141-148.

[29] L. Wang, Y. Kang, X. Liu, S. Zhang, W. Huang, S. Wang, ZnO nanorod gas sensor for ethanol detection, Sensors and Actuators B: Chemical, 162 (2012) 237-243.

[30] Z. Zhu, C.-T. Kao, R.-J. Wu, A highly sensitive ethanol sensor based on Ag@TiO_2 nanoparticles at room temperature, Applied Surface Science, 320 (2014) 348-355.

[31] R.O. Beauchamp, J.S. Bus, J.A. Popp, C.J. Boreiko, D.A. Andjelkovich, P. Leber, A Critical Review of the Literature on Hydrogen Sulfide Toxicity, CRC Critical Reviews in Toxicology, 13 (1984) 25-97.

[32] C.-C. Lin, B.-K. Wu, D.-K. Lin, Spoilage Bacteria in Canned Foods: I. Flat Sour Spoilage Bacteria in Canned Asparagus and the Thermal Death Time, Applied Microbiology, 16 (1968) 45-47.

[33] N.S. Nasri, J.M. Jones, V.A. Dupont, A. Williams, A comparative study of sulfur poisoning and regeneration of precious-metal catalysts, Energy & fuels, 12 (1998) 1130-1134.

[34] C.D. Parker, Mechanics of Corrosion of Concrete Sewers by Hydrogen Sulfide, Sewage and Industrial Wastes, 23 (1951) 1477-1485.

[35] T. Wells, R.E. Melchers, An observation-based model for corrosion of concrete sewers under aggressive conditions, Cement and Concrete Research, 61–62 (2014) 1-10.

[36] K.F. Chung, Hydrogen sulfide as a potential biomarker of asthma, Expert Review of Respiratory Medicine, 8 (2014) 5-13.

[37] T. Mathew, P. Pownraj, S. Abdulla, B. Pullithadathil, Technologies for Clinical Diagnosis Using Expired Human Breath Analysis, Diagnostics, 5 (2015) 27.

[38] A.A. Felix, E. Longo, J.A. Varela, M.O. Orlandi, Gas sensing and conductivity relationship on nanoporous thin films: A $CaCu_3Ti_4O_{12}$ case study, Thin Solid Films, 604 (2016) 69-73.

[39] A.A. Felix, J.L.M. Rupp, J.A. Varela, M.O. Orlandi, Multi-functional properties of $CaCu_3Ti_4O_{12}$ thin films, Journal of Applied Physics, 112 (2012) 054512.

[40] R. Parra, R. Savu, L.A. Ramajo, M.A. Ponce, J.A. Varela, M.S. Castro, P.R. Bueno, E. Joanni, Sol–gel synthesis of mesoporous $CaCu_3Ti_4O_{12}$ thin films and their gas sensing response, Journal of Solid State Chemistry, 183 (2010) 1209-1214.

[41] S. Pongpaiboonkul, D. Phokharatkul, J.H. Hodak, A. Wisitsoraat, S.K. Hodak, Enhancement of H_2S-sensing performances with Fe-doping in $CaCu_3Ti_4O_{12}$ thin films prepared by a sol–gel method, Sensors and Actuators B: Chemical, 224 (2016) 118-127.

[42] A. Dziaugys, J. Macutkevic, S. Svirskas, R. Juskenas, M. Wencka, J. Banys, S.F. Motria, Y. Vysochanskii, Maxwell–Wagner relaxation and anomalies of physical properties in $Cu_{0.15}Fe_{1.7}PS_3$ mixed material, Journal of Alloys and Compounds, 650 (2015) 386-392.

[43] G. Korotcenkov, B.K. Cho, L.B. Gulina, V.P. Tolstoy, Gas sensor application of Ag nanoclusters synthesized by SILD method, Sensors and Actuators B: Chemical, 166–167 (2012) 402-410.

[44] R. Chen, H.R. Morris, P.M. Whitmore, Fast detection of hydrogen sulfide gas in the ppmv range with silver nanoparticle films at ambient conditions, Sensors and Actuators B: Chemical, 186 (2013) 431-438.

[45] L. Singh, U.S. Rai, K.D. Mandal, N.B. Singh, Progress in the growth of $CaCu_3Ti_4O_{12}$ and related functional dielectric perovskites, Progress in Crystal Growth and Characterization of Materials, 60 (2014) 15-62.

[46] L. Feng, Y. Wang, Y. Yan, G. Cao, Z. Jiao, Growth of highly-oriented $CaCu_3Ti_4O_{12}$ thin films on $SrTiO_3$ (1 0 0) substrates by a chemical solution route, Applied Surface Science, 253 (2006) 2268-2271.

[47] K.D. MANDAL, A.K. RAI, L. SINGH, O. PARKASH, Dielectric properties of $CaCu_{2.9}Co_{0.1}Ti_4O_{12}$ and $CaCu_3Ti_{3.9}Co_{0.1}O_{12}$ ceramics synthesized by semi-wet route, Bulletin of Materials Science, 35 (2012) 433-438.

[48] D. Xu, K. He, R. Yu, L. Jiao, H. Yuan, X. Sun, G. Zhao, H. Xu, X. Cheng, Effect of $AETiO_3$ (AE = Mg, Ca, Sr) doping on dielectric and varistor characteristics of $CaCu_3Ti_4O_{12}$ ceramic prepared by the sol–gel process, Journal of Alloys and Compounds, 592 (2014) 220-225.

[49] W. Yang, S. Yu, R. Sun, R. Du, Nano- and microsize effect of CCTO fillers on the dielectric behavior of CCTO/PVDF composites, Acta Materialia, 59 (2011) 5593-5602.

[50] P. Liu, Y. Lai, Y. Zeng, S. Wu, Z. Huang, J. Han, Influence of sintering conditions on microstructure and electrical properties of $CaCu_3Ti_4O_{12}$ (CCTO) ceramics, Journal of Alloys and Compounds, 650 (2015) 59-64.

[51] D.P. Singh, Y.N. Mohapatra, D.C. Agrawal, Dielectric and leakage current properties of sol–gel derived calcium copper titanate (CCTO) thin films and CCTO/ZrO_2 multilayers, Materials Science and Engineering: B, 157 (2009) 58-65.

[52] F. Amaral, M.A. Valente, L.C. Costa, Dielectric properties of $CaCu_3Ti_4O_{12}$ (CCTO) doped with GeO_2, Journal of Non-Crystalline Solids, 356 (2010) 822-827.

[53] A.A. Felix, M.O. Orlandi, J.A. Varela, Schottky-type grain boundaries in CCTO ceramics, Solid State Communications, 151 (2011) 1377-1381.

[54] J.-W. Lee, J.-H. Koh, Enhanced dielectric properties of Ag-doped CCTO ceramics for energy storage devices, Ceramics International, 43 (2017) 9493-9497.

[55] C.J. Brinker, G.W. Scherer, CHAPTER 3 - Hydrolysis and Condensation II: Silicates, in: Sol-Gel Science, Academic Press, San Diego, 1990, pp. 96-233.

[56] C.J. Brinker, G.W. Scherer, CHAPTER 14 - Applications, in: Sol-Gel Science, Academic Press, San Diego, 1990, pp. 838-880.

[57] K. Norrman, A. Ghanbari-Siahkali, N.B. Larsen, Studies of spin-coated polymer films, Annual Reports Section "C" (Physical Chemistry), 101 (2005) 174-201.

[58] P. Temple-Boyer, L. Mazenq, J.B. Doucet, V. Conédéra, B. Torbiéro, J. Launay, Theoretical studies of the spin coating process for the deposition of polymer-based Maxwellian liquids, Microelectronic Engineering, 87 (2010) 163-166.

[59] N. Sahu, B. Parija, S. Panigrahi, Fundamental understanding and modeling of spin coating process: A review, Indian Journal of Physics, 83 (2009) 493-502.

[60] C.J. Brinker, G.W. Scherer, CHAPTER 8 - Drying, in: Sol-Gel Science, Academic Press, San Diego, 1990, pp. 452-513.

[61] C.J. Brinker, G.W. Scherer, CHAPTER 9 - Structural Evolution during Consolidation, in: Sol-Gel Science, Academic Press, San Diego, 1990, pp. 514-615.

[62] A. Mirzaei, K. Janghorban, B. Hashemi, A. Bonavita, M. Bonyani, S. Leonardi, G. Neri, Synthesis, Characterization and Gas Sensing Properties of Ag@α-Fe_2O_3 Core–Shell Nanocomposites, Nanomaterials, 5 (2015) 737.

[63] L. Filipovic, S. Selberherr, Performance and Stress Analysis of Metal Oxide Films for CMOS-Integrated Gas Sensors, Sensors, 15 (2015) 7206.

[64] S. Choopun, N. Hongsith, E. Wongrat, Metal-Oxide Nanowires for Gas Sensors, in: X. Peng (Ed.) Nanowires - Recent Advances, InTech, Rijeka, 2012, pp. Ch. 01.

[65] N.Z. Misak, Langmuir isotherm and its application in ion-exchange reactions, Reactive Polymers, 21 (1993) 53-64.

[66] J.A. Seibert, X-ray imaging physics for nuclear medicine technologists. Part 1: Basic principles of x-ray production, Journal of nuclear medicine technology, 32 (2004) 139-147.

[67] W.J. Meredith, J.B. Massey, CHAPTER V - THE PRODUCTION OF X-RAYS, in: Fundamental Physics of Radiology, Butterworth-Heinemann, 1968, pp. 44-58.

[68] R. Dalven, Review of Semiconductor Physics, in: R. Dalven (Ed.) Introduction to Applied Solid State Physics: Topics in the Applications of Semiconductors, Superconductors, Ferromagnetism, and the Nonlinear Optical Properties of Solids, Springer US, Boston, MA, 1990, pp. 1-25.

[69] P. Gnanamoorthy, V. Karthikeyan, V.A. Prabu, Field Emission Scanning Electron Microscopy (FESEM) characterisation of the porous silica nanoparticulate structure of marine diatoms, Journal of Porous Materials, 21 (2014) 225-233.

[70] M. Sabbadini, P.E. Frandsen, M. Ghilardi, G.A.E. Vandenbosch, EDX 2014; Companion tools and other 2nd year developments, in: Proceedings of the Fourth European Conference on Antennas and Propagation, 2010, pp. 1-5.

[71] G.S. Bumbrah, R.M. Sharma, Raman spectroscopy – Basic principle, instrumentation and selected applications for the characterization of drugs of abuse, Egyptian Journal of Forensic Sciences, 6 (2016) 209-215.

[72] E. Desimoni, B. Brunetti, X-Ray Photoelectron Spectroscopic Characterization of Chemically Modified Electrodes Used as Chemical Sensors and Biosensors: A Review, Chemosensors, 3 (2015) 70.

[73] S.K. Hodak, T. Supasai, A. Wisitsoraat, J.H. Hodak, Design of low cost gas sensor based on $SrTiO_3$ and $BaTiO_3$ films, Journal of nanoscience and nanotechnology, 10 (2010) 7236-7238.

[74] I.J. Kim, S.D. Han, C.H. Han, J. Gwak, D.U. Hong, D. Jakhar, K.C. Singh, J.S. Wang, Development of micro hydrogen gas sensor with SnO_2-Ag_2O-PtO_x composite using MEMS process, Sensors and Actuators B: Chemical, 127 (2007) 441-446.

[75] S. Pongpaiboonkul, Y. Kasa, D. Phokharatkul, B. Putasaeng, J.H. Hodak, A. Wisitsoraat, S.K. Hodak, Controlling the preferential orientation in sol-gel prepared $CaCu_3Ti_4O_{12}$ thin films by $LaAlO_3$ and $NdGaO_3$ substrates, Applied Surface Science, 385 (2016) 324-332.

[76] L. Daniel, H. Nagai, N. Yoshida, M. Sato, Photocatalytic Activity of Vis-Responsive Ag-Nanoparticles/TiO_2 Composite Thin Films Fabricated by Molecular Precursor Method (MPM), Catalysts, 3 (2013) 625-645.

[77] N.D. Burrows, S. Harvey, F.A. Idesis, C.J. Murphy, Understanding the Seed-Mediated Growth of Gold Nanorods through a Fractional Factorial Design of Experiments, Langmuir, 33 (2017) 1891-1907.

[78] M.C. Biesinger, L.W.M. Lau, A.R. Gerson, R.S.C. Smart, Resolving surface chemical states in XPS analysis of first row transition metals, oxides and hydroxides: Sc, Ti, V, Cu and Zn, Applied Surface Science, 257 (2010) 887-898.

[79] Z. Yao, H. Liu, Y. Liu, Z. Wu, Z. Shen, Y. Liu, M. Cao, Structure and dielectric behavior of Nd-doped $BaTiO_3$ perovskites, Materials Chemistry and Physics, 109 (2008) 475-481.

[80] R. Zimmermann, P. Steiner, R. Claessen, F. Reinert, S. Hüfner, Electronic structure systematics of 3d transition metal oxides, Journal of Electron Spectroscopy and Related Phenomena, 96 (1998) 179-186.

[81] M. Punginsang, A. Wisitsora-at, A. Tuantranont, S. Phanichphant, C. Liewhiran, Effects of cobalt doping on nitric oxide, acetone and ethanol sensing performances of

FSP-made SnO_2 nanoparticles, Sensors and Actuators B: Chemical, 210 (2015) 589-601.

[82] N. Pauly, F. Yubero, S. Tougaard, Quantitative analysis of satellite structures in XPS spectra of gold and silver, Applied Surface Science, 383 (2016) 317-323.

[83] M.A. Ponce, M.A. Ramirez, F. Schipani, E. Joanni, J.P. Tomba, M.S. Castro, Electrical behavior analysis of n-type $CaCu_3Ti_4O_{12}$ thick films exposed to different atmospheres, Journal of the European Ceramic Society, 35 (2015) 153-161.

[84] M.L. Moreira, E.C. Paris, G.S. do Nascimento, V.M. Longo, J.R. Sambrano, V.R. Mastelaro, M.I.B. Bernardi, J. Andrés, J.A. Varela, E. Longo, Structural and optical properties of $CaTiO_3$ perovskite-based materials obtained by microwave-assisted hydrothermal synthesis: An experimental and theoretical insight, Acta Materialia, 57 (2009) 5174-5185.

[85] I. Ganesh, A.K. Gupta, P.P. Kumar, P.S. Sekhar, K. Radha, G. Padmanabham, G. Sundararajan, Preparation and characterization of Ni-doped TiO_2 materials for photocurrent and photocatalytic applications, TheScientificWorldJournal, 2012 (2012) 127326.

[86] I. Martina, R. Wiesinger, D. Jembrih-Simb¨¹rger, M. Schreiner, Micro-Raman Characterisation of Silver Corrosion Products: Instrumental Set Up and Reference Database, E-Preservation Science, (2012).

[87] V. Strelchuk, O. Kolomys, B.O. Golichenko, M.I. Boyko, E.B. Kaganovich, I.M. Krishchenko, S. Kravchenko, O. Lytvyn, E.G. Manoilov, I. Nasieka, Micro-Raman study of nanocomposite porous films with silver nanoparticles prepared using pulsed laser deposition, 2015.

[88] S. Phanichphant, Semiconductor Metal Oxides as Hydrogen Gas Sensors, Procedia Engineering, 87 (2014) 795-802.

[89] J. Blanc, N. Derouiche, A. El Hadri, J. Germain, C. Maleysson, H. Robert, Study of the action of gases on a polypyrrole film, Sensors and Actuators B: Chemical, 1 (1990) 130-133.

[90] J. Gong, Q. Chen, M.-R. Lian, N.-C. Liu, R.G. Stevenson, F. Adami, Micromachined nanocrystalline silver doped SnO_2 H_2S sensor, Sensors and Actuators B: Chemical, 114 (2006) 32-39.

[91] P. Shankar, J.B.B. Rayappan, Gas sensing mechanism of metal oxides: The role of ambient atmosphere, type of semiconductor and gases - A review, Science Letters, 4 (2015) 126.

[92] M.E. Franke, T.J. Koplin, U. Simon, Metal and metal oxide nanoparticles in chemiresistors: does the nanoscale matter?, Small (Weinheim an der Bergstrasse, Germany), 2 (2006) 36-50.

[93] J. Xu, X. Wang, J. Shen, Hydrothermal synthesis of In_2O_3 for detecting H_2S in air, Sensors and Actuators B: Chemical, 115 (2006) 642-646.

[94] R. Kumar, A. Khanna, V.S. Sastry, Interaction of reducing gases with tin oxide films prepared by reactive evaporation techniques, Vacuum, 86 (2012) 1380-1386.

[95] W. Wei, S. Guo, C. Chen, L. Sun, Y. Chen, W. Guo, S. Ruan, High sensitive and fast formaldehyde gas sensor based on Ag-doped $LaFeO_3$ nanofibers, Journal of Alloys and Compounds, 695 (2017) 1122-1127.

[96] S.G.S.a.A.B. Gambhireb, Gas sensing properties of nanocrystalline silver/tin dioxide sensor prepared by coprecipitation method, Applied Science Research, 5(5) (2014) 12-18

[97] R.K. Birdwhistell, E. Griswold, The Effect of Some Salts on the Solubility of Silver Acetate and of Silver Nitrate in Acetic Acid at 30 °C, Journal of the American Chemical Society, 77 (1955) 873-875.

[98] A A2 - Urben, PG, in: Bretherick's Handbook of Reactive Chemical Hazards (Seventh Edition), Academic Press, Oxford, 2007, pp. 1-65.

APPENDICES

Appendix A

Ag-doping concentrations

In order to doped Ag in CCTO films, we can be calculated the percentage of Ag concentration for silver acetate by following expression

$$\left(\frac{\frac{g_{AgCH_3CO_2}}{MW_{AgCH_3CO_2}}}{\frac{g_{Ca(C_2H_3O_2)_2\cdot xH_2O}}{MW_{Ca(C_2H_3O_2)_2\cdot xH_2O}}}\right)\left(\frac{MW_{Ag}}{MW_{CCTO}}\right)\times 100 = \ldots\ldots\% \, Ag \; by \; weight$$

$$\left(\frac{\frac{g_{AgCH_3CO_2}}{166.92}}{\frac{0.855}{158.17}}\right)\left(\frac{107.86}{613.37}\right)\times 100 = \ldots\ldots\% \, Ag \; by \; weight$$

$$g_{AgCH_3CO_2}\times 19.49 = \ldots\ldots\% \, Ag \; by \; weight$$

In this thesis, I tried to dope Ag 0.3%, 0.6% and 0.9% by weight. By following the Equation above, we weighed Ag 0.01496 g, 0.02992 g and 0.04488 g for Ag doped 0.3%, 0.6% and 0.9% by weight, respectively. However, the quantity of Ag in our films were later measured from EDX experiments which are 0.21%, 0.39% and 0.70% by weight instead of 0.3%, 0.6% and 0.9% by weight.

In order to doped Ag in CCTO films, we can be calculated the percentage of Ag concentration for silver perchlorate by following expression

$$\left(\frac{\frac{g_{AgClO_4}}{MW_{AgClO_4}}}{\frac{g_{Ca(C_2H_3O_2)_2\cdot xH_2O}}{MW_{Ca(C_2H_3O_2)_2\cdot xH_2O}}}\right)\left(\frac{MW_{Ag}}{MW_{CCTO}}\right)\times 100 = \ldots\ldots\% \; Ag \; by \; weight$$

$$\left(\frac{\frac{g_{AgClO_4}}{207.32}}{\frac{0.855}{158.17}}\right)\left(\frac{107.86}{613.37}\right)\times 100 = \ldots\ldots\% \; Ag \; by \; weight$$

$$g_{AgClO_4}\times 15.69 = \ldots\ldots\% \; Ag \; by \; weight$$

In this thesis, I tried to dope Ag 1%, 3%, 5%, 7% and 9% by weight. By following the Equation above, we weighed Ag 0.0637 g, 0.1912 g, 0.3181 g, 0.4461 g and 0.5736 g for Ag doped 1%, 3%, 5%, 7% and 9% by weight, respectively. However, the quantity of Ag in our films were later measured from EDX experiments which are not presented the Ag signal in the EDX spectra of the Ag-doped CCTO films.

Appendix B

XRD database

The crystal structure of the CCTO films on substrates were synthesized by the sol-gel technique. They were compared with the XRD database from The International Centre for Diffraction Data (ICDD) which illustrated as follow

Pattern : 01-075-2188 ***Radiation =*** 1.540598 ***Quality :*** Calculated

$(CaCu_3)Ti_4O_{12}$

Calcium Copper Titanium Oxide
Also called: Calcium tricopper tetratitanium oxide

Lattice : Body-centered cubic
S.G. : Im-3 (204)

a = 7.39100

Z = 2

Mol. weight = 614.31
Volume [CD] = 403.75
Dx = 5.053
I/Icor = 5.76

ICSD collection code: 032002
Temperature factor: ITF
Cancel:
Data collection flag: Ambient.

Bochu, B., Deschizeaux, M.N., Joubert, J.C., Collomb, A., Chenavas, J., Marezio, M., J. Solid State Chem., volume 29, page 291 (1979)
Calculated from ICSD using POWD-12++

Radiation : CuKa1
Lambda : 1.54060
SS/FOM : F22=1000(0.0000,22)

Filter : Not specified
d-sp : Calculated spacings

2th	i	h	k	l
16.952	27	1	1	0
24.062	3	2	0	0
29.581	38	2	1	1
34.289	999	2	2	0
38.486	73	0	1	3
42.327	49	2	2	2
45.904	40	3	2	1
49.276	263	4	0	0
52.485	13	4	1	1
55.562	3	0	2	4
58.529	8	3	3	2
61.405	401	4	2	2
64.204	5	0	1	5
69.618	6	1	2	5
72.252	92	4	4	0
74.848	17	4	3	3
77.413	7	6	0	0
79.951	7	6	1	1
82.471	101	6	2	0
84.975	1	1	4	5
87.470	1	6	2	2
89.961	2	1	3	6

Pattern : 00-021-1276 **Radiation =** 1.540598 **Quality :** High

TiO_2

Titanium Oxide
Rutile, syn
Also called: titania

Lattice : Tetragonal
S.G. : P42/mnm (136)

a = 4.59330
c = 2.95920

Z = 2

Mol. weight = 79.90
Volume [CD] = 62.43
Dx = 4.250
Dm = 4.230
I/Icor = 3.40

General comments: No impurity over 0.001%.
Vickers hardness number: VHN_{100}=1132-1187.
Sample source or locality: Sample obtained from National Lead Co., South Amboy, New Jersey, USA.
General comments: Pattern reviewed by Syvinski, W., McCarthy, G., North Dakota State Univ, Fargo, North Dakota, USA, *ICDD Grant-in-Aid* (1990). Agrees well with experimental and calculated patterns.
General comments: Two other polymorphs, anatase (tetragonal) and brookite (orthorhombic), converted to rutile on heating above 700 C.
General comments: Additional weak reflections [indicated by brackets] were observed.
Optical data: A=2.9467, B=2.6505, Sign=+
Additional pattern: Validated by calculated pattern.
General comments: Optical data on specimen from *Dana's System of Mineralogy, 7th Ed.*, I 555.
General comments: Naturally occurring material may be reddish brown.
Color: White
Reflectance: Opaque mineral optical data on specimen from Sweden: R_3R%= 20.3, Disp.=Std.
Temperature of data collection: Pattern taken at 25 C.
Data collection flag: Ambient.

Natl. Bur. Stand. (U.S.) Monogr. 25, volume 7, page 83 (1969)

Radiation : CuKa1
Lambda : 1.54056
SS/FOM : F30=108(0.0087,32)

Filter : Monochromator crystal
d-sp : Not given
Internal standard : W

2th	i	h	k	l
27.447	100	1	1	0
36.086	50	1	0	1
39.188	8	2	0	0
41.226	25	1	1	1
44.052	10	2	1	0
54.323	60	2	1	1
56.642	20	2	2	0
62.742	10	0	0	2
64.040	10	3	1	0
65.480	2	2	2	1
69.010	20	3	0	1
69.790	12	1	1	2
72.410	2	3	1	1
74.411	1	3	2	0
76.510	4	2	0	2
79.822	2	2	1	2
82.335	6	3	2	1
84.260	4	4	0	0
87.464	2	4	1	0
89.557	8	2	2	2
90.708	4	3	3	0
95.275	6	4	1	1
96.017	6	3	1	2
97.176	4	4	2	0
98.514	1	3	3	1
105.099	2	4	2	1
106.019	2	1	0	3
109.406	2	1	1	3
116.227	4	4	0	2
117.527	4	5	1	0
120.059	8	2	1	3
122.788	8	4	3	1
123.660	8	3	3	2
131.847	6	4	2	2
136.549	8	3	0	3
140.052	12	5	2	1
143.116	2	4	4	0
155.869	2	5	3	0

Pattern : 00-029-1360 **Radiation =** 1.540598 **Quality :** High

TiO_2

Titanium Oxide
Brookite

Lattice : Orthorhombic
S.G. : Pcab (61)

a = 5.45580
b = 9.18190
c = 5.14290
a/b = 0.59419
c/b = 0.56011

Z = 8

Mol. weight = 79.90
Volume [CD] = 257.63
Dx = 4.120
Dm = 4.140

Optical data: A=2.5831, B=2.5843, Q=2.7004, Sign=+, 2V=~28°
Additional pattern: To replace 00-016-0617 and validated by calculated pattern.
Color: Black
Additional pattern: See ICSD 36408 (PDF 01-076-1934).
Sample source or locality: Specimen from Magnet Cove, Arkansas, USA (USNM 97661).
Analysis: Spectrographic analysis: 0.1-1.0% Si; 0.01-0.1% each of Al, Fe, and V; 0.001-0.01% Mg.
General comments: Niobian brookite from Mozambique [Chemical analysis (wt.%): Ti O2 80.7, Nb2 O5 14.1, FeO 5.53]; Carvalho et al., *Rev. Cien. Geol. Ser. A*, **7** 61 (1974) reports an identical pattern.
Temperature of data collection: Pattern taken at 25 C.
General comments: Intensities verified by calculated pattern.
Data collection flag: Ambient.

Natl. Bur. Stand. (U.S.) Monogr. 25, volume 3, page 57 (1964)

Radiation : CuKa1
Lambda : 1.54056
SS/FOM : F30= 58(0.0115,45)

Filter : Beta
d-sp : Not given

2th	i	h	k	l
25.340	100	1	2	0
25.689	80	1	1	1
30.808	90	1	2	1
32.791	4	2	0	0
36.252	25	0	1	2
37.297	18	2	0	1
37.934	6	1	3	1
38.371	4	2	2	0
38.576	4	2	1	1
39.205	5	0	4	0
39.967	8	1	1	2
40.153	18	0	2	2
42.340	16	2	2	1
46.072	16	0	3	2
48.012	30	2	3	1
49.173	18	1	3	2
49.694	3	2	1	2
52.012	3	2	4	0
54.205	20	3	2	0
55.234	30	2	4	1
55.711	5	1	5	1
57.176	13	1	1	3
57.685	2	2	3	2
59.991	7	1	2	3
62.065	10	0	5	2
63.065	4	1	6	0
63.415	9	3	1	2
63.643	12	2	5	1
64.104	12	2	0	3
64.603	6	1	3	3
65.002	10	2	1	3
65.876	9	1	6	1
68.768	5	4	0	0
70.432	8	3	3	2
71.490	3	4	0	1
71.931	2	2	3	3
73.648	2	0	0	4
76.948	10	0	2	4
79.024	2	4	3	1
79.283	1	1	2	4
83.643	4	3	3	3
84.287	2	0	8	0
84.724	2	4	4	1
86.743	4	0	4	4
95.590	3	5	2	1
*95.590	3	4	2	3
95.993	2	2	8	1
97.609	4	3	2	4
102.559	2	1	2	5
103.201	4	3	7	2
*103.201	4	2	5	4

Pattern : 03-065-5714 **Radiation =** 1.540598 **Quality :** Calculated

TiO_2

Titanium Oxide

Lattice : Body-centered tetragonal
S.G. : I41/amd (141)

Mol. weight = 79.90
Volume [CD] = 136.30

a = 3.78500
c = 9.51400

Dx = 3.894

Z = 4
I/Icor = 5.04

NIST M&A collection code: A 50867 ST1243 1
Temperature factor: TF Isotropic TF given by author
Sample preparation: Commercial pigmentary material was used
Remarks from ICSD/CSD: Anatase-synthetic
Data collection flag: Ambient.

Cromer, D.T., Herrington, K., J. Am. Chem. Soc., volume 77, page 4708 (1955)
Calculated from NIST using POWD-12++

Radiation : CuKa1
Lambda : 1.54060
SS/FOM : F30=597(0.0014,35)

Filter : Not specified
d-sp : Calculated spacings

2th	i	h	k	l
25.304	999	1	0	1
36.949	56	1	0	3
37.793	175	0	0	4
38.566	71	1	1	2
48.036	238	2	0	0
53.886	148	1	0	5
55.061	146	2	1	1
62.107	23	2	1	3
62.684	103	2	0	4
68.756	49	1	1	6
70.287	49	2	2	0
74.053	4	1	0	7
75.046	74	2	1	5
76.032	20	3	0	1
80.740	3	0	0	8
82.156	5	3	0	3
82.672	35	2	2	4
83.154	15	3	1	2
93.244	5	2	1	7
94.202	17	3	0	5
95.162	19	3	2	1
98.325	11	1	0	9
99.812	7	2	0	8
101.236	5	3	2	3
107.478	24	3	1	6
108.988	12	4	0	0
112.826	2	3	0	7
113.868	22	3	2	5
114.918	13	4	1	1
118.472	35	2	1	9
*118.472	35	1	1	10
120.117	6	2	2	8
121.749	5	4	1	3
122.353	15	4	0	4
122.921	10	3	3	2
131.049	20	4	2	0
132.007	5	1	0	11
135.995	3	3	2	7
137.389	19	4	1	5
142.878	1	4	0	6
143.850	7	3	0	9

Pattern : 00-046-1212 **Radiation =** 1.540598 **Quality :** High

Al_2O_3

Aluminum Oxide
Corundum, syn
Also called: α- Al2 O3

Lattice : Rhombohedral
S.G. : R-3c (167)

a = 4.75870
c = 12.99290
Z = 6

Mol. weight = 101.96
Volume [CD] = 254.81
Dx = 3.987

Sample source or locality: The sample is an alumina plate as received from *ICDD.*
General comments: Unit cell computed from d_{obs}.
Optical data: A=1.7604, B=1.7686, Sign=-
Data collection flag: Ambient.

Huang, T., Parrish, W., Masciocchi, N., Wang, P., Adv. X-Ray Anal., volume 33, page 295 (1990)

Radiation : CuKa1
Lambda : 1.54056
SS/FOM : F25=379(0.0026,25)

Filter : Not specified
d-sp : Diffractometer

2th	*i*	*h*	*k*	*l*
25.579	45	0	1	2
35.153	100	1	0	4
37.777	21	1	1	0
41.676	2	0	0	6
43.356	66	1	1	3
46.176	1	2	0	2
52.550	34	0	2	4
57.497	89	1	1	6
59.740	1	2	1	1
61.118	2	1	2	2
61.300	14	0	1	8
66.521	23	2	1	4
68.214	27	3	0	0
70.420	1	1	2	5
74.299	2	2	0	8
76.871	29	1	0	10
77.226	12	1	1	9
80.422	1	2	1	7
80.700	2	2	2	0
83.217	1	3	0	6
84.359	3	2	2	3
85.143	1	1	3	1
86.363	2	3	1	2
86.503	3	1	2	8
88.997	9	0	2	10

Appendix C

Solubility of silver compounds

The solubility of silver acetate in acetic acid at 30 °C is found to be 0.00470 molal [97]. It can be calculated that the maximum amount of silver acetate is 0.019613 g in acetic acid 25 g at 30 °C. In addition, the solubility of silver acetate in acetic acid will be increased at high temperature. Silver acetate 0.0655 g can be dissolved in acetic acid 25 g at 76 °C.

The solubility of silver perchlorate in acetic acid at 19.8 °C is found to be 79.86 g in acetic acid 100 g [98]. It means that silver perchlorate 19 g can be dissolved in acetic acid 25 g at 76 °C.

Appendix D

Conference Presentations

International Presentation:

2016, Aukrit Natkaeo, Satreerat K. Hodak, Jose H. Hodak, Anurat Wisitsoraat and Disayut Phokharakul. Modifiacation of Calcium Copper Titanate Thin Films by Adding Ag Substances and their H_2S Gas Sensing Response. Poster presentation at the 3rd International congress on Advanced Materials (AM 2016) at Centara Grand, Central Plaza Ladprao, Bangkok, Thailand (November 27-30 2016) Code: ENM-P-34

I am glad to receive award for the excellent poster presentation in this conference.

Modification of Calcium Copper Titanate Thin Films by Adding Ag Compounds and their H_2S Gas Sensing Response

Aukrit Natkaeo[1], Ditsayut Phokharatkul[2], Jose H. Hodak[3], Anurat Wisitsoraat[2], Satreerat K. Hodak[1,*]
[1]Department of Physics, Faculty of Science, Chulalongkorn University, Bangkok 10330, Thailand
[2]Nanoelectronics and MEMS Laboratory, Pathumthani 12120, Thailand
[3]DQIAyQF FCEN University of Buenos Aires/INQUIMAE-CONICET, Argentina
*corresponding author: satreerat.h@chula.ac.th

Abstract

Ag-doped $CaCu_3Ti_4O_{12}$ (CCTO) thin films with different doping concentrations were prepared by a sol-gel technique. Films were grown by depositing four layers of CCTO on alumina substrates followed by sputtering Au/Cr interdigitated electrodes to fabricate gas sensors. The films were characterized by X-ray diffraction (XRD), field emission scanning electron microscopy (FESEM) and energy dispersive X-ray spectroscopy (EDX). The films have predominantly the perovskite CCTO crystal phase with very small amount of TiO_2 secondary phases. In this work, both undoped CCTO and Ag-doped CCTO thin films were tested for selective sensing to H_2S gas relative to NH_3, H_2, NO_2 and ethanol vapor. For characterizing gas sensing properties of the films, gas concentrations in the range of 0.2-10 ppm were used with operating temperatures ranging from 150 to 350 °C. When compared to undoped CCTO sensor, the Ag-doped CCTO sensors presented much higher response. The best sensitivity towards H_2S was found in 0.75 wt% Ag-doped CCTO film and at the optimum operating temperature of 250 °C. The highest response of the sensor based on the 0.75 wt% Ag-doped CCTO film to 10 ppm of H_2S is approximately ten times than that of a sensor based on undoped CCTO film. The doped film sensor also showed stability and relatively short response and recovery times. Therefore, Ag-doped CCTO films with small doping concentration constitute an excellent candidate for developing H_2S sensors operating at low-temperatures.

Introduction

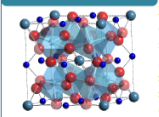

Fig. 1 CCTO structure.

The pseudo perovskite structure of $CaCu_3Ti_4O_{12}$ material has cubic structure having an octahedral tilting distortion. The dielectric properties of CCTO have attracted considerable interest for inventing microelectronic devices because of its giant dielectric constant of about 10^4-10^5 in the temperature range of 100-600 K. Nowadays, there is continuous demand for miniaturization of electronic devices, and interest to develop capacitor materials with high dielectric constant and low loss for applications in microelectronic devices [1].

In recent years, gas sensors for the detection of gaseous molecules have attracted much attention. The goal of gas sensor research is to create the detection with a group range of gases or specific type of gases. Detection the quantity of gases is important for security and gas control. It would be expected to be useful for many applications such as food processing, environmental remediation, agriculture, medical diagnostics and defense. In recent research work in our laboratory, both undoped CCTO and Fe-doped CCTO thin films is selective to H_2S against NH_3, CO, C_2H_2, CH_4, ethanol and NO_2 [2]. Even for pure CCTO thin film could be selective and sensitive to H_2S with the sensitivity of about 10. Furthermore, the sensitivity of 9 wt% Fe-doped CCTO film towards H_2S increased to more than 100 which is about 10 times of that of pure CCTO thin film. Thus, it is interesting further to a novel dopant in the CCTO films. In this work, the effect of Ag-modifying CCTO thin films towards H_2S and the comparison in response times and recovery times with that of Fe-doped CCTO films is focused.

Methodology

- The solution sol-gel method (SSG) is described in the following diagram:

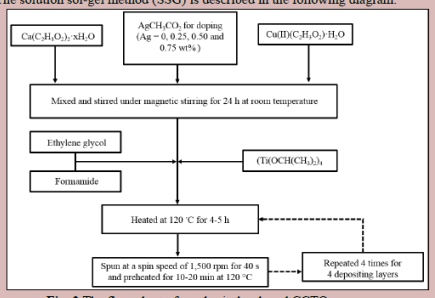

Fig. 2 The flow chart of synthesis Ag-doped CCTO precursor and the fabrication of Ag-doped CCTO films.

CCTO thin films grown with different conditions on alumina substrates were sputtered with Au/Cr electrode as coplanar patterns for quantitative detection of gases. The electrode was deposited on the film surface through a photolithographic mask created using a positive photoresist followed by photoresist lift-off in acetone within an ultrasonic bath.

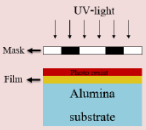

Fig. 3 Photolithography process.

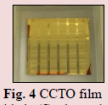

Fig. 4 CCTO film with Au/Cr electrode.

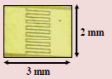

Fig. 5 CCTO sensors.

The gas sensor sensitivity S is defined as :

$$S = R_a/R_g$$

where R_a and R_g stand for the resistances of the samples in air and H_2S respectively.

Results and Discussion

XRD results

The XRD patterns of Ag-doped CCTO thin films deposited on silicon substrates calcined at 800 °C with different Ag concentrations are shown in Fig. 6. The dominant diffraction peaks of silicon substrates were detected in XRD analysis on (220), (400) and (422) planes which can be seen in the film grown on alumina substrate as well.

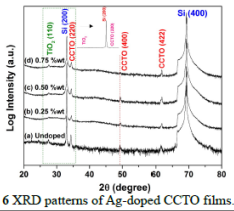

Fig. 6 XRD patterns of Ag-doped CCTO films.

Surface morphology & cross section

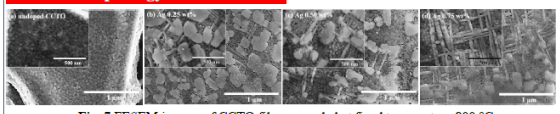

Fig. 7 FESEM images of CCTO films annealed at fixed temperature 800 °C.

Surface morphologies of CCTO films with different Ag doping concentrations are shown in Fig. 7 (a)-(d). It is seen that the undoped CCTO film has granular morphology.

Fig. 8 shows a cross section image of Ag-doped CCTO film on alumina substrate. It can be seen that the film thickness is approximately 360 to 500 nm for four layers of deposition.

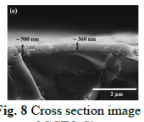

Fig. 8 Cross section image of CCTO film.

EDX spectra

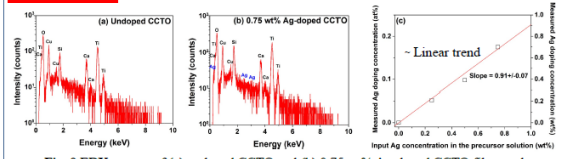

Fig. 9 EDX spectra of (a) undoped CCTO and (b) 0.75 wt% Ag-doped CCTO films and (c) the plot of measured Ag doping concentrations and the concentration of Ag in precursor solutions.

Gas sensing properties

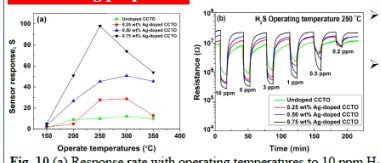

Fig. 10 (a) Response rate with operating temperatures to 10 ppm H_2S (b) Resistance changes for films exposed to H_2S gas at 250 °C.

- The maximum response is observed for 0.75 wt% Ag-doped CCTO at 250 °C.
- The highest concentration for Ag dopant has the maximum response (~98.7) at low operating temperature (250 °C).

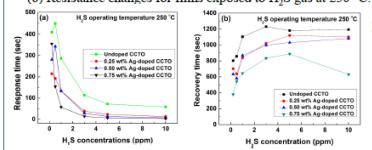

Fig. 11 (a) and (b) show the typical response and recovery time of Ag doped CCTO sensor to different H_2S concentrations

- The smallest number of response and recover times belong to 0.75 wt% Ag-doped CCTO sensor to 10 ppm H_2S.
- The sensors exhibit the highest response to 10 ppm H_2S, moderate response to NO_2 at low concentration (5 ppm) and negligible response to NH_3, H_2 and C_2H_5OH even at such a high concentration.

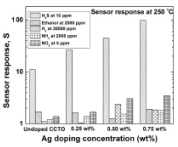

Fig. 12 Selectivity histograms exhibited by the undoped CCTO and Ag-doped CCTO sensors towards various gases at 250 °C.

Conclusions

In this study, Ag-doped CCTO thin films were successfully synthesized by a sol-gel technique. According to XRD patterns, FESEM images and EDX spectra, they confirmed the crystal structure of CCTO. For gas sensing properties, both undoped CCTO and Ag-doped CCTO thin films is selective to H_2S against NH_3, H_2, NO_2 and ethanol vapor. Ag-doped CCTO films with small doping concentration constitute an excellent candidate for developing H_2S sensors operating at low-temperatures of 250 °C. The highest response of the sensor based on the 0.75 wt% Ag-doped CCTO to 10 ppm of H_2S is approximately 99.

References

[1] Gong, J., Chen, Q., Lian, M.R., Liu, N.C. Micromachined nanocrystalline silver doped tin oxide hydrogen sulfide sensors, Proceeding of MSTI-Nanotech 2 (2005) 301-305.

[2] Pongpaiboonkul, S., Phokharatkul, D., Hodak, J.H., Wisitsoraat, A., Hodak, S.K. Enhancement of H_2S-sensing performances with Fe-doping in $CaCu_3Ti_4O_{12}$ thin films prepared by a sol-gel method, Sensors and Actuators B: Chemical 224 (2015) 118-127.

Local Presentation:

2017, Aukrit Natkaeo, Satreerat K. Hodak, Jose H. Hodak, Anurat Wisitsoraat and Disayut Phokharakul. Modifiacation of Calcium Copper Titanate Thin Films by Adding Ag Compounds and their H_2S Gas Sensing Response. Poster presentation at Siam Physics Congress 2017 at Rayong Marriott & Spa, Rayong, Thailand (May 24-26 2017) Code: P-SI10-249

Modification of Calcium Copper Titanate Thin Films by Adding Ag Compounds and their H_2S Gas Sensing Response

Aukrit Natkaeo[1], Ditsayut Phokharatkul[2], Jose H. Hodak[3], Anurat Wisitsoraat[2], Satreerat K. Hodak[1,*]
[1]Department of Physics, Faculty of Science, Chulalongkorn University, Bangkok 10330, Thailand
[2]Nanoelectronics and MEMS Laboratory, Pathumthani 12120, Thailand
[3]DQIAyQF FCEN University of Buenos Aires/INQUIMAE-CONICET, Argentina
*corresponding author: satreerat.h@chula.ac.th

NECTEC a member of NSTDA
SPC2017 Siam Physics Congress 2017

Abstract

Ag-doped $CaCu_3Ti_4O_{12}$ (CCTO) thin films with different doping concentrations were prepared by a sol-gel technique. Films were grown by depositing four layers of CCTO on alumina substrates followed by sputtering Au/Cr interdigitated electrodes to fabricate gas sensors. The films were characterized by X-ray diffraction (XRD), field emission scanning electron microscopy (FESEM) and energy dispersive X-ray spectroscopy (EDX). The films have predominantly the perovskite CCTO crystal phase with very small amount of TiO_2 secondary phases. In this work, both undoped CCTO and Ag-doped CCTO thin films were tested for selective sensing to H_2S gas relative to NH_3, H_2, NO_2 and ethanol vapor. For characterizing gas sensing properties of the films, gas concentrations in the range of 0.2-10 ppm were used with operating temperatures ranging from 150 to 350 °C. When compared to undoped CCTO sensor, the Ag-doped CCTO sensors presented much higher response. The best sensitivity towards H_2S was found in 0.9 wt% Ag-doped CCTO film and at the optimum operating temperature of 250 °C. The highest response of the sensor based on the 0.9 wt% Ag-doped CCTO film to 10 ppm of H_2S is approximately ten times than that of a sensor based on undoped CCTO film. The doped film sensor also showed stability and relatively short response and recovery times. Therefore, Ag-doped CCTO films with small doping concentration constitute an excellent candidate for developing H_2S sensors operating at low-temperatures.

Introduction

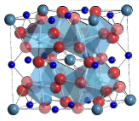

Fig. 1 CCTO structure.

The pseudo perovskite structure of $CaCu_3Ti_4O_{12}$ material has cubic structure having an octahedral tilting distortion. The dielectric properties of CCTO have attracted considerable interest for inventing microelectronic devices because of its giant dielectric constant of about 10^4-10^5 in the temperature range of 100-600 K. Nowadays, there is continuous demand for miniaturization of electronic devices, and interest to develop capacitor materials with high dielectric constant and low loss for applications in microelectronic devices [1].

In recent years, gas sensors for the detection of gaseous molecules have attracted much attention. The goal of gas sensor research is to create the detection with a group range of gases or specific type of gases. Detection the quantity of gases is important for security and gas control. It would be expected to be useful for many applications such as food processing, environmental remediation, agriculture, medical diagnostics and defense.

In recent research work in our laboratory, both undoped CCTO and Fe-doped CCTO thin films is selective to H_2S against NH_3, CO, C_2H_2, CH_4, ethanol and NO_2 [2]. Even for pure CCTO thin film could be selective and sensitive to H_2S with the sensitivity of about 10. Furthermore, the sensitivity of 9 wt% Fe-doped CCTO film towards H_2S increased to more than 100 which is about 10 times of that of pure CCTO thin film. Thus, it is interesting further to a novel dopant in the CCTO films. In this work, the effect of Ag-modifying CCTO thin films towards H_2S and the comparison in response times and recovery times with that of Fe-doped CCTO films is focused

Methodology

- The solution sol-gel method (SSG) is described in the following diagram:

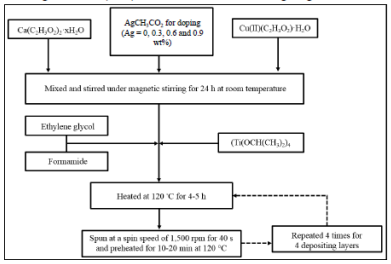

Fig. 2 The flow chart of synthesis Ag-doped CCTO precursor and the fabrication of Ag-doped CCTO films.

CCTO thin films grown with different conditions on alumina substrates were sputtered with Au/Cr electrode as coplanar patterns for quantitative detection of gases. The electrode was deposited on the film surface through a photolithographic mask created using a positive photoresist followed by photoresist lift-off in acetone within an ultrasonic bath.

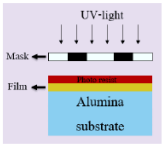

Fig. 3 Photolithography process.

Fig. 4 CCTO film with Au/Cr electrode.

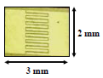

Fig. 5 CCTO sensors.

The gas sensor sensitivity S is defined as :

$$S = R_a/R_g$$

where R_a and R_g stand for the resistances of the samples in air and H_2S respectively.

Results and Discussion

XRD results

The XRD patterns of Ag-doped CCTO thin films deposited on silicon substrates calcined at 800 °C with different Ag concentrations are shown in Fig. 6. The dominant diffraction peaks of silicon substrates were detected in XRD analysis on (220), (400) and (422) planes which can be seen in the film grown on alumina substrate as well.

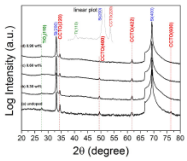

Fig. 6 XRD patterns of Ag-doped CCTO films.

Surface morphology & cross section

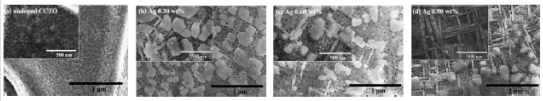

Fig. 7 FESEM images of CCTO films annealed at fixed temperature 800 °C.

Surface morphologies of CCTO films with different Ag doping concentrations are shown in Fig. 7 (a)-(d). It is seen that the undoped CCTO film has granular morphology.

Fig. 8 shows a cross section image of Ag-doped CCTO film on alumina substrate. It can be seen that the film thickness is approximately 360 to 500 nm for four layers of deposition.

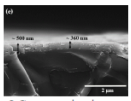

Fig. 8 Cross section image of CCTO film.

EDX spectra

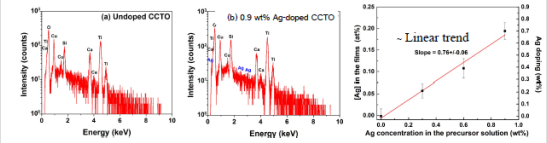

Fig. 9 EDX spectra of (a) undoped CCTO and (b) 0.9 wt% Ag-doped CCTO films and (c) the plot of measured Ag doping concentrations and the concentration of Ag in precursor solutions.

Gas sensing properties

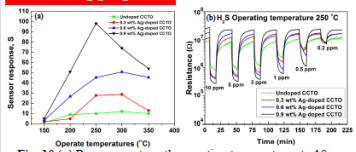

- The maximum response is observed for 0.9 wt% Ag-doped CCTO at 250 °C.
- The highest concentration for Ag dopant has the maximum response (~98.7) at low operating temperature (250 °C).

Fig. 10 (a) Response rate with operating temperatures to 10 ppm H_2S (b) Resistance changes for films exposed to H_2S gas at 250 °C.

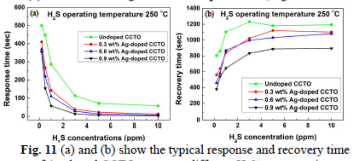

- The smallest number of response and recover times belong to 0.9 wt% Ag-doped CCTO sensor to 10 ppm H_2S.

Fig. 11 (a) and (b) show the typical response and recovery time of Ag doped CCTO sensor to different H_2S concentrations

- The sensors exhibit the highest response to 10 ppm H_2S, moderate response to NO_2 at low concentration (5 ppm) and negligible response to NH_3, H_2 and C_2H_5OH even at such a high concentration.

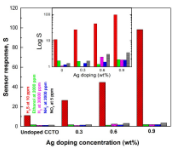

Fig. 12 Selectivity histograms exhibited by the undoped CCTO and Ag-doped CCTO sensors towards various gases at 250 °C.

Conclusions

In this study, Ag-doped CCTO thin films were successfully synthesized by a sol-gel technique. According to XRD patterns, FESEM images and EDX spectra, they confirmed the crystal structure of CCTO. For gas sensing properties, both undoped CCTO and Ag-doped CCTO thin films is selective to H_2S against NH_3, H_2, NO_2 and ethanol vapor. Ag-doped CCTO films with small doping concentration constitute an excellent candidate for developing H_2S sensors operating at low-temperatures of 250 °C. The highest response of the sensor based on the 0.9 wt% Ag-doped CCTO to 10 ppm of H_2S is approximately 99.

References :
[1] Gong, J., Chen, Q., Lian, M.R., Liu, N.C. Micromachined nanocrystalline silver doped tin oxide hydrogen sulfide sensors, Proceeding of MSTI-Nanotech 2 (2005) 301-305.
[2] Poungsiboonkul, S., Phokharatkul, D., Hodak, J.H., Wisitsoraat, A., Hodak, S.K. Enhancement of H_2S-sensing performances with Fe-doping in $CaCu_3Ti_4O_{12}$ thin films prepared by a sol-gel method, Sensors and Actuators B: Chemical 224 (2015) 118-127.

VITA

Mr. Aukrit Natkaeo was born on 12th July, 1991, in Surat Thani province, Thailand. He got high school level from PSU.Wittayanusorn School, Songkhla in 2009. He has received Development and Promotion of Science and Technology Talents Project (DPST) in 2010. He finished the bachelor degree in Physics, Department of Physics, Faculty of Science, Prince of Songkla University, Hat Yai campus in 2013. His bachelor degree had been supervised by Assistant Professor Dr. Helmut Josef Durrast. Since 2014, he has been studying the master degree in Physics, Department of Physics, Faculty of Science, Chulalongkorn University. His master degree have been under the supervision of Associate Professor Dr. Satreerat K. Hodak.